

SOLUTION-PHASE SYNTHESIS AND CHARACTERIZATION OF  $\text{Fe}_2\text{GeS}_4$  MATERIAL  
AND PHOTOVOLTAIC DEVICES

By

Mimi Liu

A DISSERTATION

Submitted to the faculty of Delaware State University in partial fulfillment  
of the requirements for the degree of Doctor of Philosophy  
of Applied Chemistry in the Department of Chemistry

DOVER, DELAWARE

December 2018

This dissertation is approved by the following members of the Final Oral Review Committee:

Dr. Cherese Winstead Casson, Committee Chairperson, Department of Chemistry, Delaware State University

Dr. Daniela R. Radu, Committee Co-Chairperson, Department of Mechanical and Materials Engineering, Florida International University

Dr. Aristides Marcano, Committee Member, Division of Physical and Computational Sciences, Delaware State University

Dr. Gabriel Gwanmesia, Committee Member, Division of Physical and Computational Sciences, Delaware State University

Dr. Gulnihal Ozbay, Committee Member, Department of Agriculture and Natural Resources, Delaware State University

Dr. Kevin Dobson, External Committee Member, Institute of Energy Conversion, University of Delaware

## **DEDICATION**

This dissertation is dedicated to my parents Zihuai Liu and Sheqing Gao, who supported me at all stages of my life. They also taught me to work hard to achieve the goals I am pursuing. I also want to express my gratitude to my brothers and sister for their understanding and believing. Whenever I encounter difficulties in life, they always support and encourage me. I am truly grateful for having them in my life.

## ACKNOWLEDGMENTS

This work was completed under the guidance of my research advisor Dr. Daniela R. Radu and academic advisor Dr. Cherese Winstead-Casson. Specifically, I would like to thank Dr. Daniela R. Radu for her academic guidance, support, and encouragement over the past three years. I would also like to express my gratitude to Dr. Cherese Winstead-Casson for her guidance and kind assistance in my doctoral program. They both have provided a lot of help not only for my research but also for my professional life in Delaware State University. I would like to express my sincere appreciation to Dr. Cheng-Yu Lai, for his expert guidance and help. In addition, I wish to thank Dr. Dominik Berg for helping me with all the instruments and solar cell measurements.

I also would like to acknowledge my committee members, Dr. Aristides Marcano, Dr. Gabriel Gwanmesia, Dr. Gulnihal Ozbay, and Dr. Kevin Dobson for their guidance, input on my dissertation, and providing professional suggestions. Additionally, I wish to acknowledge Dr. Dyremple B. Marsh and Dr. Charlie Wilson for their kind support through my graduate program.

I would like to thank all the professors in the Department of Chemistry. Their teaching has provided foundation for my dissertation research and my future studies. At the same time, I would like to thank my laboratory group members: Anjuli Bhandari, Po-yu Hwang, Hao-Hsin Chi, Nicholas Pizzi, and undergraduate interns Aaron R Legar, Dylan R McConnell, for their kind helps and support.

This project is based upon work supported in part by the US Department of Energy SunShot Initiative (Award DE-EE0006322) and the National Science Foundation (Grants

1458980 and 1435716). I would also like to acknowledge the INBRE program for the financial support for my graduate assistantship.

# **SOLUTION-PHASE SYNTHESIS AND CHARACTERIZATION OF $\text{Fe}_2\text{GeS}_4$ MATERIAL AND PHOTOVOLTAIC DEVICES**

**Mimi Liu**

**Research Advisor: Dr. Daniela R. Radu**

**Faculty Advisor Cherese Winstead Casson**

## **ABSTRACT**

Recently, climate change and the energy crisis are warning human race that it is necessary to develop new renewable energy. Solar energy is considered to be one of the cleanest and most abundant energy sources to replace fossil fuels. Solar cells are extensively studied devices that convert sunlight into electricity. However, recent solar cells have been hampered by high cost, use of toxic materials and low conversion efficiency. To further improve the solar cells, a cheap, earth-abundant, and non-toxic material is required.

The ternary compound  $\text{Fe}_2\text{GeS}_4$  (FGS) has attracted considerable attention because it not only has high absorption coefficient and band gap suitable for photovoltaic applications but also has better sustainability. In addition, the elements contained in FGS are relatively abundant in earth's crust and are less toxic. In my dissertation work, FGS crystals were prepared using two methods, solution-phase synthesis of FGS precursor, followed by a thermal treatment and one-pot synthesis.

In the solution-phase synthesis of FGS precursor, the effects of reaction parameters such as precursors, solvents, reaction times on the chemical and physical properties of the resulting products have been comprehensively investigated. The results show that a stable FGS precursor

can be prepared in the mixture of oleylamine (OLA) and 1-Octadecene (ODE), using Fe (III) 2,4-pentanedionate, Ge (Gly)<sub>2</sub>(H<sub>2</sub>O)<sub>2</sub>, elemental sulfur as Fe, Ge and S source, while the reaction time is 15 minutes. Then, the optimization of the annealing conditions for FGS powders has also been studied. Finally, the highly crystalline FGS powders were obtained by a two-step process, solution-phase synthesis of FGS precursors and thermal treatment at 550°C for 2 hours under sulfur/argon atmosphere. FGS thin films were fabricated by dip-coating the prepared FGS inks on the substrate and performing the same thermal treatment at 550°C for 2 hours under sulfur/argon atmosphere. The FGS solution-based solar cell using FGS thin film as the light absorbing layer showed a significant open-circuit voltage ( $V_{OC}$ ) of 361 mV. When the optimized FGS thin film was incorporated into a well-established dye-sensitized solar cell, the fabricated FGS-catalyzed dye-sensitized solar cell achieved a higher open-circuit voltage ( $V_{OC}$ ), short-circuit current density ( $J_{SC}$ ) and conversion efficiency ( $\eta$ ).

In the one-pot synthesis of FGS NCs, the effects of trioctylphosphine oxide (TOPO) and reaction time on the product have been determined. The results show that the plate-like FGS crystals can be prepared within 5 hours, using FeCl<sub>2</sub>, Ge(Gly)<sub>2</sub>(H<sub>2</sub>O)<sub>2</sub>, TOPO, and 1-dodecanethiol (1-DDT) as reactants, while OLA acts as the solvent. A high-quality FGS thin film was prepared by dip-coating and thermal treatment at 400 °C for 2 hours under sulfur/argon atmosphere. Similar to the solar cells fabricated based on FGS precursor, the photovoltaic devices based on the FGS NCs also exhibited a significant open-circuit voltage.

# TABLE OF CONTENTS

LIST OF TABLES .....	ix
LIST OF FIGURES .....	x
LIST OF ABBREVIATIONS.....	xv
<b>CHAPTER 1. INTRODUCTION .....</b>	<b>1</b>
1.1. Solar Cells .....	1
1.1.1. First-Generation Solar Cells (Crystalline Silicon).....	3
1.1.2. Second-Generation Solar Cells (Thin Film) .....	4
1.1.3. Third-Generation Solar Cells.....	6
1.2. Characteristic of Solar Cells.....	6
1.2.1. Open-Circuit Voltage ( $V_{OC}$ ).....	7
1.2.2. Short-Circuit Current ( $I_{SC}$ ).....	8
1.2.3. Peak Power ( $P_m$ ).....	8
1.2.4. Fill Factor (FF).....	9
1.2.5. Conversion Efficiency ( $\eta$ ).....	9
1.3. Material Options for Thin Film Solar Cells .....	10
1.3.1. Absorption Coefficient.....	10
1.3.2. Optical Band Gap ( $E_g$ ) .....	12
1.4. $Fe_2GeS_4$ Absorber Layer and $Fe_2GeS_4$ Based Solar Cells .....	15
1.4.1. $Fe_2GeS_4$ (FGS) .....	15
1.4.2. Dye-Sensitized Solar Cell (DSSC) .....	16
<b>CHAPTER 2. LITERATURE REVIEW .....</b>	<b>19</b>
2.1. Iron Dichalcogenides $FeX_2$ ( $X=S, Se, Te$ ) .....	19
2.1.1. Properties of Iron Disulfide ( $FeS_2$ ) .....	20
2.1.2. Problems of p- $FeS_2$ Based Solar Cells.....	25
2.2. Ternary Fe Based Chalcogenides $Fe_2GeS_4$ .....	30
2.2.1. Properties and Applications of $Fe_2GeS_4$ Materials .....	30
2.2.2. Synthesis of $Fe_2GeS_4$ Materials via Solid-State Method .....	36
2.2.3. Synthesis of $Fe_2GeS_4$ Materials via Wet Chemical Method .....	41
2.2.4. Fabrication of $Fe_2GeS_4$ Thin Films by RF Magnetron Sputtering.....	45
<b>CHAPTER 3. MATERIALS AND METHOD .....</b>	<b>47</b>
3.1. Materials.....	47
3.2. Experimental Outline .....	48
3.2.1. Synthesis of $Fe_2GeS_4$ Precursors.....	49
3.2.2. Fabrication of $Fe_2GeS_4$ Thin Films .....	52

3.2.3. Fabrication of Fe <sub>2</sub> GeS <sub>4</sub> Based Photovoltaic Devices .....	52
3.2.4. Characterization Technique .....	53
3.2.5. Photocurrent-Voltage Measurements.....	56
<b>CHAPTER 4. SOLUTION-PROCESSED FE<sub>2</sub>GES<sub>4</sub> THIN FILMS AND SOLAR CELLS</b>	<b>58</b>
4.1. Introduction .....	58
4.2. Experimental Section .....	58
4.2.1. Synthesis of FGS Precursors.....	58
4.2.2. Preparation of FGS Powders.....	62
4.2.3. Fabrication of FGS Thin Films .....	63
4.2.4. Solar Cells Fabrication.....	65
4.3. Result and Discussion .....	69
4.3.1. Results of Synthesized FGS Precursors.....	69
4.3.2. Results of Prepared Fe <sub>2</sub> GeS <sub>4</sub> Powders.....	76
4.3.3. Results of FGS Thin Films .....	79
4.3.4. Performance of FGS Thin Films in Photovoltaic Devices.....	84
4.4. Conclusion.....	90
<b>CHAPTER 5. ONE-POT SYNTHESIS OF FE<sub>2</sub>GES<sub>4</sub> NANOCRYSTALS AND SOLAR CELLS</b>	<b>92</b>
5.1. Introduction .....	92
5.2. Experimental Section .....	93
5.2.1. Synthesis of FGS Nanocrystals.....	94
5.2.2. Fabrication of FGS Thin Films .....	95
5.2.3. Solar Cells Fabrication.....	95
5.3. Results and Discussion.....	98
5.3.1. Results of Synthesis of FGS Nanocrystals.....	98
5.3.2. Effects of Trioctylphosphine Oxide (TOPO).....	101
5.3.3. Results of FGS Thin Films .....	103
5.3.4. Results of FGS NP-Based Solar Cells .....	103
5.4. Conclusion.....	107
<b>CHAPTER 6. CONCLUSION AND PATH FORWARD</b> .....	<b>108</b>
<b>REFERENCES</b> .....	<b>112</b>

## LIST OF TABLES

<b>Table 2.1.</b> Some physical-chemical properties of S, Se and Te .....	20
<b>Table 2.2.</b> Band gap and k-points at VB and CB edges. HSE06 and $\Delta$ -sol gaps are obtained at the experimental lattice constants .....	24
<b>Table 2.3.</b> Experimental conditions used in preparation of Fe <sub>2</sub> GeS <sub>4</sub> materials using different method.....	45
<b>Table 3.1.</b> Materials used in this research .....	47
<b>Table 4.1.</b> Selection of reaction parameters .....	61
<b>Table 4.2.</b> Photovoltaic performance of DSSCs with different counter electrode.....	88
<b>Table 5.1.</b> XRF results of as-synthesized FGS NPs using different time. ....	102

## LIST OF FIGURES

<b>Figure 1.1.</b> Working mechanism of a solar cell .....	2
<b>Figure 1.2.</b> A typical IV curve of a solar cell.....	7
<b>Figure 1.3.</b> A band gap diagram showing the varied sizes of band gaps for conductors, semiconductors, and insulators .....	12
<b>Figure 1.4. (a)</b> Direct band gap diagram; <b>(b)</b> Indirect band gap .....	13
<b>Figure 1.5.</b> Ideal solar cell efficiency as a function of the band gap energy for the spectral distribution AM0 and AM1.5 .....	14
<b>Figure 1.6.</b> Fe <sub>2</sub> GeS <sub>4</sub> crystal structure .....	16
<b>Figure 1.7.</b> Dye-sensitized solar cell (DSSC).....	17
<b>Figure 1.8.</b> Operating principle of dye-sensitized solar cells .....	18
<b>Figure 2.1.</b> Pyrite (FeS <sub>2</sub> ) crystal structure.....	21
<b>Figure 2.2.</b> Marcasite (FeS <sub>2</sub> ) crystal structure.....	22
<b>Figure 2.3.</b> 3d orbital splitting schemes in pyrite and marcasite.....	23
<b>Figure 2.4.</b> Energy level scheme of FeS <sub>2</sub> .....	24
<b>Figure 2.5.</b> Comparison of the absorption lengths $L = 1/\alpha$ for different semiconductors materials .....	25
<b>Figure 2.6.</b> Calculated formation energy of intermediate S-deficient phases .....	27
<b>Figure 2.7.</b> Crystal structure.....	27
<b>Figure 2.8.</b> Temperature variation of the receptivity of pyrrhotite with different compositions ..	29
<b>Figure 2.9.(a)</b> Fe <sub>2</sub> GeS <sub>4</sub> crystal structure ; <b>(b)</b> Diffuse reflectance data from powders; <b>(c)</b> Calculated optical absorption coefficients for FeS <sub>2</sub> , Fe <sub>2</sub> GeS <sub>4</sub> and Fe <sub>2</sub> SiS <sub>4</sub> .....	31

<b>Figure 2.10.</b> Photocurrent response in a linear sweep from 0 V to -0.5 V .....	32
<b>Figure 2.11. (a)</b> Inverse susceptibility versus temperature in a 21400 Oe field; <b>(b)</b> Spontaneous magnetization as a function of temperature, in a residual field of 110 Oe .....	33
<b>Figure 2.12.</b> Calculated <b>(a)</b> thermopower, <b>(b)</b> electrical conductivity scaled by relaxation time and <b>(c)</b> power factor for Fe <sub>2</sub> GeS <sub>4</sub> .....	35
<b>Figure 2.13.</b> Schematic illustration of Solid-state synthesis. ....	36
<b>Figure 2.14. (A)</b> Schematic illustration of the synthesis of Fe <sub>2</sub> GeS <sub>4</sub> by mechanochemical process; <b>(B)</b> TEM investigations of as-synthesized (a,b) and heat-treated (e, f) Fe <sub>2</sub> GeS <sub>4</sub> NCs. ..	38
<b>Figure 2.15. (A)</b> Comparison of the XRD patterns of the as-synthesized Fe <sub>2</sub> GeS <sub>4</sub> NCs and those post-annealed at 450°C for 2 hours; <b>(B)</b> Comparison of Raman spectra of the as-synthesized Fe <sub>2</sub> GeS <sub>4</sub> NCs and those post-annealed at 450°C for 2 hours; <b>(C)</b> High-resolution XPS spectra of (a) Fe 2p and (b) Ge 3d from as-synthesized (bottom) and post-heat-treated (top) Fe <sub>2</sub> GeS <sub>4</sub> NCs. ....	39
<b>Figure 2.16.</b> Illustration of the synthesis of Fe <sub>2</sub> GeS <sub>4</sub> NPs by a rapid molecular precursor solid-state route .....	40
<b>Figure 2.17.</b> Proposed mechanism of Fe <sub>2</sub> GeS <sub>4</sub> NPs formation .....	40
<b>Figure 2.18.</b> Low resolution TEM image of Fe <sub>2</sub> GeS <sub>4</sub> nanocrystals after a 24 h growth time. ...	43
<b>Figure 2.19. (a, b)</b> TEM images <b>(c)</b> HRTEM image <b>(d)</b> SAED pattern of as-synthesized Fe <sub>2</sub> GeS <sub>4</sub> nanosheets .....	44
<b>Figure 2.20.</b> Process flow diagram of PVD .....	46
<b>Figure 3.1.</b> Outline of research procedures .....	49
<b>Figure 3.2.</b> Schlenk line set-up.....	50

<b>Figure 3.3.</b> Illustration of sample set-up. ....	54
<b>Figure 3.4.</b> Schematic diagram of J-V measurement setup.....	56
<b>Figure 4.1.</b> Illustration of synthesis procedure.....	60
<b>Figure 4.2.</b> Illustration of thermal treatment .....	63
<b>Figure 4.3.</b> Fabrication of FGS thin films .....	63
<b>Figure 4.4.</b> Dye-sensitized solar cell without FGS (ITO/TiO <sub>2</sub> &Dye/Iodine solution/Mo) . ....	67
<b>Figure 4.5.</b> Structure of FGS-catalyzed DSSC. ....	68
<b>Figure 4.6.</b> FGS solution-based solar cell (ITO/TiO <sub>2</sub> /Iodine solution/FGS/Mo) . ....	69
<b>Figure 4.7.</b> XRD patterns of FGS powders prepared from different Fe precursors.....	70
<b>Figure 4.8.</b> XRD patterns of FGS powders prepared from GeI <sub>4</sub> .....	71
<b>Figure 4.9.</b> XRD patterns of FGS precursor powders using different reaction time. ....	72
<b>Figure 4.10.</b> Color change of FGS precursor made from different solvents.....	74
<b>Figure 4.11.</b> XRD pattern of the FGS powder that was annealed after two days of exposure. ...	74
<b>Figure 4.12. (a)</b> Photograph of FGS precursors; <b>(b)</b> XRD pattern of As-synthesized FGS precursors and annealed FGS powders .....	75
<b>Figure 4.13.</b> XRD patterns of FGS powder annealed at different temperature. ....	77
<b>Figure 4.14.</b> Intensity comparison of the most intense XRD peaks from the FGS powders annealed at different temperature.....	78
<b>Figure 4.15.</b> Synchrotron X-Ray analysis of annealed FGS powder .....	78
<b>Figure 4.16.</b> Raman spectrum of annealed FGS powders.....	79
<b>Figure 4.17.</b> XRD patterns of FGS thin films annealed at different temperature. ....	80

<b>Figure 4.18.</b> Comparison of XRD patterns of FGS thin film annealed at 550 °C for different times.....	81
<b>Figure 4.19.</b> Raman spectrum of FGS thin film annealed at 550°C for 2 hours .....	82
<b>Figure 4.20.</b> FGS thin-film band gap evaluation. ....	82
<b>Figure 4.21.</b> SEM Cross section of annealed FGS thin film.....	83
<b>Figure 4.22.</b> Device characteristics for DSSC (ITO/TiO <sub>2</sub> &Dye/Iodine solution/Mo) .....	85
<b>Figure 4.23.</b> Device characteristics for FGS-catalyzed DSSC (ITO/TiO <sub>2</sub> &Dye/Iodine solution /FGS/Mo) .....	86
<b>Figure 4.24.</b> Device characteristics for FGS-catalyzed DSSC (ITO/TiO <sub>2</sub> &Dye/Iodine solution/FGS/FTO). ....	87
<b>Figure 4.25.</b> Device characteristics for FGS solution-based solar cell (ITO/TiO <sub>2</sub> /Iodine solution/FGS/Mo) .....	89
<b>Figure 5.1.</b> Fabrication of FGS NPs-catalyzed dye-sensitized solar cells. ....	93
<b>Figure 5.2.</b> Structure of FGS NPs-catalyzed dye-sensitized solar cells. (ITO/TiO <sub>2</sub> &Dye/ Electrolyte/FGS/FTO).....	97
<b>Figure 5.3. (a)</b> Structure of DSSC without FGS (ITO/TiO <sub>2</sub> &Dye/ Electrolyte/FTO); <b>(b)</b> Structure of FGS solution-based solar cell (ITO/TiO <sub>2</sub> /Electrolyte/ FGS/FTO). ....	97
<b>Figure 5.4.</b> XRD Patterns of FGS NPs prepared with TOPO. ....	98
<b>Figure 5.5.</b> Raman spectrum of as-synthesized FGS NPs.....	99
<b>Figure 5.6.</b> TEM images of as-synthesized FGS NPs.....	99
<b>Figure 5.7.</b> Thermogravimetric analysis (TGA) of as-synthesized FGS NPs.....	100
<b>Figure 5.8.</b> XRD Patterns of FGS NPs prepared without TOPO.....	102

<b>Figure 5.9.</b> (a) XRD pattern of FGS thin film; (b) Raman spectrum of FGS thin film.....	103
<b>Figure 5.10.</b> Device characteristics of DSSC without FGS. (ITO/TiO <sub>2</sub> &Dye/Electrolyte/FTO). .....	104
<b>Figure 5.11.</b> Device characteristics of FGS-catalyzed DSSC. (ITO/TiO <sub>2</sub> &Dye/Electrolyte /FGS/FTO). .....	105
<b>Figure 5.12.</b> Device characteristics of FGS-Solution-based solar cell. (ITO/TiO <sub>2</sub> /Electrolyte /FGS/FTO). .....	106

## LIST OF ABBREVIATIONS

AM	Air mass
a.u	Arbitrary unit
cm	Centimeter
CB	Conduction band
CE	Counter electrode
CIGS	Copper gallium indium selenide
CZTS	Copper zinc tin sulfide
CZTSe	Copper zinc tin selenide
CZTSSe	Copper zinc tin sulfur-selenium
DSSCs	Dye-sensitized solar cells
1-DDT	1-Dodecanethiol
FGS	Fe <sub>2</sub> GeS <sub>4</sub>
FTO	Fluorine-doped tin oxide glass
HRTEM	High-resolution transmission electron microscopy
ITO	Indium doped tin oxide glass
J-V	Photocurrent-voltage
LD50	Median lethal dose
MCs	Metal chalcogenides
m-FeS <sub>2</sub>	Marcasite FeS <sub>2</sub>
Mo	Molybdenum-coated soda lime glass
NCs	Nanocrystals

nm	Nanometer
NPs	Nanoparticles
NSs	Nanosheets
ODE	Octadecene
OLA	Oleylamine
p-FeS <sub>2</sub>	Pyrite FeS <sub>2</sub>
PL	Photoluminescence Spectroscopy
PV	Photovoltaic
PVD	Physical vapor deposition
SEM	Scanning electron microscopy
TE	Thermoelectric
TEM	Transmission electron microscopy
TGA	Thermogravimetric analysis
TOPO	Trioctylphosphine oxide
VB	Valence band
WE	Working electrode
XRD	X-ray diffraction
XRF	X-ray Fluorescence
ZT	Figure of merits

## CHAPTER 1. INTRODUCTION

With fast-growing population and the improvement of human life, the global energy consumption has gradually increased over the coming decades. According to the energy data of 2017, these consumed energies mainly come from fossil fuel which is predicted to run out within the next 100-150 years<sup>[1]</sup>. Moreover, burning fossil fuel-based energy causes an increase in atmospheric CO<sub>2</sub>, which can have some negative influences on our living planet, such as raising its average temperature, expanding ocean water and then increasing sea-level<sup>[2]</sup>. Therefore, both the rising energy demand and CO<sub>2</sub> emissions are warning us that it is necessary to put more emphasis on the renewable energy resources.

Solar energy, which harnessed from the sun, is one of the most popular renewable energy sources not only because it has the minimal impact on the environment but also since it uses unlimited sunlight. Solar energy is mainly used in two forms: (1) photothermal conversion, in which light is transformed to heat; (2) photoelectric conversion, in which light is converted into electricity. The device that is used in photoelectric conversion is called solar cell.

### 1.1. Solar Cells

Solar cells, also known as “Photovoltaic cells” are devices that absorb photons from the sun and then convert them into electricity through photovoltaic effect. The photovoltaic effect is the process of converting sunlight into electrical voltage and current, which was firstly discovered by Edmund Becquerel<sup>[3,4]</sup>. Typically, either Schottky junction or p-n junction can be used to develop the photovoltaic effect of a solar cell. In a photovoltaic device with p-n

junctions, the p-type and n-type semiconductors are joined together to form a p-n junction which is used to separate two types of charges and drive them in contrary directions <sup>[5]</sup>. The p-type semiconductor has a high concentration of holes, whereas the n-type semiconductor has a high concentration of electrons. In the p-n junction, the p-type and n-type semiconductors can be the same material having different dopants or two different materials of p-type and n-type respectively.

As shown in Figure 1.1, the working mechanism of a solar cell includes three processes: 1) when sunlight irradiated on the PV devices, some photons of the light are absorbed by the semiconductors; then, the energy of the absorbed photons is transmitted to the valence electrons which eventually excited and jump out from the bond to produce electron-hole pairs; 2) In the built-in electric field of the p-n junction, photogenerated holes flow into the p region, whereas photogenerated electrons flow into the n region; 3) when an external circuit is connected to these two sides (p-region and n-region), the two types of separated charges are recombined by the external circuit to generate photocurrent <sup>[6]</sup>.

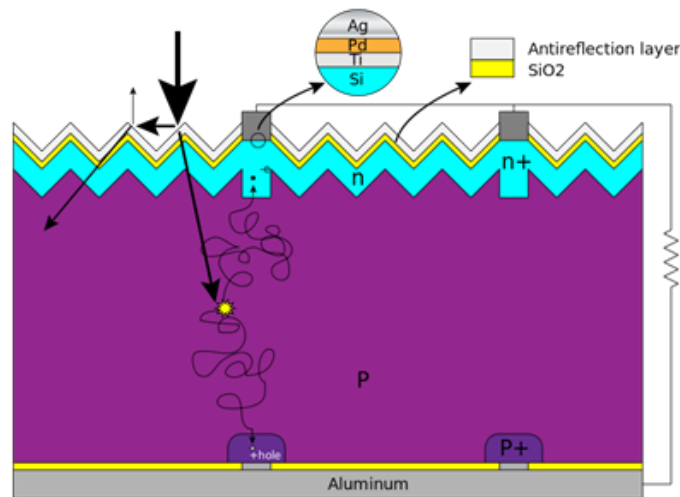


**Figure 1.1.** Working mechanism of a solar cell <sup>[6]</sup>.

Currently, there have been many types of solar cells, such as single crystal silicon solar cells, thin film solar cells, dye-sensitized solar cells, organic solar cells, perovskite solar cells, quantum dot solar cells, and other kinds of solar cells. These solar cells can be roughly divided into three stages depending on its development.

### **1.1.1. First-Generation Solar Cells (Crystalline Silicon)**

Crystalline silicon solar cells are the first generation of solar cells. It is one type of solar cells made of high-purity single crystal silicon wafers, firstly reported by Russell in 1941<sup>[7]</sup>. Up to today, crystalline silicon solar cells have evolved into solar cells with the highest conversion efficiency of 26.3% and the most mature manufacturing technologies<sup>[8]</sup>. However, many studies have shown that semiconductors with direct band gap can convert photons into electron-hole pairs more easily than that with an indirect band gap because that photogenerated electrons in the semiconductors with indirect band gap require additional energy for changing the momentum. Thus, the indirect band gap property of the material impairs its ability to absorb light in semiconductor. This suggests that the indirect gap property of crystalline silicon weaken its capability to absorb light, resulting in the need for a large amount of Si material to absorb all available sunlight<sup>[9]</sup>. As a result, despite the single crystal silicon solar cells currently dominates the large-scale applications and industrial production of solar cells, however, its large quantity of Si material cost and cumbersome battery process impedes the progress of Si NCs for PVs and other optoelectronic applications.

### 1.1.2. Second-Generation Solar Cells (Thin Film)

Compared to first-generation solar cells, second-generation solar cells use a thin film with a typical thickness of micron instead of bulk silicon material as the light absorber, significantly reducing the raw material consumption. For this reason, second-generation solar cells are also called thin film solar cells. In addition, thin film solar cells can be manufactured using inexpensive substrates such as glass, plastics, ceramics, graphite, and metal sheets, which reduces the manufacturing device costs. Furthermore, the fabrication of thin film solar cells can use a variety of deposition techniques and substrates, which undoubtedly provides more opportunities to improve the photovoltaic performance of fabricated solar cells. Therefore, thin film solar cells have extensively studied as promising candidate solar cells in recent years. So far, various materials have been theoretically proposed as the good light absorbing materials for thin film solar cells, such as amorphous silicon, cadmium telluride (CdTe), copper gallium indium diselenide (CIGS), copper zinc tin sulfur (CZTS), and other metal chalcogenides (MC) semiconductor materials.

It is well known that crystals are a material in which atoms, molecules, or ions are arranged in a highly ordered manner. In contrast, the constituents of amorphous material are randomly arranged. Thereby, Si atoms in the amorphous silicon material are arranged in a disordered structure, resulting in the presence of some dangling bonds in this material. These dangling bonds influence the electronic behavior of the material and even affect its photovoltaic applications<sup>[10,11]</sup>. In order to improve the optoelectrical behavior of the amorphous silicon, hydrogen is introduced to passivate the material, resulting in a semiconductor ( $\alpha$ -Si: H) with a direct band gap of 1.7 eV. In addition, the amorphous Si ( $\alpha$ -Si: H) absorbs light more strongly

than crystalline Si at a given thickness. Scientific research shows that the p-n junction, a critical design of the first-generation solar cells, does not work in such amorphous silicon solar cells due to the short motion of light-generated charge carriers from the point of the generation which caused by the localized states in amorphous Si. A few years later, it was found that an amorphous silicon solar cell with p-i-n (or n-i-p) design can work since the p-i-n (or n-i-p) design enables the light-generated charge carriers to be separated in the intrinsic layer <sup>[12]</sup>. In 2015, a triple-junction thin film amorphous silicon solar cell with a record efficiency of 13.6% was obtained by Hitoshi Sai et al. <sup>[13]</sup>. However, amorphous Si solar cells having p-i-n multilayers make the fabrication more complicated, resulting in a rise in cost. Furthermore, the efficiency of amorphous silicon cell will be reduced after prolonged exposure to sunlight, which also hinders the progress of amorphous silicon for PVs and other optoelectronic applications.

In addition to amorphous silicon, metal chalcogenide (MC) nanomaterials have also been proposed as promising candidates for thin film solar cells because of their excellent photovoltaic performance. Currently, cadmium telluride (CdTe), copper indium gallium selenide (CIGS), and copper zinc tin sulfide (CZTS) are the most popular materials. Moreover, quaternary semiconductor copper indium gallium selenide (CIGS) and binary semiconductor cadmium telluride (CdTe) based thin film solar cells have reached significant record efficiencies of 22.6% and 22.1% respectively <sup>[8]</sup>. However, CIGS contain earth-rare elements of indium and gallium. Furthermore, CIGS and CdTe thin film solar cells require the use of toxic elements such as selenium and cadmium, which are considered to have health risks for researcher and manufacturers <sup>[14,15]</sup>.

Base on the exceptional properties of thin film solar cells, more and more research has recently focused on the manufacturing a type of thin film solar cells containing non-toxic and earth-abundant elements.

### **1.1.3. Third-Generation Solar Cells**

The third-generation solar cells are photovoltaic cells which may be able to surmount the Shockley-Queisser limit of 31-41% power efficiency for single gap solar cells <sup>[16,17]</sup>. Third-generation solar cells are considered including nanocrystal based solar cells, polymer based solar cells, dye sensitized solar cells, and concentrated solar cells <sup>[18]</sup>. This generation of solar cells are being fabricated using various technologies, including printing press technologies, organic dyes, and conductive plastics, and so on. It is a type of near-ideal photovoltaic solar cells that have high efficiency, low cost, long life, non-toxicity and high stability. So far, third-generation solar cells that have been manufactured or being manufactured include dye-sensitized solar cells (DSSC), organic solar cells, perovskite solar cells, quantum dot solar cells, as well as CZTS and derivates CZTSe and CZTSSe solar cells.

## **1.2. Characteristic of Solar Cells**

Usually, we use current-voltage curve to determine the photovoltaic performance of a solar cell, as shown in Figure 1.2. Several parameters derived from the measured current-voltage curve are often used to describe the photovoltaic performance of solar cells, including open-

circuit voltage ( $V_{OC}$ ), short-circuit current ( $I_{SC}$ ), peak power ( $P_m$ ), fill factor (FF), power conversion efficiency ( $\eta$ ), and so on.

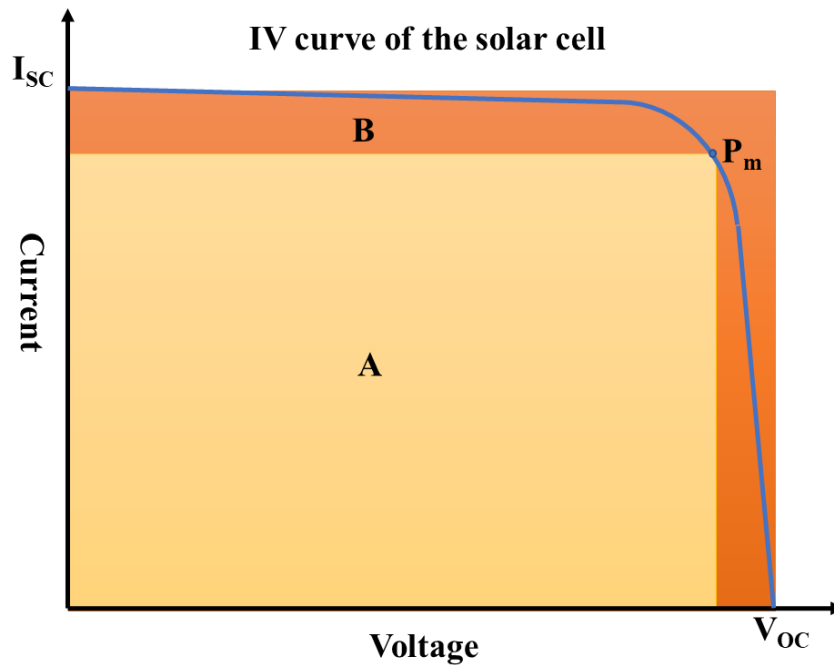


**Figure 1.2.** A typical IV curve of a solar cell.

### 1.2.1. Open-Circuit Voltage ( $V_{OC}$ )

In solar cells, open-circuit voltage ( $V_{OC}$ ) is the voltage between the positive and negative electrodes of the solar cell while these two electrodes are not attached to an external circuit. The unit of the open circuit voltage is volts (V). As shown in Figure 1.2, open circuit voltage is the voltage at the intersection of the IV curve and the horizontal axis, which is the maximum voltage that the PV can produce. From the equation 1.1, it is apparent that the open-circuit voltage is affected by temperature, the dark saturation current, and light-generate current. In real

photovoltaic devices, there are other parameters impacted on the open-circuit voltage, such as the series resistance and various shunt.

$$V_{oc} = \frac{nkT}{q} \ln \left( \frac{I_L}{I_0} + 1 \right) \quad (1.1)$$

$I_0$ - Dark Saturation Current;  $I_L$ - Light Generated Current;  $n$ - Ideality Factor;  $T$ - Temperature;  $q$ - Electronic charge;  $k$  - Boltzmann constant.

### 1.2.2. Short-Circuit Current ( $I_{sc}$ )

When the positive and negative electrodes of the solar cell short-circuited so that the voltage ( $U$ ) is 0, the current at this moment is the short-circuit current of the device. In Figure 1.2, the short-circuit current is the intersection point between the IV curve and the vertical axis. The unit of the short-circuit current is ampere (A). And the short-circuit current ( $I_{sc}$ ) of the solar cell related to the area of the solar cell, the light intensity, the spectrum of the incident light, the optical properties, and the collection probability. Typically, researchers use the short-circuit current density ( $J_{sc}$  in  $\text{mA}/\text{cm}^2$ ) instead of short-circuit current to eliminate the dependence on the solar cell area.

### 1.2.3. Peak Power ( $P_m$ )

Peak power ( $P_m$ ) is the maximum power output of the solar cell. As shown in Figure 1.2, the peak power is obtained at the intersection of region A and the IV curve of the solar cell, that is, the  $P_m$  is equal to the product of the peak current and the peak voltage. The formula is shown in equation 1.2. The unit of peak power is w (Watts). The peak power of a solar cell varies

depending on the solar irradiance, solar spectral distribution, and working temperature of the cell.

$$P_m = I_m \times U_m \quad (1.2)$$

$P_m$  – Peak power;  $I_m$  – Peak current;  $U_m$  – Peak voltage

#### 1.2.4. Fill Factor (FF)

The ratio of the maximum power to the product of the open-circuit voltage and the short-circuit current is defined as the fill factor ( FF ) which is an important parameter for evaluating the solar cell performance, as shown in equation 1.3. It is also the ratio of area B to area A (FF=B/A) in Figure 1.2.

$$FF = \frac{B}{A} = \frac{(I_m \times U_m)}{(I_{SC} \times U_{OC})} = \frac{P_m}{(I_{SC} \times U_{OC})} \quad (1.3)$$

FF – Fill Factor;  $I_m$  – Peak current;  $U_m$  – Peak voltage;  $I_{SC}$  – Short circuit current;  $V_{OC}$  – Open circuit voltage;  $P_m$  – Peak power;

#### 1.2.5. Conversion Efficiency ( $\eta$ )

The conversion efficiency of a solar cell is the percentage of energy output from the solar cell and the applied energy from the sun, defined as equation 1.4. It represents the ability of a photovoltaic device to convert incident light into electricity. The higher the  $\eta$  value, the better the photovoltaic performance.

$$\eta = \frac{V_{oc}I_{sc}FF}{P_{in}} \quad (1.4)$$

$V_{oc}$  – Open-circuit voltage;  $I_{sc}$  – Short-circuit current;  $FF$  – Fill factor;  $\eta$  – Power conversion efficiency.

### 1.3. Material Options for Thin Film Solar Cells

The main purpose of the PV study is to get the maximum conversion efficiency which is affected by several main factors including the incident energy of sunlight and the options of light absorber materials. In general, the light absorbing materials used in thin film solar cells are required to have good optical properties such as a large absorption coefficient and a suitable optical band gap.

#### 1.3.1. Absorption Coefficient

When light propagates through the medium, part of incident light that is absorbed by the material, causing the light intensity to decay with the propagation distance (depth of penetration). This phenomenon is called light absorption. Establishing a model that monochromatic light travels through a semiconductor, the function of the exponential decay of this light behave as equation 1.5 [19].

$$F(x) = F(x_0)e^{-\alpha(x-x_0)} \quad (1.5)$$

$F(x)$  – Intensity at a point  $x$  below the surface of a semiconductor;  $F(x_0)$  – Intensity at a surface point  $x_0$ ;  $\alpha$  – Absorption coefficient, which is a function of the wavelength of light and extinction coefficient ( $\kappa$ ), is defined as equation 1.6.

$$\alpha = \frac{4\pi f k}{c} \quad (1.6)$$

$f$  – Frequency of the monochromatic light, which is equal to the ratio of the velocity of the light wave ( $v$ ) to the wavelength of this light ( $\lambda$ );  $c$  – Speed of light;  $\pi$  – A constant ( $\approx 3.14$ );  $\kappa$  – Extinction coefficient, which is corresponding to the index of refraction  $n$  that merely determines how much light is absorbed by the material.

From equations 1.5 and 1.6, it is good to know that the absorption coefficient is affected by both the incident light and the intrinsic qualities of the material. In addition, the absorption coefficient is corresponding to the band gap which is an important optical parameter of semiconductor, as shown in equation 1.7.

$$\alpha = \frac{A\sqrt{hf - E_g}}{hf} \quad (1.7)$$

$A$  – A constant determined by the electronic band structure;  $h$  – Planck constant;  $f$  – Frequency of the light;  $E_g$  – Band gap of the semiconductor.

Conversely, the band gap of a material can be determined from the absorption spectrum using this equation. From an absorption spectrum, we can get the photon energy ( $E$ ) using equation 1.8 and obtain the absorption coefficient ( $\alpha$ ) of the material using equation 1.9. The two variables of  $h\nu$  and  $(\alpha h\nu)^{1/r}$  are plotted on two axes, respectively, where  $h\nu$  is the x-axis and  $(\alpha h\nu)^{1/r}$  is the y-axis. By extrapolating the linear region of this plot down to zero absorption, we can get the optical band gap of this material.

$$E = h\nu = h\frac{c}{\lambda} \quad (1.8)$$

$$\alpha = 2.303\frac{A}{t} \quad (1.9)$$

$h\nu$ -Photon energy;  $c$ - Speed of light;  $h$ - Planck constant.

$\alpha$  – Absorption coefficient;  $t$ - Sample thickness;  $A$ -Absorbance.

### 1.3.2. Optical Band Gap ( $E_g$ )

The energy of electrons in solids is not continuous but discontinuous energy bands. Generally, the band originally occupied by the valence electrons is the valence band, whereas the band that valence electrons can transmit into from the valence band is conduction band. The minimum energy difference between the conduction band and the valence band is so-called band gap. As displayed in Figure 1.3, the band gap of metal is zero, while the insulator has a maximum band gap and the semiconductor has a moderate band gap. In this diagram, the Fermi level is the chemical potential of electrons at absolute zero.

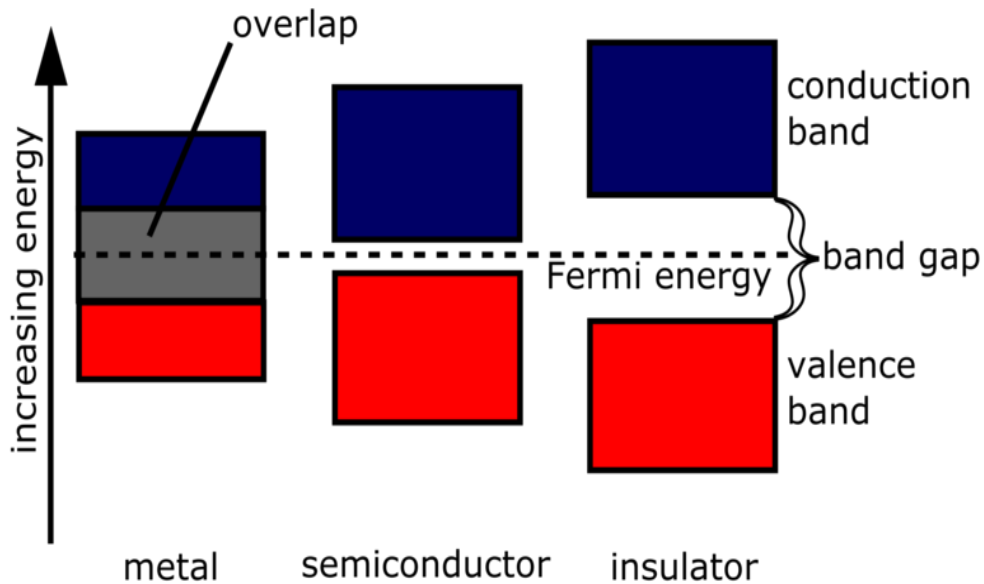


**Figure 1.3.** A band gap diagram showing the varied sizes of band gaps for conductors, semiconductors, and insulators <sup>[20]</sup>.

In solar cells, the value considered is the optical band gap of the semiconductor, which is the minimum energy required to excite electrons from the valence band to the conduction band, symbolized by  $E_g$ . The optical band gap determines the proportion of the solar spectrum absorbed by the photovoltaic cell <sup>[21]</sup>. The optical band gap of a semiconductor consists of two forms: the direct band gap and the indirect band gap as shown in Figure 4a and 4b.

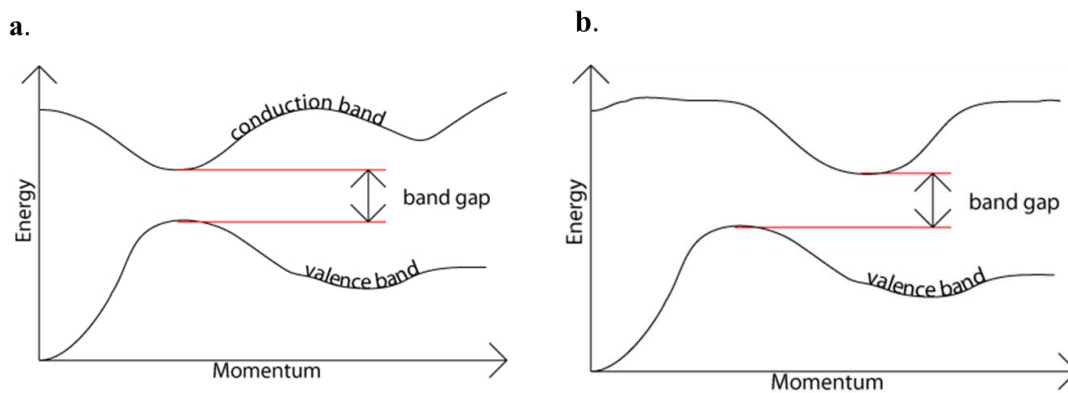


**Figure 1.4.** (a) Direct band gap diagram; (b) Indirect band gap <sup>[22]</sup>.

If the bottom of the conduction band and the top of the valence band is at the same value of the electron momentum (k-vector), the band gap is referred to as direct band gap, as shown in Figure 1.4 (a). In contrast, the material with different k-vector values at the bottom of the conduction band and at the top of the valence band, as shown in Figure 1.4 (b), possess an indirect band gap. Whether the material has a direct band gap or an indirect band gap can intensively affect its optical and electrical properties. As mentioned earlier, semiconductors with direct band gap can convert photons into electron-hole pairs more easily than materials with the

indirect band gap, since photogenerated electrons of semiconductors with indirect band gap require additional energy to change the momentum.

Furthermore, the conversion efficiency can be calculated as a function of the band gap energy, and the result is shown in Figure 1.5. It should be noted that AM in this figure represents Air Mass spectra. AM0 means the sun radiation doesn't pass through the Earth' atmosphere, which is the spectrum of space. AM1.5G is the most common testing condition, referring to the  $1000\text{W}\cdot\text{m}^{-2}$  light incident at  $48^\circ$  to the surface normal. From Figure 1.5, it is well known that the required optical band gap of the light absorber material for thin film solar cells is between 1.0 and 1.6 eV.

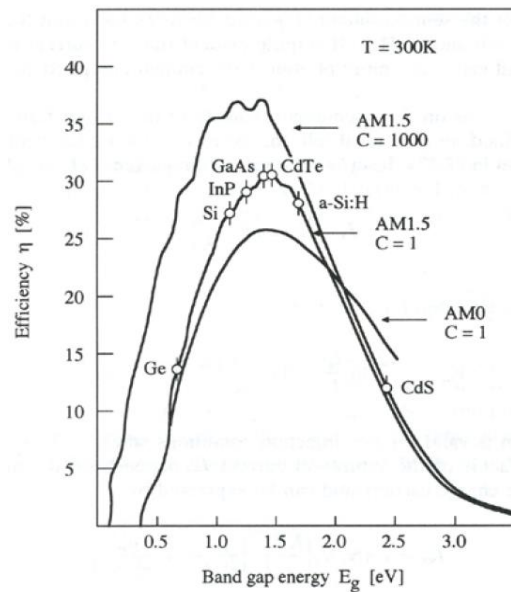


**Figure 1.5.** Ideal solar cell efficiency as a function of the band gap energy for the spectral distribution AM0 and AM1.5 [23].

## **1.4. Fe<sub>2</sub>GeS<sub>4</sub> Absorber Layer and Fe<sub>2</sub>GeS<sub>4</sub> Based Solar Cells**

As mentioned previously, a large number of inorganic materials have successfully applied to thin film solar cells such as CdTe, CIGS, CZTS, CIS, and so on. Most of these semiconductor materials have a direct band gap, which makes them have a higher absorption coefficient than silicon with an indirect band gap. This means that the required light absorbing materials will be reduced, resulting in a thinner solar cell. With the development of semiconductor research, scientists found that nanomaterials have a larger surface area than the bulk materials, providing more reaction sites. At the same time, the small size of nanomaterials offers a predominant absorption ability due to the size dependence of the optical band gap. Such distinct features make the nanomaterials to be the ideal candidates for the semiconductors.

Therefore, nano-semiconductor materials with different crystal structures, sizes, shapes, and elemental compositions have gradually become the focus of much academic research on thin film solar cells.

### **1.4.1. Fe<sub>2</sub>GeS<sub>4</sub> (FGS)**

Fe<sub>2</sub>GeS<sub>4</sub> (FGS) is emerging as a promising light absorbing material because it not only has a high absorption coefficient ( $>10^5 \text{ cm}^{-1}$ ) and a direct band gap (1.4 eV) suitable for photovoltaic applications but also has better sustainability<sup>[24]</sup>. All these excellent optoelectronic properties of FGS highlighted its potential for photovoltaic application. Although FGS is relatively new material, several published papers have presented that FGS materials could be prepared using both the solid-state method and the solution-phase method. The prepared FGS has

an olivine crystal structure which crystallizes with Pnma orthorhombic symmetry, as shown in Figure 1.6 <sup>[25]</sup>.

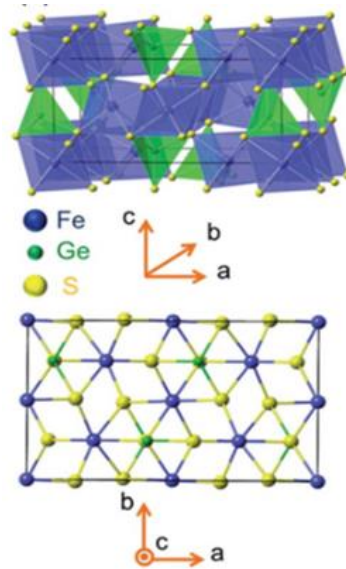


**Figure 1.6.** Fe<sub>2</sub>GeS<sub>4</sub> crystal structure <sup>[25]</sup>.

In my work, I have prepared FGS-based dye-sensitized solar cells to investigate the potential of the FGS in photovoltaic applications.

#### 1.4.2. Dye-Sensitized Solar Cell (DSSC)

Early dye-sensitized solar cells used a compressed ZnO or TiO<sub>2</sub> layer as the electrode, resulting in low conversion efficiency of about 1.5% <sup>[26, 27]</sup>. Until 1991, Grätzel and O'Regan used mesoporous TiO<sub>2</sub> thin film instead of the compact TiO<sub>2</sub> layer to form an improved dye-sensitized solar cell with a conversion efficiency of 7.9% <sup>[28]</sup>.

A typical dye-sensitized solar cell is shown in Figure 1.7. Its construction is as follows:

- 1) Working electrode (WE). The glass protective substrate is coated with fluorine or indium doped  $\text{SnO}_2$  to form a conductive FTO or ITO substrate. Next, the prepared conductive substrate is printed with  $\text{TiO}_2$  paste. Then, this  $\text{TiO}_2$  thin film is sensitized with the dye. The resulting dye-sensitized  $\text{TiO}_2$  thin film is the working electrode.
- 2) Counter electrode (CE). Similarly, a glass protective substrate is coated with fluorine or indium doped  $\text{SnO}_2$  to form conductive FTO or ITO substrate. Then, the prepared conductive substrate is deposited with the catalyst layer. The resulting thin film is the counter electrode.
- 3) Electrolyte. The electrolyte is an important component of the dye-sensitized solar cell, which is used to transport electrons from the counter electrode back into the photogenerated holes in the dye to promote the dye regeneration. In other words, the electrolyte helps the dye and itself to be continuously regenerated. Until now, there have been many types of electrolyte such as iodide/triiodide, tetra-*n*-butylammonium ( $\text{TBA}^+$ ), 1,2-dimethyl-3-propylimidazolium ( $\text{DMPI}^+$ ), etc <sup>[29]</sup>.

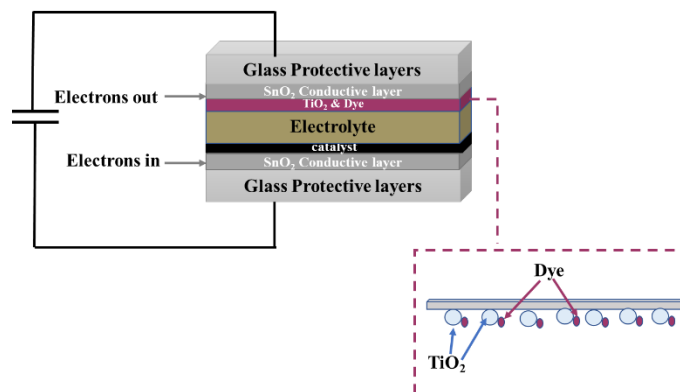


**Figure 1.7.** Dye-sensitized solar cell (DSSC).

As shown in Figure 1.8, the working mechanism of the dye-sensitized solar cell includes three processes <sup>[30]</sup>:

1. When light shines on the solar cell, photons of the incident light are absorbed by the dye. The dye is then excited to produce excitons ( $D^*$ ).
2. Excitons ( $D^*$ ) release electrons into the conduction band of  $TiO_2$ , meanwhile, leaving holes ( $D^+$ ) in the dye.
3. The released electrons move to the conductive layer and then go through the external circuit to perform the electrical work. The dye is regenerated by accepting the electron from the reduced species in the electrolyte.
4. Then the electrons reach the counter electrode. With the help of the catalyst, the electrons enter into the electrolyte and reduce the oxidized component of the redox couple.

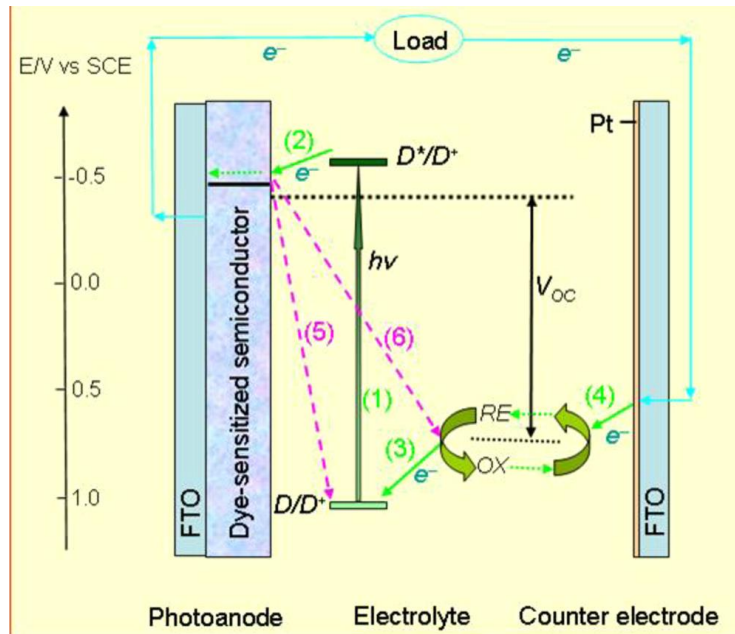


**Figure 1.8.** Operating principle of dye-sensitized solar cells <sup>[30]</sup>.

## CHAPTER 2. LITERATURE REVIEW

In the past few decades, Fe dichalcogenides  $\text{FeX}_2$  ( $\text{X}=\text{S}, \text{Se}, \text{Te}$ ) nanomaterials and the ternary compounds derived from them have been considered as potential semiconductors due to their high absorption coefficient, suitable band gap, the abundant Fe content on the earth, and other great properties.

### 2.1. Iron Dichalcogenides $\text{FeX}_2$ ( $\text{X}=\text{S}, \text{Se}, \text{Te}$ )

Iron dichalcogenide, composed of one iron element and two chalcogen anions, are a group of inorganic chemical compounds. Fe element is the fourth most abundant element in the earth's crust, accounting for five percent in the earth by weight, only less than oxygen, silicon and aluminum<sup>[31]</sup>. Chalcogens are generally known as oxygen family, including all the elements in group VIA of the periodic table. However, the iron chalcogenides we usually mentioned are sulfides, selenides, and tellurides compounds, rather than oxides and polonium compounds which have extremely strong non-metallic and strong metallic properties, respectively<sup>[32]</sup>. According to the different chalcogens, these iron dichalcogenides can be classified into disulfides, diselenides, ditellurides, or multi-chalcogen chalcogenides.

The physical and chemical properties of sulfur, selenium, and tellurium are shown in the red circled area of Table 2.1. As shown in Table 2.1, the order of the abundance of chalcogen in the crust is  $\text{S} > \text{Se} > \text{Te}$ , indicating that sulfur is the most abundant chalcogen on the earth except oxygen. Simultaneously, Te has a median lethal dose ( $\text{LD}_{50}$ ) of 83 mg/kg, showing the most

toxicity compared to S and Se <sup>[33]</sup>. Thus, much attention has been attracted to Fe sulfide and Fe selenide.

Considering comprehensively, pyrite (FeS<sub>2</sub>) has been considered as an ideal material for manufacturing photovoltaic devices in recent decades.

**Table 2.1.** Some physical-chemical properties of S, Se and Te <sup>[33]</sup>.

	Oxygen(O)	Sulfur(S)	Selenium (Se)	Tellurium (Te)	Polonium (Po)
Atomic Mass	15.999	32.07	78.96	127.6	210
Abundance in earth Crust (%)	46	0.042	5×10 <sup>-6</sup>	1×10 <sup>-7</sup>	N/A
Toxicity	> 50 (kPa)	LD <sub>50</sub> Oral – rat-> 2,000 mg/kg	LD <sub>50</sub> Oral -rat - 6,700 mg/kg	LD <sub>50</sub> Oral – rat 83 mg/kg	LD <sub>50</sub> Oral 50 mg/kg
Electronic Structure	[He] 2s <sup>2</sup> 2p <sup>4</sup>	[Ne]3s <sup>2</sup> 3p <sup>4</sup>	[Ar]3d <sup>10</sup> 4s <sup>2</sup> 4p <sup>4</sup>	[Kr]4d <sup>10</sup> 5s <sup>2</sup> 5p <sup>4</sup>	[Xe]4f <sup>14</sup> 5d <sup>10</sup> 6s <sup>2</sup> 6p <sup>4</sup>
Melting Point (°C)	-218.8	119.0	220.5	449.8	254
Boiling Point (°C)	-183.0	444.6	694.8	989.8	962
Density (g/cm <sup>3</sup> )	1.14	2.03	4.82	6.25	α-9.916 β-9.398
Atomic Radius (10 <sup>-10</sup> m)	0.6	1.00	1.20	1.40	1.68
Electronegativity (Pauling's data)	3.44	2.58	2.55	2.10	2.0
<b>Standard Redox Potential (V)</b>	<b>+0.40</b>	<b>-0.48</b>	<b>-0.92</b>	<b>-1.14</b>	<b>N/A</b>

### 2.1.1. Properties of Iron Disulfide (FeS<sub>2</sub>)

Iron disulfide (FeS<sub>2</sub>) has two different polymorphs, including marcasite (m-FeS<sub>2</sub>) and pyrite (p-FeS<sub>2</sub>). From Figure 2.1, it is known that p-FeS<sub>2</sub> is a typical AB-type cubic compound

whose structure is similar to that of NaCl type, in which  $\text{Fe}^{2+}$  ion bonded to six nearest S atoms in a twisted octahedral site to form  $\text{FeS}_6$  unit, whereas S anion bound by three Fe atoms and another S atom in a distorted tetrahedral environment<sup>[34]</sup>. In this distorted  $\text{FeS}_6$  unit, the point symmetry declined from cubic ( $\text{O}_h$ ) to trigonal ( $\text{C}_{3i}$ ). In such a cubic structure of pyrite ( $\text{p-FeS}_2$ ), the deformed octahedral  $\text{FeS}_6$  unit share the common corner. Although marcasite ( $\text{m-FeS}_2$ ) with orthorhombic structure also possess distorted octahedra  $\text{FeS}_6$  unit and distorted tetrahedral site around S atoms, nevertheless, the  $\text{FeS}_6$  unit in  $\text{m-FeS}_2$  is edge-shared, as shown in Figure 2.2<sup>[35]</sup>.

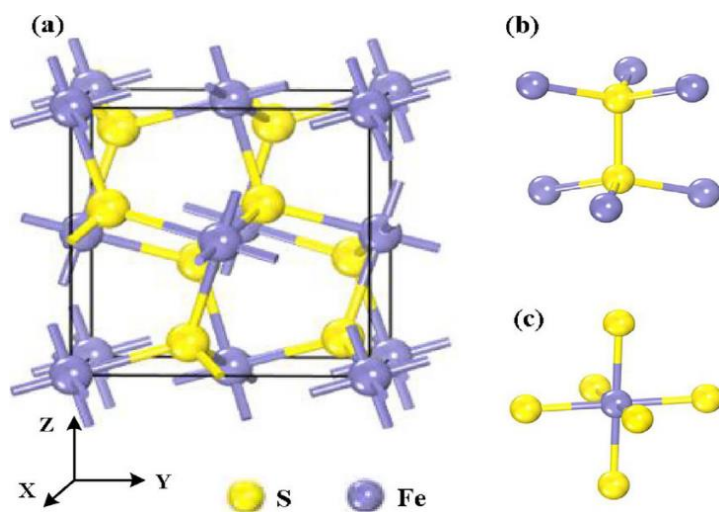


**Figure 2.1.** Pyrite ( $\text{FeS}_2$ ) crystal structure<sup>[34]</sup>.

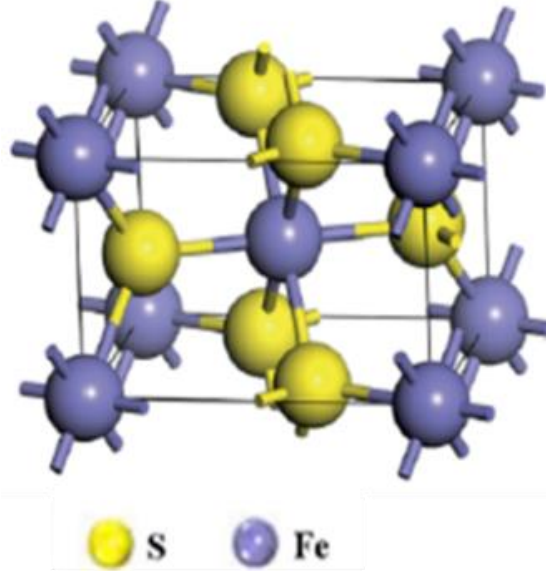


**Figure 2.2.** Marcasite ( $\text{FeS}_2$ ) crystal structure <sup>[35]</sup>.

Base on the Fe electronic configuration of  $[\text{Ar}] 3d^6 4s^2$ , the splitting of the  $d$ -orbitals occurs in both p- $\text{FeS}_2$  and m- $\text{FeS}_2$ . According to the crystal field theory, the original 3d orbitals of Fe in p- $\text{FeS}_2$ , with equal energy, are split into two groups, including stabilized  $d_{xy}$ ,  $d_{xz}$ ,  $d_{yz}$  state with higher energy, in terms of  $t_{2g}$ , and destabilized  $d_z^2$ ,  $d_{x^2-y^2}$  state with lower energy, symbolized as  $e_g$ , which is shown in Figure 2.3 <sup>[36]</sup>. In this crystal field, all the six d electrons will first occupy the lower energy  $t_{2g}$  orbit, while the higher energy  $e_g$  orbital are empty, forming a low-spin compound. Furthermore, in p- $\text{FeS}_2$  structure, the  $e_g^*$  antibonding orbitals of Fe and  $\sigma^*$  antibonding orbital of S are hybridized to form the conduction band (CB), whereas the  $t_{2g}$  nonbonding orbitals of Fe hybridize with p orbitals of S to form the valence band (VB), resulting a band gap of 0.95 eV. As shown in Figure 2.4, an energy level scheme of p- $\text{FeS}_2$  was derived by A Schlegel and P Wachter in 1976, indicating an energy gap of 0.95eV which is suitable for photovoltaic application <sup>[37]</sup>.

Despite both p-FeS<sub>2</sub> and m-FeS<sub>2</sub> are low-spin compounds, however, the Fe d orbitals in m-FeS<sub>2</sub> exhibit increased splitting at both t<sub>2g</sub> and e<sub>g</sub> levels due to its lower symmetry than that of p-FeS<sub>2</sub>, as shown in Figure 2.3<sup>[36]</sup>. The different crystal-field splitting and the low-spin configuration of Fe<sup>2+</sup> in m-FeS<sub>2</sub> leads one to speculate that E<sub>g</sub> for m-FeS<sub>2</sub> should be less than E<sub>g</sub> for p-FeS<sub>2</sub><sup>[38]</sup>. In addition, the band gap in m-FeS<sub>2</sub> is formed by the Fe 3d-Fe 3d transition, which presented a band gap of 0.34 eV in early studies<sup>[38-40]</sup>.

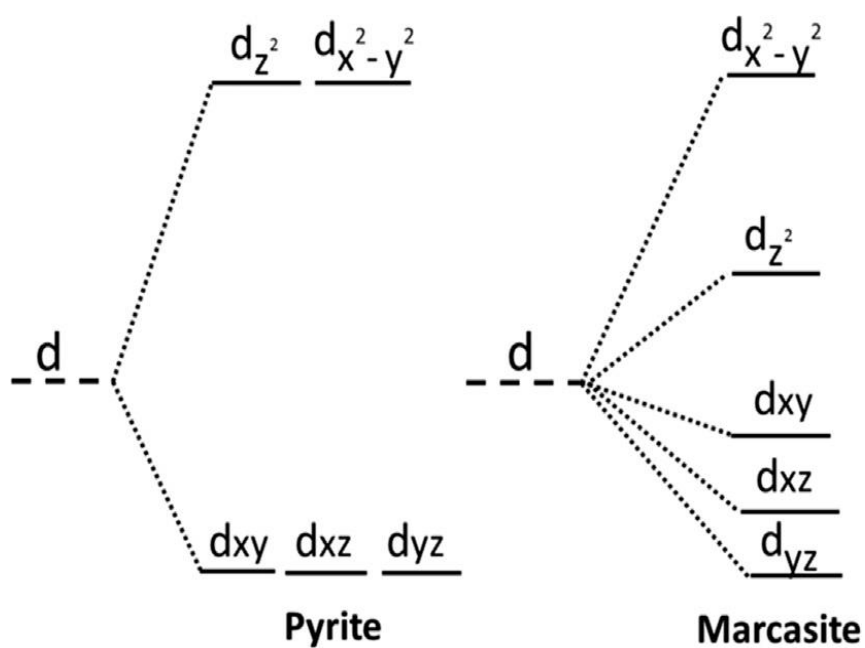


**Figure 2.3.** 3d orbital splitting schemes in pyrite and marcasite<sup>[36]</sup>.

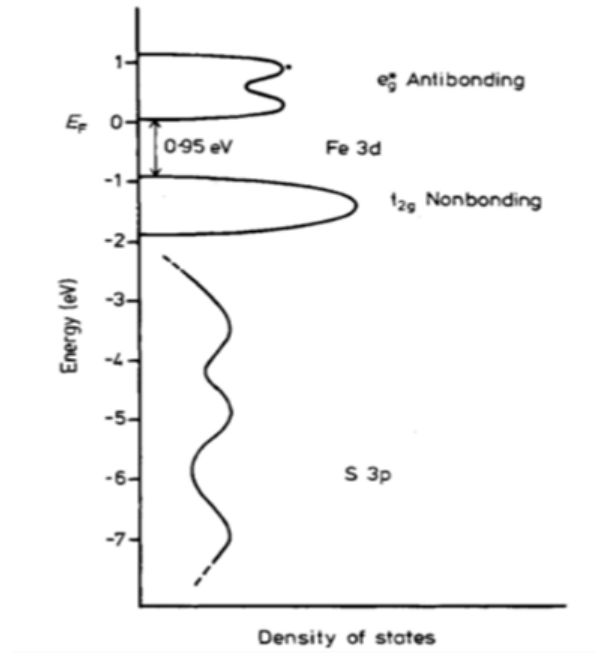


**Figure 2.4.** Energy level scheme of FeS<sub>2</sub> [37].

However, Sun et al. (2011) found the band gap of m-FeS<sub>2</sub> is not less than p-FeS<sub>2</sub>, as displayed in Table 2.2. These band gap values are calculated using LDA, GGA-PBE, GGA-AM05, HSE06, and  $\Delta$ -sol models [41].

**Table 2.2.** Band gap (in eV) and k-points at VB and CB edges. HSE06 and  $\Delta$ -sol gaps are obtained at the experimental lattice constants [41].

	Pyrite			Marcasite		
	$E_g$	VB	CB	$E_g$	VB	CB
LDA	0.22	(0.4375,0,0)	(0,0,0)	0.88	(0.375,0,0)	(0,0.5,0.5)
PBE	0.40	(0.4375,0,0)	(0,0,0)	0.81	(0.4375,0,0)	(0,0.5,0.5)
PBE+ $U$	1.03	(0.4375,0,0)	(0,0,0)	1.18	(0.4375,0,0)	(0,0.5,0.5)
AM05	0.29	(0.4375,0,0)	(0,0,0)	0.88	(0.375,0,0)	(0,0.5,0.5)
AM05+ $U$	0.72	(0.4375,0,0)	(0,0,0)	1.18	(0.375,0,0)	(0,0.5,0.5)
HSE06	2.76	(0.5,0.5,0)	(0,0,0)	2.72	(0.5,0,0)	(0,0.5,0)
$\Delta$ -sol	1.3			1.2		
Experiment	0.95 <sup>a</sup>			0.34 <sup>b</sup>		

In addition to a suitable band gap for photovoltaic application, p-FeS<sub>2</sub> also possess high light absorption. The comparison of the absorption length  $L = 1/a$  for the different semiconductor materials in Figure 2.5 clearly shows that FeS<sub>2</sub> has the shortest absorption length, which means that FeS<sub>2</sub> is the least used material when absorbing the same amount of light.

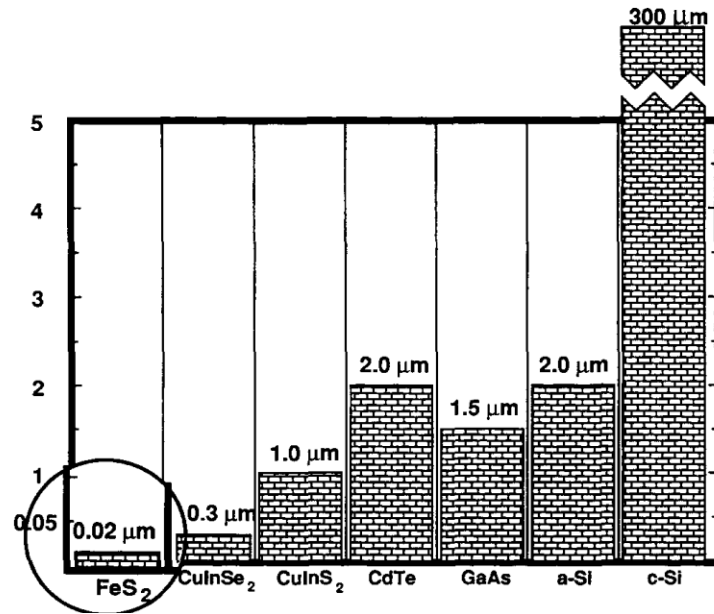


**Figure 2.5.** Comparison of the absorption lengths  $L = 1/a$  for different semiconductors materials [42].

Thereby, p-FeS<sub>2</sub> has been extensively investigated as a semiconductor material during recent years, regarding not only its high absorption coefficient ( $>10^5 \text{ cm}^{-1}$ ) and a band gap of  $\sim 0.95 \text{ eV}$ , but also its natural abundance [43].

### 2.1.2. Problems of p-FeS<sub>2</sub> Based Solar Cells

After decades of efforts, p-FeS<sub>2</sub> based photovoltaic devices still exhibit deficient performance, although it has exceptional theoretical optoelectronic properties. Inconsistent with

theoretical properties, the highest record of the open-circuit voltage of the pyrite single crystal photoelectrochemical cell is only 0.2V [42]. Further, in the photovoltaic device, the p-FeS<sub>2</sub> thin film worked as the p-type, but the single crystal performed as the n-type [44,45]. Moreover, the p-FeS<sub>2</sub> thin film in the photoelectrochemical cell does not exhibit a photoelectrochemical response. Therefore, several hypotheses have been proposed to explain the reason why the photovoltaic performance of the p-FeS<sub>2</sub>-based solar cells is poor.

First, the presence of marcasite phase in pyrite. In 1976, Gronvold reported that the marcasite-to-pyrite transformation occurred under certain conditions [46]. Before 2011, it is generally believed that the lower band gap of marcasite is one of the main factors for the poor photovoltaic performance of p-FeS<sub>2</sub>-based photovoltaic devices. However, Sun et al. pronounced that the calculated band gap of m-FeS<sub>2</sub> was not less than that of p-FeS<sub>2</sub>, indicating that the presence of m-FeS<sub>2</sub> was not the major negative factor determining the poor photovoltaic performance of p-FeS<sub>2</sub>-based solar cell devices [41].

Second, phase coexistence and thermal instability of p-FeS<sub>2</sub> [47, 24]. As shown in Figure 2.6, the formation enthalpies ( $\Delta H$ ) of S-deficient phases including Fe<sub>11</sub>S<sub>12</sub>, Fe<sub>7</sub>S<sub>8</sub>, Fe<sub>9</sub>S<sub>10</sub>, and Fe<sub>3</sub>S<sub>4</sub> are lower than that of FeS and FeS<sub>2</sub>. Basically, the Fe<sub>11</sub>S<sub>12</sub>, Fe<sub>7</sub>S<sub>8</sub> and Fe<sub>9</sub>S<sub>10</sub> can be classified as pyrrhotite, while Fe<sub>3</sub>S<sub>4</sub> has a common name of Greigite. Through the analysis of the calculated formation energy of intermediate S-deficient phases, Yu et al. (2011) pointed out that the intermediate Fe-deficient phases of pyrrhotite (Fe<sub>1-x</sub>S, X = 0 to 0.2) and greigite (Fe<sub>3</sub>S<sub>4</sub>) could be formed spontaneously when the troilite FeS (X=0) is formed during growth, resulting in a phase coexistence [24].

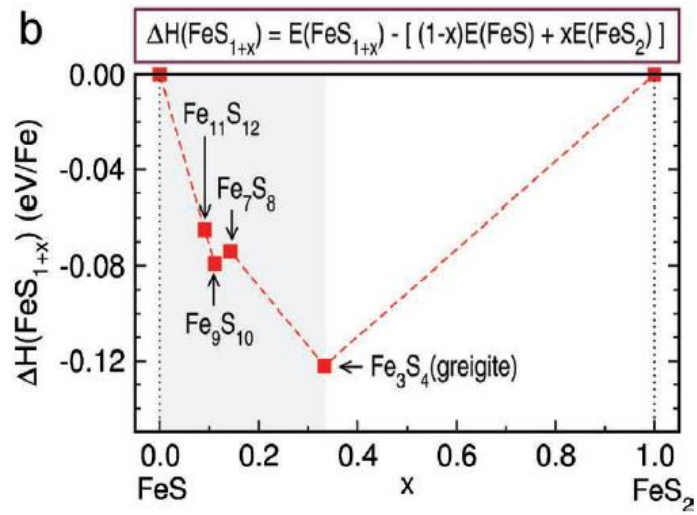


**Figure 2.6.** Calculated formation energy of intermediate S-deficient phases <sup>[24]</sup>.

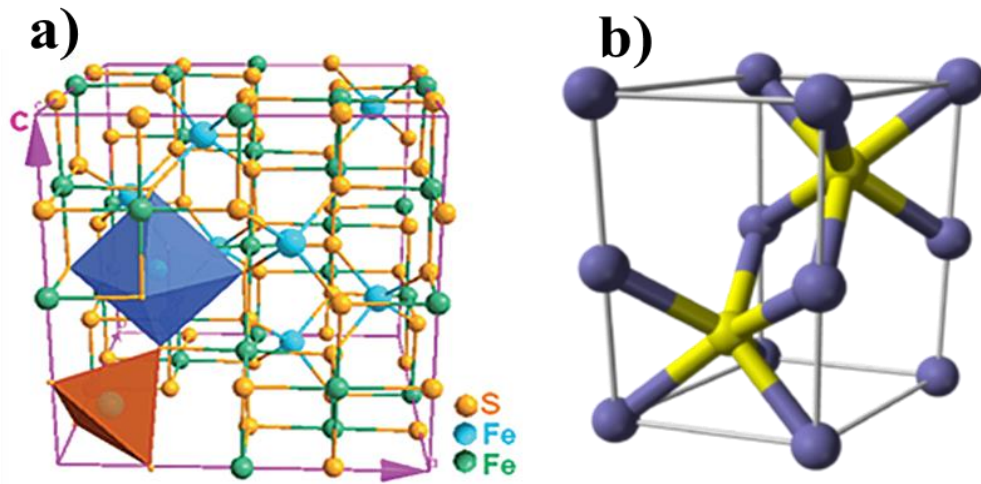


**Figure 2.7.** Crystal structure. **a)** Greigite <sup>[48]</sup>; **b)** Pyrrhotite based NiAs structure <sup>[49]</sup>.

Greigite ( $\text{Fe}_3\text{S}_4$ ) possess a cubic unit cell in which a portion of Fe ion is in the tetrahedral A-sites and another portion of the Fe cation is in the octahedral B-sites, as shown in Figure 2.7 (a) <sup>[48]</sup>. From the electronic structure, it is known that a Greigite having spinel structure can be

considered as a conductor to electrons of one spin orientation but an insulator or a semiconductor to those of the opposite orientation <sup>[50]</sup>. Basically, all the pyrrhotite-4M Fe<sub>7</sub>S<sub>8</sub>, Pyrrhotite-5H or 7H Fe<sub>9</sub>S<sub>10</sub>, and Pyrrhotite-6M Fe<sub>11</sub>S<sub>12</sub> phases have a basic crystal structure of NiAs structure, in which Fe cation is bonding to six S anions at the octahedral site (FeS<sub>6</sub>), as shown in Figure 2.7 (b) <sup>[49]</sup>. Similar to p-FeS<sub>2</sub>, the Fe 3d orbitals of the pyrrhotite split into a higher energy level e<sub>g</sub> and a lower energy level t<sub>2g</sub>. However, Nesbitt et al. determined that the orbital separation energy ( $\Delta$ ) of Fe ions in pyrrhotite is smaller than the spin-pairing energy ( $P$ ), resulting in a high-spin electron configuration of Fe atoms in pyrrhotite <sup>[51]</sup>.

Wang et al. (2005) reported that the concentration of impurities and the temperature could alter the band structure of pyrrhotite. The temperature variation of the resistivity of pyrrhotite with different composition in Figure 2.8, clearly exhibits that all pyrrhotite samples present semiconductor properties due to the negative slope of temperature coefficients for resistivity below the transition temperature ( $T_{\beta}$ ). But when the temperature goes above 315 °C, the slope of temperature coefficients for resistivity becomes positive, indicating that the pyrrhotite samples have metallic properties <sup>[52]</sup>.

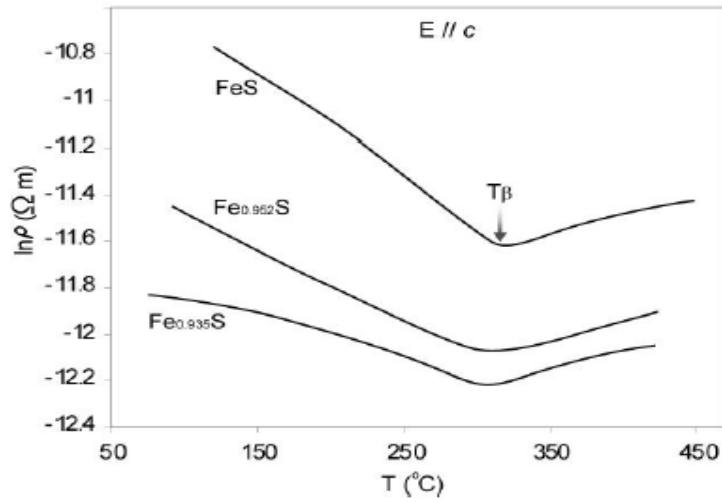


**Figure 2.8.** Temperature variation of the receptivity of pyrrhotite with different compositions [52].

Therefore, we can speculate that the process of pyrrhotite affecting the photovoltaic performance of the p-FeS<sub>2</sub>-based solar cell is as follow: 1) The S-deficient phase pyrrhotite will be spontaneously formed during the formation of pyrite; 2) When the temperature is raised above 315°C, the impurity pyrrhotite will become possessing some metallic properties; 3) The metallic properties of pyrrhotite in pyrite will affect its photovoltaic performance as a semiconductor.

In summary, the instability of the pyrite phase and the resulting intermediate S-deficient pyrrhotite and greigite phases may be responsible for the poor photovoltaic performance of the p-FeS<sub>2</sub> based solar devices.

## 2.2. Ternary Fe Based Chalcogenides Fe<sub>2</sub>GeS<sub>4</sub>

To avoid the phase instability of p-FeS<sub>2</sub>, Yu's group proposed an innovative design, adding a third element (Ge, Si) to p-FeS<sub>2</sub> to form ternary compounds Fe<sub>2</sub>GeS<sub>4</sub> or Fe<sub>2</sub>SiS<sub>4</sub> with a stable olivine structure [24].

### 2.2.1. Properties and Applications of Fe<sub>2</sub>GeS<sub>4</sub> Materials

It is well known that the crystal structure of a material influences numerous chemical and physical properties of the material, such as stability, band gap, and so on. The ternary Fe<sub>2</sub>GeS<sub>4</sub>, with an olivine structure, has a calculated band gap of 1.40 eV and high absorption coefficient, making it a promising light absorbing material for photovoltaic devices.

#### 2.2.1.1. Optoelectronic Property

As aforementioned, the optoelectronic properties of a material are defined as the ability to convert light into electricity, which determines its potential in photovoltaic applications. For optoelectronic conversion, the optical properties like light absorption and band gap are vital factors. So far, several reports have shown that Fe<sub>2</sub>GeS<sub>4</sub> has optoelectronic properties [24,55].

The Fe<sub>2</sub>GeS<sub>4</sub> was firstly investigated to have an olivine crystal structure with orthorhombic symmetry by Vincent et al. [53]. As shown in Figure 2.9 (a), the Fe<sub>2</sub>GeS<sub>4</sub> crystal structure exhibits that the Fe ions octahedrally coordinated with six S anions to form FeS<sub>6</sub> unit while the Ge cations tetrahedrally coordinated with three S atoms [54]. But the Fe ions in Fe<sub>2</sub>GeS<sub>4</sub> can occupy two different sites of 4a and 4c, wherein the Fe-S at 4a site has a shorter bond length

than that of the 4c site. In addition, through either calculating the decomposition enthalpy of  $\text{Fe}_2\text{GeS}_4$  or measuring the TGA of the  $\text{Fe}_2\text{GeS}_4$  pallet, they confirmed the high phase stability of the  $\text{Fe}_2\text{GeS}_4$  material [24]. The diffuse reflectance data of  $\text{Fe}_2\text{GeS}_4$  and  $\text{Fe}_2\text{SiS}_4$  in Figure 2.9 (b) presents that the  $\text{Fe}_2\text{GeS}_4$  crystal possesses a direct band gap of 1.36 eV, which is suitable for PV application. Furthermore,  $\text{Fe}_2\text{GeS}_4$  possess a high calculated absorption coefficient of  $10^5 \text{ cm}^{-1}$  which is shown in Figure 2.9 (c) [24].

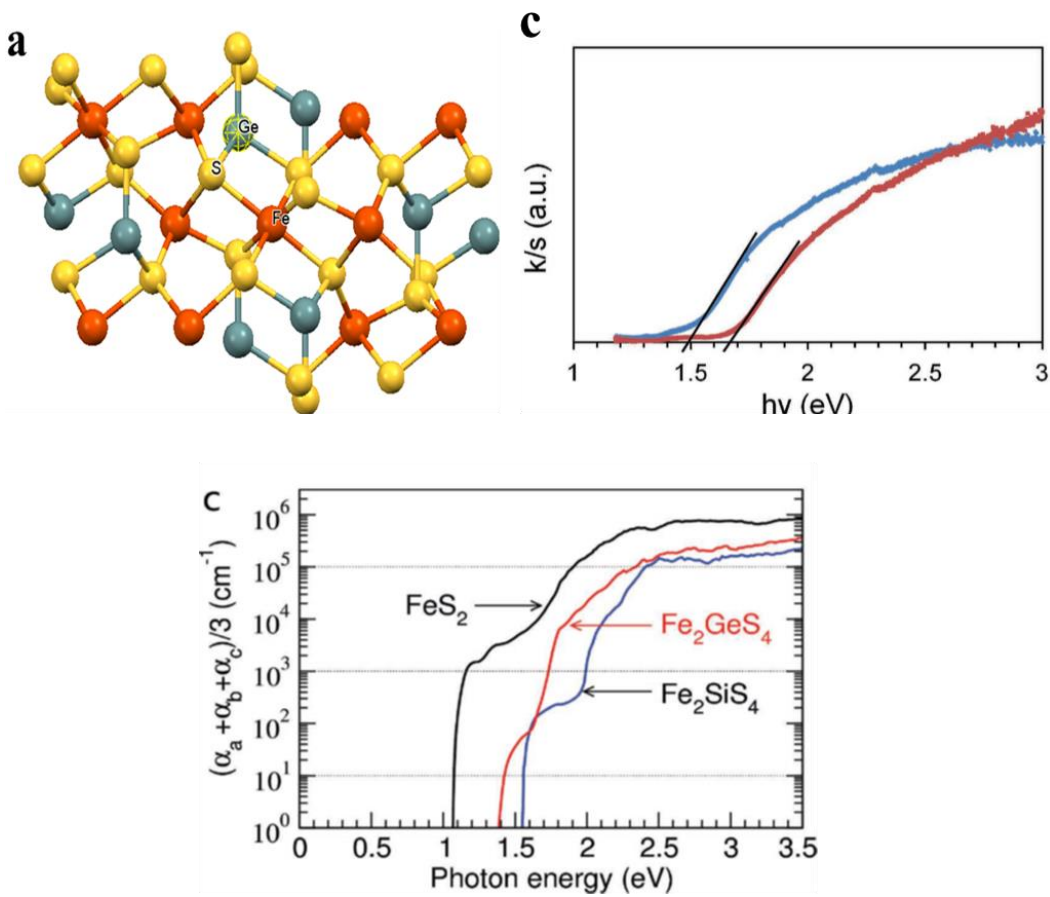


**Figure 2.9.** (a)  $\text{Fe}_2\text{GeS}_4$  crystal structure [54]; (b) Diffuse reflectance data from powders [24]. ( $\text{Fe}_2\text{GeS}_4$  –blue line,  $\text{Fe}_2\text{SiS}_4$  –red line.); (c) Calculated optical absorption coefficients for  $\text{FeS}_2$ ,  $\text{Fe}_2\text{GeS}_4$  and  $\text{Fe}_2\text{SiS}_4$  [24].

Further, a report by Prieto et al. showed a measured photocurrent of  $\text{Fe}_2\text{GeS}_4$  thin films as shown in Figure 2.10, demonstrating that the  $\text{Fe}_2\text{GeS}_4$  thin film has a photoelectrochemical response [55].

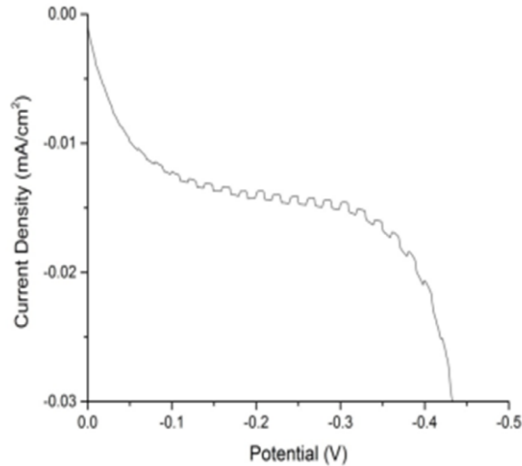


**Figure 2.10.** Photocurrent response in a linear sweep from 0 V to -0.5 V [55].

In summary, all of these investigations have shown that  $\text{Fe}_2\text{GeS}_4$  has exceptional optoelectronic properties and further demonstrate its potential for photovoltaic applications.

### 2.2.1.2. Magnetic Property

The magnetic properties of a material refer to the attraction or exclusion between the material and the external magnetic field. Recently, the nanomaterials with magnetic properties have been extensively studied for the application in biomedical and other fields.

According to the report by Vincent et al.,  $\text{Fe}_2\text{GeS}_4$  has paramagnetic properties in the range of 108-300K and antiferromagnetic properties in the range of 108-69K, as shown in Figure 2.11(a). Nevertheless, when the temperature drops below 69K, the magnetic properties of

Fe<sub>2</sub>GeS<sub>4</sub> turned to weak ferrimagnetic as shown in Figure 2.11 (b). They ascribed this transition from antiferromagnetic to weak ferrimagnetic at 69 K to the slight changes in spin orientation from the b-axis to the a-axis [56]. These investigations were also clarified by both Junod et al. (1995) and Ohgushi et al. (2006), in which the magnetic transitions occurred at 69.5±1 K and 145 K [57,58].

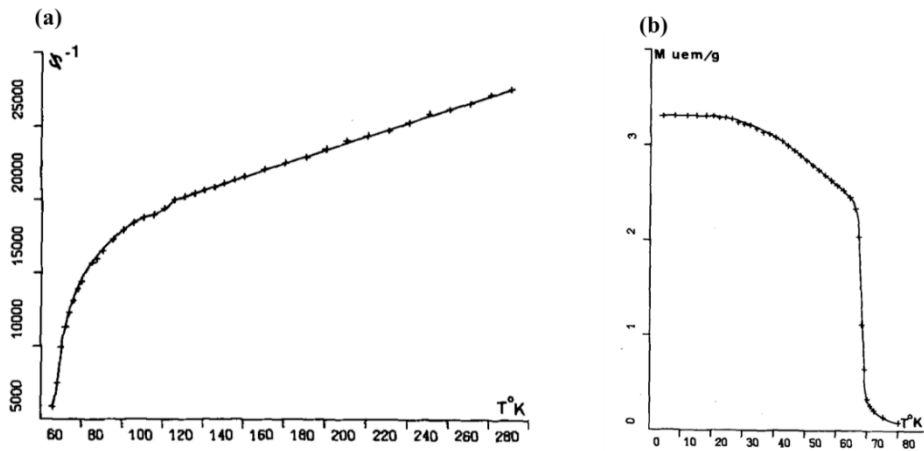


**Figure 2.11.** (a) Inverse susceptibility versus temperature in a 21400 Oe field; (b) Spontaneous magnetization as a function of temperature, in a residual field of 110 Oe [56].

### 2.2.1.3. Thermoelectric Property

The thermoelectric property of a material depends on the thermoelectric efficiency which related to the figure of merit ( $ZT$ ). The function is defined as equation 2.1.

$$ZT = \sigma S^2 T / (k_e + k_l) \quad (2.1)$$

$$\text{Power factor} = \sigma S^2 \quad (2.2)$$

$T$  – Absolute temperature;  $S$  – Seebeck coefficient;  $\sigma$  – Electrical conductivity;  $\kappa_e$  – Thermal conductivity of electrons;  $\kappa_l$  – Thermal conductivity of the lattice (phonons).

Thereby, the ability of a material to convert heat to electricity is related to its electrical conductivity ( $\sigma$ ), Seebeck coefficient ( $S$ ), and thermal conductivity ( $\kappa_e + \kappa_l$ )<sup>[59]</sup>. In addition, the power factor of a material is a useful parameter to determine its ability to generate electrical energy. In the literature, a good thermoelectric material is supposed to have a large electrical conductivity ( $\sigma$ ) and Seebeck coefficient ( $S$ ) but a low thermal conductivity ( $\kappa_e + \kappa_l$ )<sup>[60]</sup>.

$\text{Fe}_2\text{GeS}_4$  emerged as a promising candidate with good thermoelectric performance. a report by Platt et al. (2011) showed that the  $\text{Fe}_2\text{GeS}_4$  material had a thermopower of  $250 \mu\text{V/K}$  at room temperature<sup>[61]</sup>. Then, Gudelli et al. (2016) reported the calculated thermopower ( $S$ ), electrical conductivity ( $\sigma$ ), and power factor of  $\text{Fe}_2\text{GeS}_4$  at 300 K and 500K, respectively. As shown in Figure 2.12 (a), for the hole concentration, even the thermopower of  $\text{Fe}_2\text{GeS}_4$  is declining from 850 to  $250 \mu\text{V/K}$  at both 300 K and 500 K, the thermopower values are still higher than that of the commercial used thermoelectric material  $\text{Bi}_2\text{Te}_3$  whose thermopower is  $225 \mu\text{V/K}$ . As well as the hole carriers, for the electron concentration, the thermopower of  $\text{Fe}_2\text{GeS}_4$  also exhibits high values from  $800\text{--}200 \mu\text{V/K}$ . On the other hand, the electrical conductivity of  $\text{Fe}_2\text{GeS}_4$  in Figure 2.12 (b) exhibits high values of  $10^{16}\text{--}10^{19} \text{ cm}^{-3}$  along b-axis and c-axis for electrons, but low values of  $10^{13}\text{--}10^{16} \text{ cm}^{-3}$  along a-axis, which can attribute to weak covalent bonding along a-axis and the higher parameter of 'a'. Furthermore, the electrical conductivity of  $\text{Fe}_2\text{GeS}_4$  for electrons is higher than that for holes, resulting in distinguish of power factors between electrons and holes as shown in Figure 2.12 (c)<sup>[62]</sup>.

In summary, for  $\text{Fe}_2\text{GeS}_4$  material, the electrical conductivity, thermopower, and power factors were investigated, which exhibited that  $\text{Fe}_2\text{GeS}_4$  possess the potential to develop a thermoelectric material.

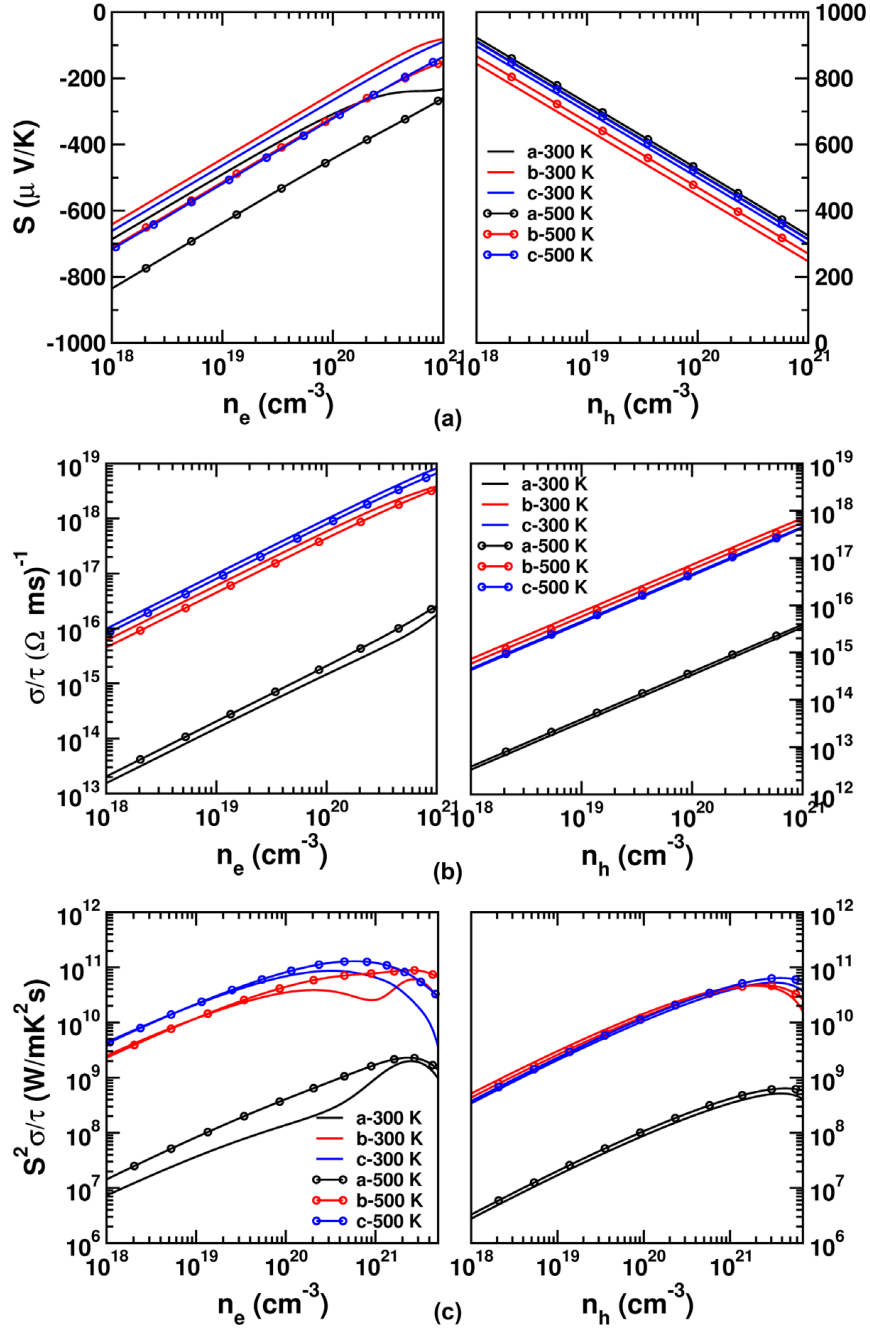


**Figure 2.12.** Calculated (a) thermopower, (b) electrical conductivity scaled by relaxation time and (c) power factor for  $\text{Fe}_2\text{GeS}_4$  <sup>[62]</sup>.

### 2.2.2. Synthesis of Fe<sub>2</sub>GeS<sub>4</sub> Materials via Solid-State Method

In the literature, there have been two main methods for preparing Fe<sub>2</sub>GeS<sub>4</sub> materials, including the solid-state method and solution-phase method.

Generally, a typical solid-state synthesis has two steps, including the preparation of precursors and the sintering process in a furnace, as shown in Figure 2.13, which is consistent with the slang name of ‘shake and bake’<sup>[63]</sup>. Usually, the term ‘shake’ refers to the mixing of precursors, which can be achieved by ball milling or hand grinding. Through ball milling or grinding, large reactant powders become smaller, resulting in an increased surface area of exposure, which is beneficial to the subsequent sintering process. ‘Bake’ means to heat the mixed powder in a furnace, which is consistent with the sintering process.

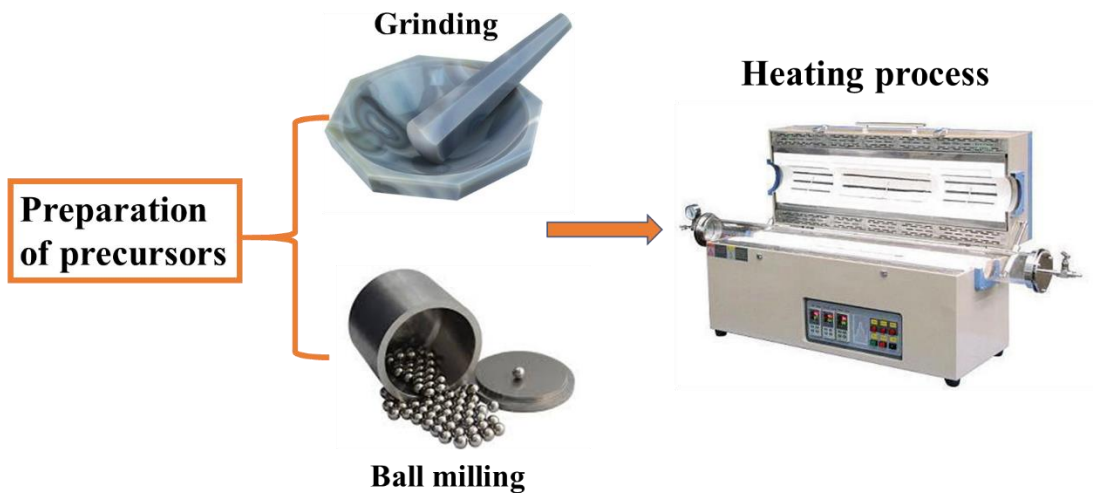


**Figure 2.13.** Schematic illustration of Solid-state synthesis.

### 2.2.2.1. Melting

In early solid-state synthesis, the direct melting method was widely used in the preparation of materials. For example, a report by Vincent group presents that a large  $\text{Fe}_2\text{GeS}_4$  single crystal could be prepared by melting the elemental Fe, Ge, S powders in a quartz tube at  $750^\circ\text{C}$  for one week and then cooling slowly<sup>[53]</sup>. Another report by Junod et al. also presented that a polycrystalline  $\text{Fe}_2\text{GeS}_4$  was prepared using progressive solid-state synthesis, in which the reaction system is heated to  $1200^\circ\text{C}$  with two short pauses at  $600^\circ\text{C}$  and  $800^\circ\text{C}$  respectively<sup>[57]</sup>. Recently, the single crystal  $\text{Fe}_2\text{GeS}_4$  prepared by Yu et al. (2011) using conventional solid-state method showed a measured band gap of 1.36 eV for the first time, which is in good agreement of theoretic value of 1.40 eV<sup>[24]</sup>.

In these three reports,  $\text{Fe}_2\text{GeS}_4$  powders were prepared from elemental Fe, Ge, and S by melting them in vacuum-sealed quartz tubes at elevated temperature using a long time.

### 2.2.2.2. Ball Milling

Otherwise, the solid-state method without sintering has also applied in the solid-state synthesis of  $\text{Fe}_2\text{GeS}_4$  NCs. For example, Park and his co-workers prepared  $\text{Fe}_2\text{GeS}_4$  NCs by ball milling. As shown in Figure 2.14 (A), a typical synthesis of  $\text{Fe}_2\text{GeS}_4$  NCs by the dry mechanochemical method involves the mixing of elemental precursors, sequential pulverization, chemical reaction and post-annealing process. Moreover, several studies have shown that the post-annealing process can enhance the crystallinity and size of nanocrystals, and protect them from oxidation<sup>[24,25]</sup>. For example, the size of the as-synthesized  $\text{Fe}_2\text{GeS}_4$  NCs is 30-100 nm, and

the size of the post-heat treated  $\text{Fe}_2\text{GeS}_4$  NCs is 60-200 nm, as shown in Figure 2.14 (B). And also, the XRD patterns in Figure 2.15 (A) demonstrates that post-heat treatment can enhance the crystallinity of  $\text{Fe}_2\text{GeS}_4$  NCs. Further, the XPS spectrum in Figure 2.15 (C) manifest that post-heat treatment can protect the as-synthesized  $\text{Fe}_2\text{GeS}_4$  NCs from oxidation. It is worth mentioning that Park et al. firstly provided the Raman scattering of  $\text{Fe}_2\text{GeS}_4$  NCs at around  $361\text{ cm}^{-1}$  in Figure 2.15 (B) which is a valuable character for the future study [25].

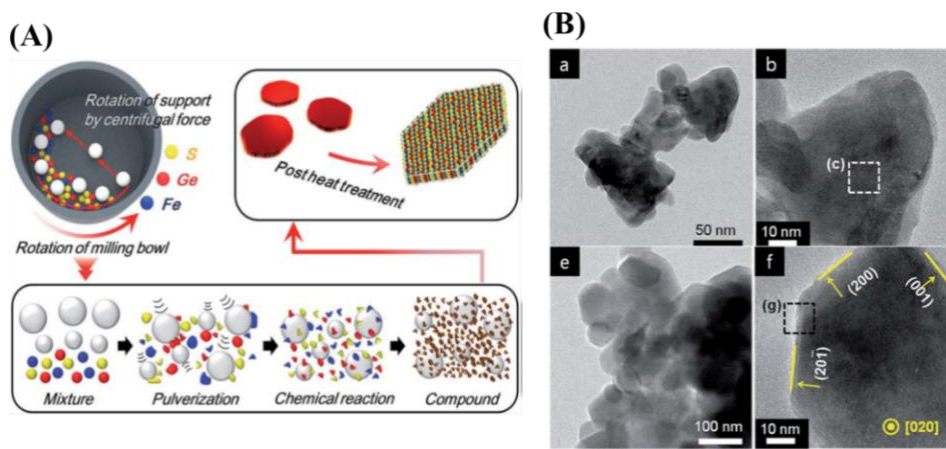


**Figure 2.14.** (A) Schematic illustration of the synthesis of  $\text{Fe}_2\text{GeS}_4$  by mechanochemical process [23]; (B) TEM investigations of as-synthesized (a,b) and heat-treated (e, f)  $\text{Fe}_2\text{GeS}_4$  NCs [23].

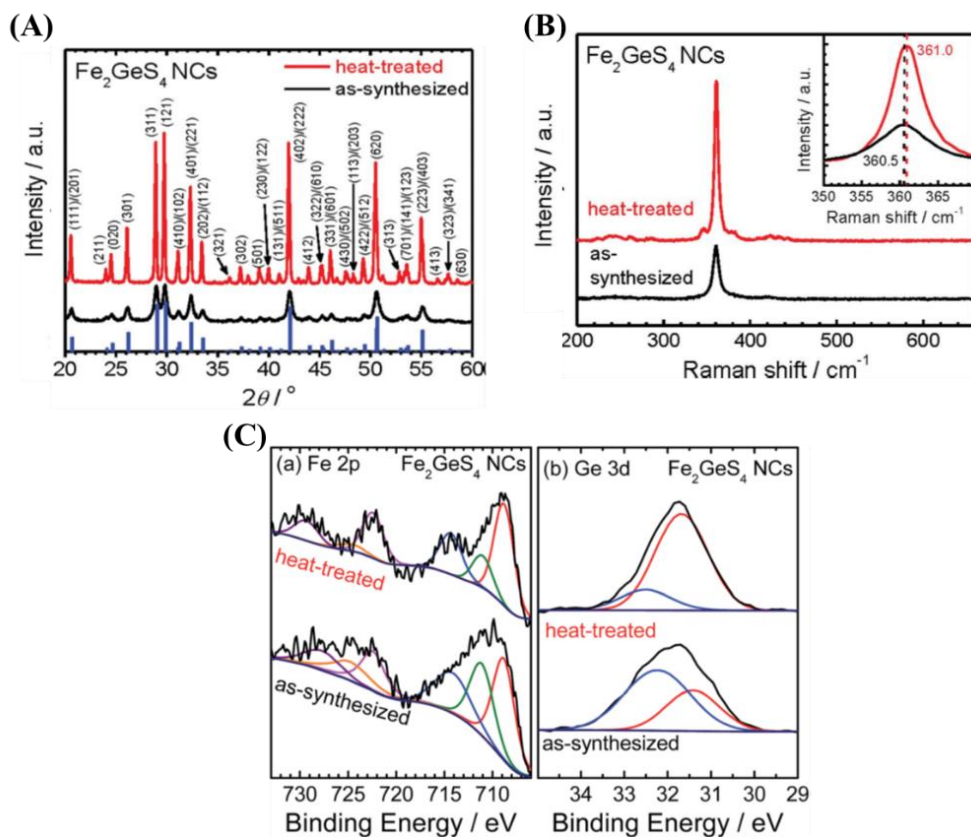


**Figure 2.15.** (A) Comparison of the XRD patterns of the as-synthesized  $\text{Fe}_2\text{GeS}_4$  NCs and those post-annealed at  $450^\circ\text{C}$  for 2 hours <sup>[25]</sup>; (B) Comparison of Raman spectra of the as-synthesized  $\text{Fe}_2\text{GeS}_4$  NCs and those post-annealed at  $450^\circ\text{C}$  for 2 hours <sup>[25]</sup>; (C) High-resolution XPS spectra of (a) Fe 2p and (b) Ge 3d from as-synthesized (bottom) and post-heat-treated (top)  $\text{Fe}_2\text{GeS}_4$  NCs <sup>[24]</sup>.

Although the reaction time of  $\text{Fe}_2\text{GeS}_4$  NCs in this article reduced, it is still an overnight reaction which is not good based on the safety considerations.

### 2.2.2.3. Hand Grinding with Post-Annealing

Alternatively, a typical solid-state synthesis of  $\text{Fe}_2\text{GeS}_4$  NPs which involved the mixing process of the Fe, Ge, S precursors by hand-grinding (10 min, in air) and direct heating process

of the mixed powder under argon and sulfur atmosphere in a tube furnace (600°C, 2h) was reported by Po-Yu Hwang and his co-workers in 2018 <sup>[64]</sup>. The process for preparing Fe<sub>2</sub>GeS<sub>4</sub> NPs is illustrated in Figure 2.16. Unlike other solid-state syntheses of Fe<sub>2</sub>GeS<sub>4</sub> powders, they used Ge[(Gly)<sub>2</sub>(H<sub>2</sub>O)<sub>2</sub>] and FeCl<sub>3</sub> as Ge and Fe source, respectively, to get pure Fe<sub>2</sub>GeS<sub>4</sub> NPs.

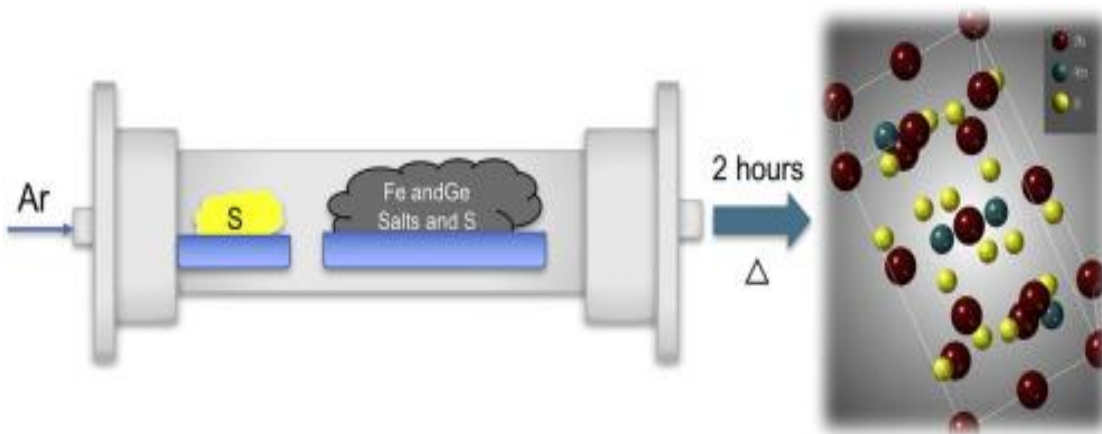


**Figure 2.16.** Illustration of the synthesis of Fe<sub>2</sub>GeS<sub>4</sub> NPs by a rapid molecular precursor solid-state route <sup>[64]</sup>.

More importantly, they proposed the mechanism of Fe<sub>2</sub>GeS<sub>4</sub> NPs formation, as shown in Figure 2.17, which includes the rapid decomposition of pyrite into pyrrhotite phase (Fe<sub>7</sub>S<sub>8</sub>) and the formation of Fe<sub>2</sub>GeS<sub>4</sub> NPs by a reaction of pyrrhotite with GeS<sub>2</sub> or Ge.

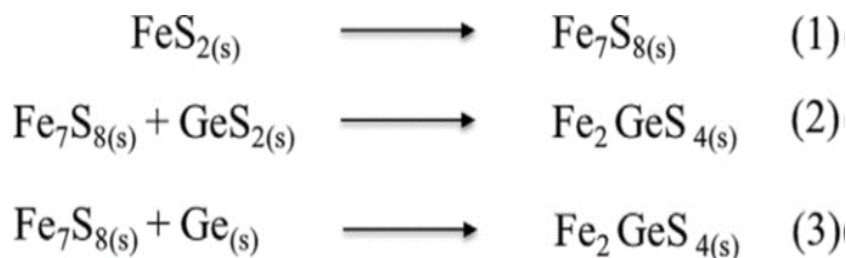


**Figure 2.17.** Proposed mechanism of Fe<sub>2</sub>GeS<sub>4</sub> NPs formation <sup>[64]</sup>.

Currently, although  $\text{Fe}_2\text{GeS}_4$  NCs can be prepared by solid-state synthesis in a short time of 2 hours, the large size, irregular morphology and large aggregates of the synthesized nanocrystals by solid-state methods remain a challenging problem, which impedes its PV applications.

### **2.2.3. Synthesis of $\text{Fe}_2\text{GeS}_4$ Materials via Wet Chemical Method**

Wet chemical synthesis is an alternative to the solid-state methods, which is adapted to prepare the  $\text{Fe}_2\text{GeS}_4$  materials. Generally, the wet chemical method can also refer to as a solution-phase method. A solution-phase method means that the nucleation and growth of nanocrystals are typically carried out in a suitable solvent and surfactant system under certain reaction conditions. The solution-phase method is controllable, relatively facile and cost-efficient, compared to solid-state synthesis. The statement of ‘controllable’ response for controlling the sizes, morphology, compositions of the prepared nanocrystals by adjusting the surfactant, solvent, reaction temperature, and so on. Wet chemical synthesis usually operated in simple reaction vessels that are cheap and easy to handle. The statement of ‘cost efficient’ is due to its short reaction time, low reaction temperature and cheap facilities. In fact, there are many types of wet chemical methods, such as hydrothermal/solvothermal process, hot-injection method, single precursor method, mixed solvents method, and so on [65, 33].

So far, there have been only two articles about the preparation of  $\text{Fe}_2\text{GeS}_4$  materials by the solution-phase method, one via the hot-injection method and the other one via one-pot synthesis.

### 2.2.3.1. Hot-injection Synthesis of Fe<sub>2</sub>GeS<sub>4</sub> NCs

Hot-injection, one of the wet chemical methods, is widely used in the synthesis of nanostructured materials. Briefly, the hot-injection method is a rapid synthetic process in which the cold reagent is injected into the hot precursors to trigger the rapid nucleation which is followed by a crystal growth step. Via hot-injection method, nanostructured materials with uniform morphology and narrow size distribution can be obtained.

In 2013, Fredrick and Prieto reported the first wet chemical synthesis of Fe<sub>2</sub>GeS<sub>4</sub> NCs, in which Fe<sub>2</sub>GeS<sub>4</sub> NCs were obtained by hot-injection method. In their study, FeCl<sub>2</sub>, GeI<sub>4</sub>, hexamethyldisilathiane [(TMS)<sub>2</sub>S] were used as Fe, Ge, S precursors, respectively, and 1-octadecene (ODE), hexadecylamine (HDA) and hexamethyldisilazane (HMDS) were used as solvent or surfactant. Through a 24-hours reaction at 320°C, they obtained plate-like Fe<sub>2</sub>GeS<sub>4</sub> NCs with a size of 75.9±30.9 nm, as shown in Figure 2.18 <sup>[55]</sup>. Comparing with the product obtained by the solid-state method, the Fe<sub>2</sub>GeS<sub>4</sub> NCs synthesized via hot-injection method have a narrow size distribution, which facilitates the photovoltaic performance of Fe<sub>2</sub>GeS<sub>4</sub> based solar device <sup>[55]</sup>.

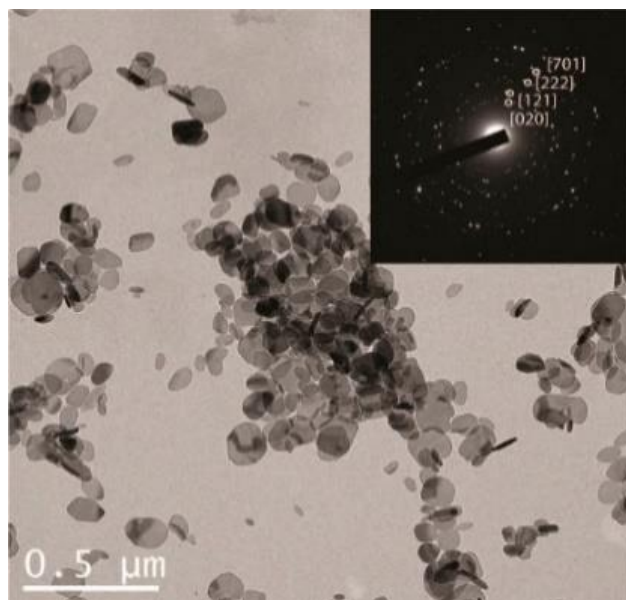


**Figure 2.18.** Low resolution TEM image of  $\text{Fe}_2\text{GeS}_4$  nanocrystals after a 24 h growth time. (Inset) Selected area electron diffraction with four representative spots indexed <sup>[55]</sup>.

### 2.2.3.2. One-pot synthesis of $\text{Fe}_2\text{GeS}_4$ materials

In 2016, Lim and his co-workers prepared  $\text{Fe}_2\text{GeS}_4$  nanosheets by one-pot synthesis. As an advanced process based on the hot injection method, one-pot synthesis is extensively used for the synthesis of nanoparticles due to its simple reaction process. In the report by Lim et al., the reactants  $\text{FeCl}_2$ ,  $\text{GeI}_4$ , 1-dodecanethiol and oleylamine were loaded into only one flask in which the reaction operated at  $320^\circ\text{C}$  for 3.5 hours <sup>[66]</sup>. In such a reaction, no hot-injection and any other manipulate are required. Moreover, the total reaction time is 6.5 hours which is relatively shorter than Fredrick's 24 hours. However, too thick and large size of as-synthesized  $\text{Fe}_2\text{GeS}_4$  nanosheets in Figure 2.19 make it difficult to fabricate a high-quality thin film which is not conducive to its PV application.

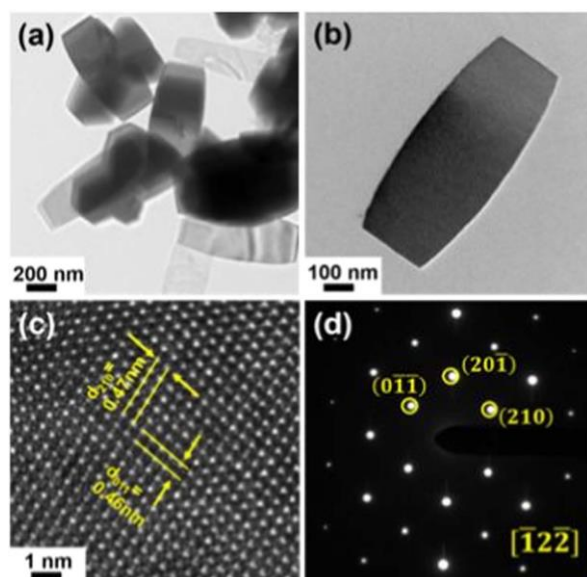


**Figure 2.19.** (a, b) TEM images (c) HRTEM image (d) SAED pattern of as-synthesized  $\text{Fe}_2\text{GeS}_4$  nanosheets [66].

Despite there has been a report containing photoelectrochemistry response for the  $\text{Fe}_2\text{GeS}_4$  thin film [55], however, there has not been a fabricated  $\text{Fe}_2\text{GeS}_4$  based solar cell.

Table 2.3 displays the morphology and size of the  $\text{Fe}_2\text{GeS}_4$  materials prepared under different experimental conditions in the literature. It is known from the table that the  $\text{Fe}_2\text{GeS}_4$  materials prepared by the solution-phase method possess a uniform morphology and a small size, whereas the  $\text{Fe}_2\text{GeS}_4$  materials produced via the solid-state method exhibit an irregular, aggregated morphology. In addition, the reaction temperature for preparing the  $\text{Fe}_2\text{GeS}_4$  materials by the solution-phase method is relatively lower than that of the solid-state method. Thereby, comparing the products prepared by the solid-state method, the hot-injection method, and the one-pot synthesis, it is apparent that the solution-phase method is more controllable, facile, and time cost-effective.

**Table 2.3.** Experimental conditions used in preparation of Fe<sub>2</sub>GeS<sub>4</sub> materials using different method.

Method			Reaction Conditions	Shape of Fe <sub>2</sub> GeS <sub>4</sub> products	Size of products (nm)
Solid-state method	Direct sintering process	Vincent at al. 1976 <sup>[53]</sup>	750°C for 1 week	Large single crystals	–
		Junod at al. 1995 <sup>[57]</sup>	1200 °C for 3 days	Polycrystalline	–
		Yu at al. 2011 <sup>[24]</sup>	900-980 °C for 3 days	Single crystals	–
	Ball milling process	Park at al. 2014 <sup>[25]</sup>	high-energy milling for 12 hours	Irregular NCs	30-100
	Hand-grinding with post-annealing	Hwang at al. 2018 <sup>[64]</sup>	600°C for 2 hours	Irregular NPs	–
Solution-phase method	Hot-injection	Fredrick and Prieto 2013 <sup>[55]</sup>	320°C for 24 hours	plate-like structures NCs	75.9±30.9
	One-pot	Lim at al. 2016 <sup>[66]</sup>	260°C for 2 hours 320°C for 3.5 hours	Sheet-like NCs	800

#### 2.2.4. Fabrication of Fe<sub>2</sub>GeS<sub>4</sub> Thin Films by RF Magnetron Sputtering

Physical vapor deposition (PVD) is a technique widely used for the fabrication of thin films, which generally consists of two steps including vaporization of precursors and deposition process, as shown in Figure 2.20 <sup>[67]</sup>. As the name suggests, the vaporization process is that the target material vaporized into gaseous atoms, molecules, electrons or ions under vacuum conditions. The vapor phases then go back onto the hot substrates and form the target thin film, which is called the deposition process.

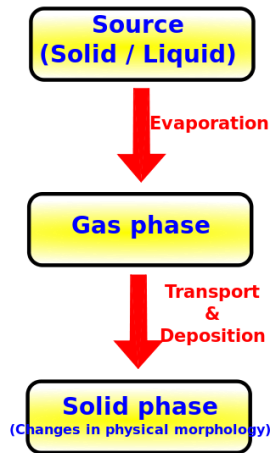


**Figure 2.20.** Process flow diagram of PVD <sup>[67]</sup>.

As one of the most common PVD processes, sputtering deposition has been applied in the fabrication of  $\text{Fe}_2\text{GeS}_4$  thin film. Yu et al. (2011) prepared  $\text{Fe}_2\text{GeS}_4$  thin films by rf magnetron sputtering, and then post-annealed with  $\text{GeS}_2$  at 600-650°C for 1 hour. As well as the powders, the  $\text{Fe}_2\text{GeS}_4$  thin film presents a p-type characteristic and a resistivity of 2.3 k $\Omega$  cm.

According to these investigations, the ternary Fe based chalcogenide  $\text{Fe}_2\text{GeS}_4$  nanomaterials can be prepared by both the solid-state method and the solution-phase method. And the  $\text{Fe}_2\text{GeS}_4$  materials hold significant hope in the photovoltaic applications.

## CHAPTER 3. MATERIALS AND METHOD

### 3.1. Materials

Table 3.1 presents all the chemical reagents and solvents used in this dissertation, which are used as received and without further purification.

**Table 3.1.** Materials used in this research

Materials	Formula	Purity (%)	Supplier
Acetone	C <sub>3</sub> H <sub>6</sub> O	99.8%	VWR International
Ethanol	C <sub>2</sub> H <sub>6</sub> O	99.5%	VWR International
Methanol	CH <sub>4</sub> O	99.8%	VWR International
Milli-Q water	H <sub>2</sub> O	5ppb (TOC)	Millipore USA
Toluene	C <sub>7</sub> H <sub>8</sub>	9.7%	VWR International
Chloroform	CHCl <sub>3</sub>	99.85%	VWR International
Glycolic acid	C <sub>2</sub> H <sub>4</sub> O <sub>3</sub>	99%	Sigma-Aldrich
Diethyl ether	(C <sub>2</sub> H <sub>5</sub> ) <sub>2</sub> O	99%	Sigma-Aldrich
Oleylamine (OLA)	C <sub>18</sub> H <sub>37</sub> N	70%	Sigma-Aldrich
1-Octadecene (ODE)	C <sub>18</sub> H <sub>36</sub>	90%	Alfa Aesar
1-Dodecanethiol (1-DDT)	CH <sub>3</sub> (CH <sub>2</sub> ) <sub>11</sub> SH	98%	Sigma-Aldrich
Germanium (IV) oxide	GeO <sub>2</sub>	99.99%	MSE Supplies
Trioctylphosphine oxide (TOPO)	C <sub>24</sub> H <sub>51</sub> OP	99%	Sigma-Aldrich

Fe (III) 2,4-pentanedionate	$C_{15}H_{21}FeO_6$	97%	Alfa Aesar
Sulfur (99.5%)	S	99.5%	Alfa Aesar
Iron dichloride	$FeCl_2$	98%	Sigma-Aldrich
Germanium tetraiodide	$GeI_4$	99.99%	Sigma-Aldrich
Molybdenum-coated soda lime glass (Mo-SLG)	N.A.	N.A.	The Institute of Energy Conversion, University of Delaware
Glass substrates	N.A.	N.A.	Fisher Scientific
Indium doped Tin-oxide glass (ITO)	N.A.	N.A.	MSE Supplies
Fluorine doped Tin-oxide glass (FTO)	N.A.	N.A.	MSE Supplies
$TiO_2$ paste	$TiO_2$	N.A.	Solaronix
Iodide/tri-iodide electrolyte	$I/I_3^-$	N.A.	Solaronix
Ruthenizer 535-bis TBA	$C_{26}H_{16}O_8N_6S_2Ru$	N.A.	Solaronix

### 3.2. Experimental Outline

As Figure 3.1 shown, the research on  $Fe_2GeS_4$  materials in this dissertation mainly consists of four steps. Step 1 is the synthesis of the  $Fe_2GeS_4$  precursor, including the selection of solvent, precursors and reaction time. Step 2 is the preparation of  $Fe_2GeS_4$  crystals and the fabrication of  $Fe_2GeS_4$  thin films, which contains the optimization of annealing conditions. Step 3 is the characterization of the prepared  $Fe_2GeS_4$  powders and thin films by XRD, Raman, and so on. Step 4 is the fabrication of the  $Fe_2GeS_4$ -based photovoltaic devices, in which the  $Fe_2GeS_4$

thin film works as a counter electrode in the  $\text{Fe}_2\text{GeS}_4$ -catalyzed dye-sensitized solar cells but a light absorbing layer in the  $\text{Fe}_2\text{GeS}_4$  solution-based solar cell.

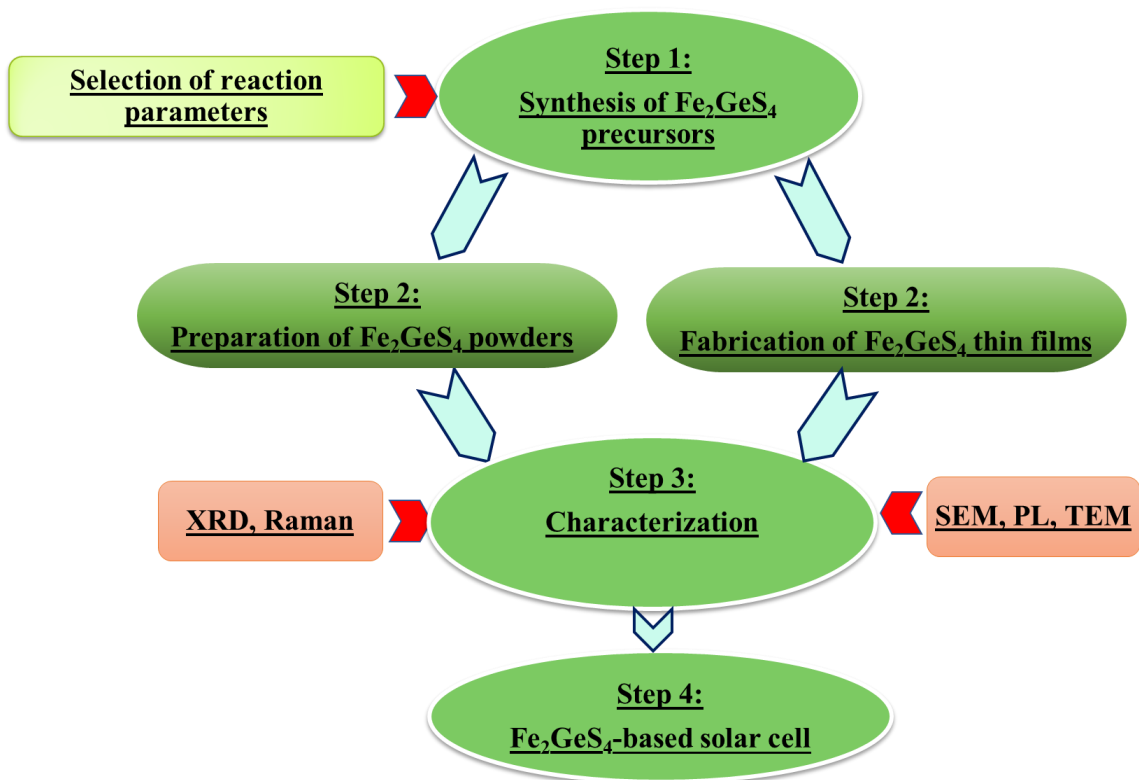


**Figure 3.1.** Outline of research procedures

### 3.2.1. Synthesis of $\text{Fe}_2\text{GeS}_4$ Precursors

Based on the optimum properties of the solution-phase process, in this dissertation, I prepared both the  $\text{Fe}_2\text{GeS}_4$  precursors and the  $\text{Fe}_2\text{GeS}_4$  NCs using the solution-phase method. Basically, a standard Schlenk line is an important apparatus to protect air-sensitive reactants from oxidation during a wet chemical synthesis.

As shown in Figure 3.2, the Schlenk line technique used in this work consists of a vacuum pump, a Schlenk line, an oil bubbler, and an inert gas tank. The schlenk line is made up of a vacuum line and an inert gas line, in which the vacuum line is used to remove impurities with low boiling point whereas the inert gas line is used to protect the air-sensitive compounds from oxidation<sup>[68]</sup>.

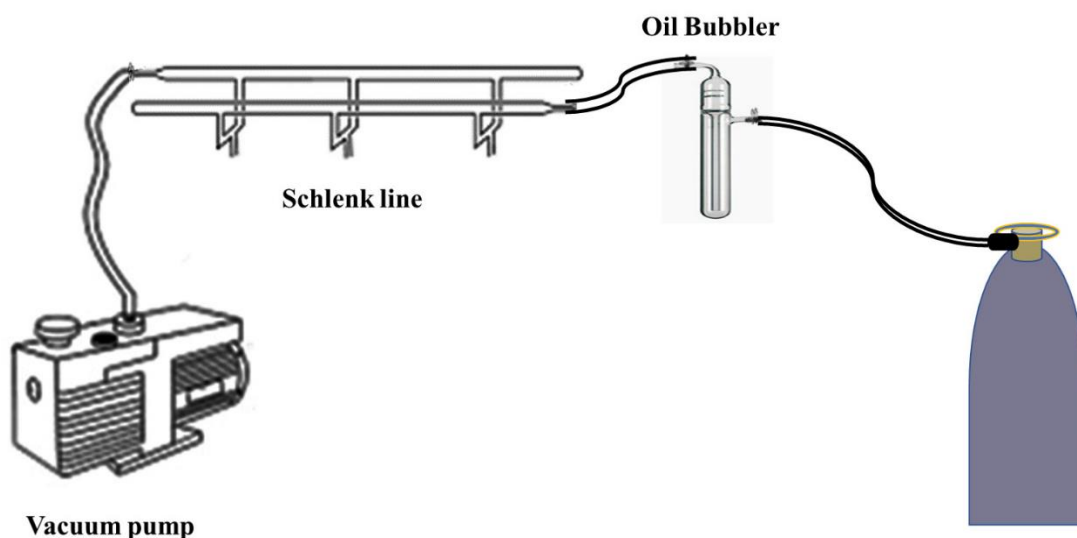


**Figure 3.2.** Schlenk line set-up.

In the synthesis of FGS precursors, several reaction parameters were studied in this work, such as different solvents, different Fe and Ge precursors, and different reaction times.

### **3.2.1.1. Option of Solvent**

As aforementioned, the main feature of solution-phase synthesis is that the reaction takes place in a suitable solvent. In general, solvents in the wet chemical process can be used not only

as solvents but also as surfactants or coordinating ligands at sometimes. Therefore, the selection of solvent is a critical step in the synthesis of materials. To prepare the  $\text{Fe}_2\text{GeS}_4$  precursors, in this research I tried to use oleylamine or a mixture of oleylamine & 1-octadecene as a solvent. By comparing their effects on the as-synthesized  $\text{Fe}_2\text{GeS}_4$  precursors, the most suitable solvent was selected.

### **3.2.1.2. Option of Precursors**

As well as the solvent, the right selection of precursors is also a key factor in achieving the target nanomaterial. For example, the report by Prieto and Fredrick presents that the  $\text{Fe}_2\text{GeS}_4$  NCs can be obtained by using the  $(\text{TMS})_2\text{S}$  as the sulfur precursor<sup>[55]</sup>. But if the elemental sulfur powder is selected as the sulfur source, the only product obtained is the iron sulfide<sup>[55]</sup>. In another report by Lim et al., 1-dodecanethiol is the only correct sulfur precursor<sup>[66]</sup>. In my work, I compared the effects of different Fe precursors and Ge precursors on the as-synthesized  $\text{Fe}_2\text{GeS}_4$  precursors.

### **3.2.1.3. Option of Reaction Time**

Reaction time has a significant impact on the nanomaterial's synthesis. If the reaction time is not enough, the reaction will be incomplete, resulting in an impure product. However, the overlong reaction time may result in increased product size and other impurities. As a typical example, the report by Park et al. presents that the reaction of 10 hours produces a mixture of

FeS and Fe<sub>2</sub>GeS<sub>4</sub>, whereas the 12-hours reaction could produce pure Fe<sub>2</sub>GeS<sub>4</sub> NCs [25]. Thus, it is essential to select an optimal reaction time.

### **3.2.2. Fabrication of Fe<sub>2</sub>GeS<sub>4</sub> Thin Films**

Typically, the fabrication of thin films involves depositing a material onto a suitable substrate. In the literature, a post-annealing process can help grow grains that are beneficial for photovoltaic applications. During my doctoral work, I tested the photovoltaic performance of the Fe<sub>2</sub>GeS<sub>4</sub> thin films deposited on Fluorine doped Tin-oxide glass (FTO) and Molybdenum-coated soda lime glass (Mo-SLG). In addition, I tried three different chemical deposition methods, such as spin coating, dip-coating, and bar coating. Finally, I choose dip-coating as the deposition method depending on the Fe<sub>2</sub>GeS<sub>4</sub> precursors and the substrate structure. In order to achieve high-quality Fe<sub>2</sub>GeS<sub>4</sub> thin films, I optimized the annealing conditions, such as the annealing temperature and time.

### **3.2.3. Fabrication of Fe<sub>2</sub>GeS<sub>4</sub> Based Photovoltaic Devices**

Currently, there are many types of thin-film-based solar cells, such as dye-sensitized solar cells (DSSC), perovskite solar cells, quantum dot solar cells, and so on. In this dissertation, we propose the sandwich-structured Fe<sub>2</sub>GeS<sub>4</sub>-catalyzed dye-sensitized solar cell, Fe<sub>2</sub>GeS<sub>4</sub>-solution-based solar cell, and a dye-sensitized solar cell without Fe<sub>2</sub>GeS<sub>4</sub>. The details of the experiments were described in chapters 4 and 5.

### **3.2.4. Characterization Technique**

In this dissertation, I used X-ray diffraction (XRD), Raman spectroscopy, X-ray fluorescence (XRF), transmission electronic microscopy (TEM), and thermogravimetric analysis (TGA) to characterize the Fe<sub>2</sub>GeS<sub>4</sub> powders. And Fe<sub>2</sub>GeS<sub>4</sub> thin films are analyzed by X-ray diffraction (XRD), Raman spectroscopy, scanning electron microscopy (SEM). The band gap of the Fe<sub>2</sub>GeS<sub>4</sub> thin film was measured using room-temperature photoluminescence (PL) spectra.

#### **3.2.4.1. X-ray Diffraction (XRD)**

In this dissertation, the crystal structure of Fe<sub>2</sub>GeS<sub>4</sub> materials was determined by the X-ray diffraction (XRD) instrument (Rigaku MiniFlex600) which equipped with a Cu K $\alpha$  radiation ( $\lambda = 1.5418 \text{ \AA}$ ). The measurement is conducted from 10 to 70 degrees under the condition of 30 mV and 10 mA. And the scanning speed is 1°/min. The powder samples were mounted on a sample holder as shown in Figure 3.3 (a), whereas the thin films are stick to a fitting glass substrate as shown in Figure 3.3 (b).

#### **3.2.4.2. Raman Spectroscopy**

According to the principles of the Raman spectroscopy, I characterized the Fe<sub>2</sub>GeS<sub>4</sub> powders and thin films using the Horiba Scientific XploRA PLUS Raman spectroscopy. The spectrometer is equipped with a 532 nm Ar-laser source. The powder sample was placed on the same sample holder as in Figure 3.3 (a), whereas the film sample was placed on a glass slide as

shown in Figure 3.3(c). The Raman spectroscopy analysis of  $\text{Fe}_2\text{GeS}_4$  powders and thin films were measured from  $250\text{ cm}^{-1}$  to  $450\text{ cm}^{-1}$ .

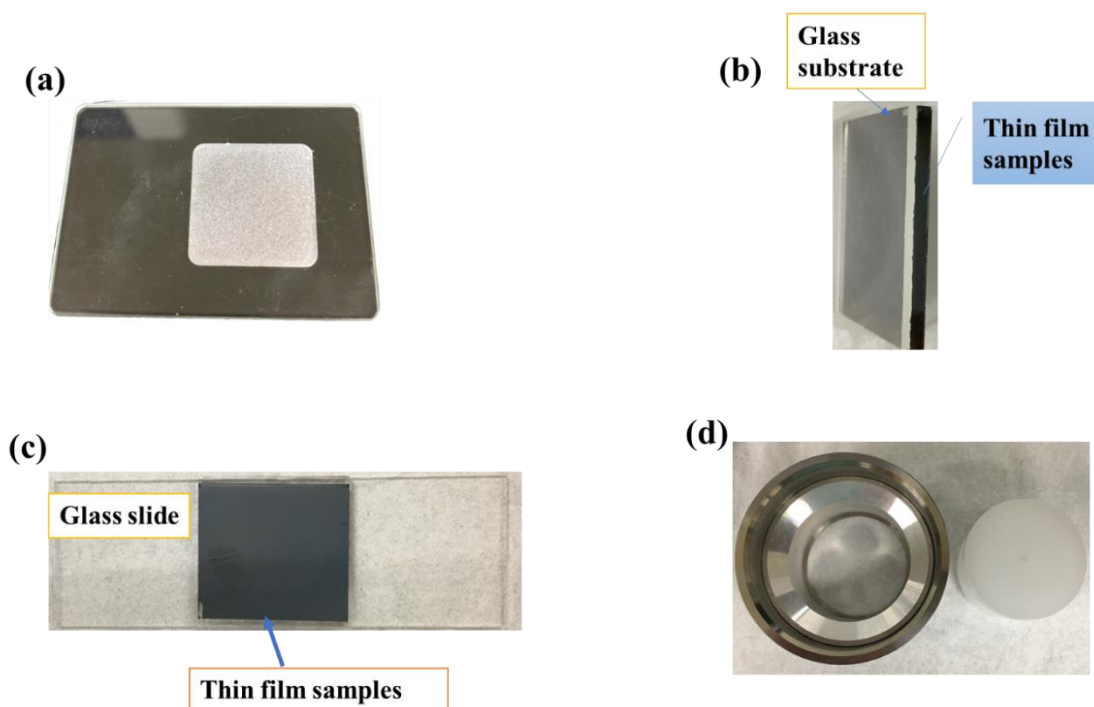


**Figure 3.3.** Illustration of sample set-up. (a) XRD powder sample holder; (b) Set-up for XRD thin film sample; (c) Set-up for Raman thin film sample; (d) XRF sample holder.

### 3.2.4.3. X-ray Fluorescence (XRF)

In general, X-ray fluorescence (XRF) spectrometer is used to determine the elements in materials. Depending on its principle, in my research, I used X-ray fluorescence (XRF) to investigate the composition of the obtained  $\text{Fe}_2\text{GeS}_4$  powders. The sample holder for the XRF measurement is as shown in Figure 3.3(d).

#### **3.2.4.4. Transmission Electron Microscopy (TEM) and Scanning Electron Microscopy (SEM)**

The JEM-2100F Transmission Electron Microscope (TEM) is used to display the morphology and size of  $\text{Fe}_2\text{GeS}_4$  powders in this dissertation.

The SEM images in my doctoral work were collected from a scanning electron microscopy (Hitachi S4700), which exhibited the information about the surface of  $\text{Fe}_2\text{GeS}_4$  thin films.

#### **3.2.4.5. Photoluminescence Spectroscopy (PL)**

Photoluminescence spectroscopy is a technique that provides the optical and electrical properties of materials, such as measuring the band gap of semiconductors. In my dissertation, the Room-temperature photoluminescence (PL) spectroscopy was applied for measuring the band gap of  $\text{Fe}_2\text{GeS}_4$  thin film, which was operated under continuous monochromatic illumination of an argon ion laser (514.5 nm). The photoluminescence (PL) spectra were collected by two off-axis mirrors, spectrally resolved by a grating monochromator and detected by a Si-CCD array <sup>[69]</sup>.

#### **3.2.4.6. Thermogravimetric Analysis (TGA)**

Briefly, the principle of thermogravimetric analysis (TGA) is to monitor the mass loss of a sample as the temperature increases. The thermogravimetric analysis (TGA) applied in this dissertation is used to measure the mass loss of  $\text{Fe}_2\text{GeS}_4$  nanoparticles at a heating rate of 5 °C/min in the range of 25-800 °C under argon atmosphere.

### 3.2.5. Photocurrent-Voltage Measurements

The photovoltaic performance of the  $\text{Fe}_2\text{GeS}_4$  based solar cells was determined by a combined system which consists of a Keithley 2400 source meter, a small Area Solar Simulator, and a reference cell meter.

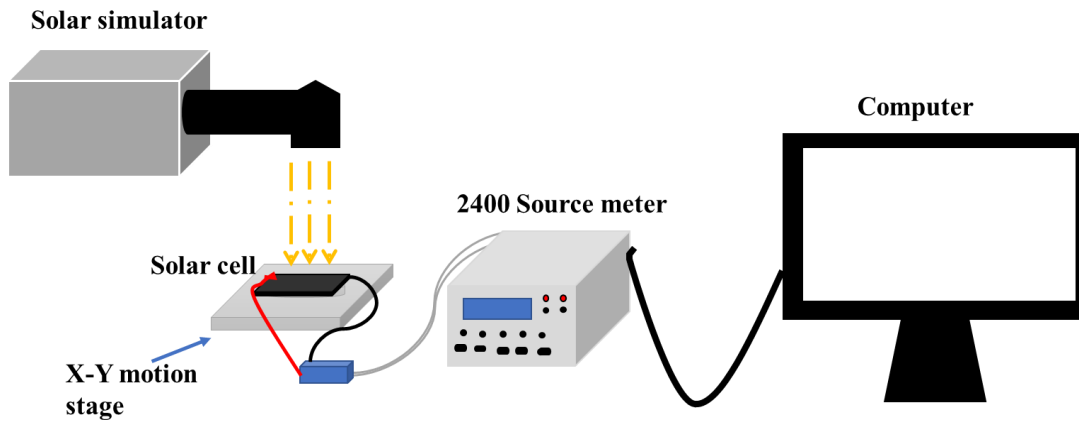


**Figure 3.4.** Schematic diagram of J-V measurement setup.

The photocurrent-voltage (J-V) measurements of the  $\text{Fe}_2\text{GeS}_4$  based solar cell devices were carried out by a combined system which presents in Figure 3.4<sup>[70-73]</sup>. In detail, a Small Area Solar Simulator (LCS-100TM) with an AM1.5G solar spectrum is used to produce light. And an optical power meter (New port) is used to adjust the light intensity of the solar simulator to  $100 \text{ mW cm}^{-2}$ . An x-y motion stage is used to adjust the position of samples to absorb the incident light effectively. Then, a source meter (Keithley 2400) connected to a computer is used to record the collected data. Finally, the PVIV software is used to analyze the photocurrent density-voltage (J-V) characteristics, which provides the information of short-circuit current density ( $J_{\text{SC}}$ ), open-

circuit voltage ( $V_{OC}$ ), fill factor (FF), conversion efficiency ( $\eta$ ), and so on. The whole current-voltage measurements were done at room temperature.

## CHAPTER 4. SOLUTION-PROCESSED $\text{Fe}_2\text{GeS}_4$ THIN FILMS AND SOLAR CELLS

### 4.1. Introduction

With the development of the solar cells, finding suitable semiconductor materials has become an urgent problem to be solved. So far, a large number of materials have been investigated as candidates for photovoltaic application, such as silicon, CZTS, CdTe, and so on. Among these candidates, the  $\text{Fe}_2\text{GeS}_4$  material has recently attracted more and more attention because it has a high absorption coefficient of  $10^5 \text{ cm}^{-1}$ , a suitable band gap of 1.4 eV and a better sustainability<sup>[24]</sup>. Up to now, several approaches have been applied in the preparation of  $\text{Fe}_2\text{GeS}_4$  materials, such as melting<sup>[53,56,57,24]</sup>, ball milling method<sup>[25]</sup>, hand grinding with post annealing<sup>[64]</sup>, hot-injection<sup>[55]</sup>, and one-pot synthesis<sup>[66]</sup>. However, most syntheses of  $\text{Fe}_2\text{GeS}_4$  materials require high reaction temperatures and long reaction times. Moreover, to the best of our knowledge, there have been no reports on the  $\text{Fe}_2\text{GeS}_4$  based photovoltaic devices yet.

In this chapter, a facile and time-efficient solution-phase method for the preparation of  $\text{Fe}_2\text{GeS}_4$  (FGS) precursors has been developed. The FGS precursor was deposited on a substrate and then subjected to thermal treatment to fabricate a high-quality thin film. The resulting FGS thin film was incorporated into a photovoltaic device to study its photovoltaic performance.

### 4.2. Experimental Section

#### 4.2.1. Synthesis of FGS Precursors

##### 4.2.1.1. Synthesis of Ge Precursor [Diaquabis (glycolato-O, O'') Germanium (IV)— $\text{Ge}(\text{Gly})_2(\text{H}_2\text{O})_2$ ].

The  $\text{Ge}(\text{Gly})_2(\text{H}_2\text{O})_2$  powder used in my dissertation was prepared via a published procedure by Chiang et al <sup>[74]</sup>. First, glycolic acid powder (1.52 g, 20.0 mmol) was dissolved in 100 mL of Milli-Q water to prepare a glycolic acid aqueous solution. Under magnetic stirring, 0.52 g (5.0 mmol) germanium dioxide ( $\text{GeO}_2$ ) was loaded into this 250 mL one-neck round bottom flask containing 100 mL pre-prepared aqueous solution of glycolic acid. The reaction flask was then connected to a condenser and further refluxed for 4 hours. After cooling to room temperature, the resulting solution was reduced to about 5 mL by rotary evaporation. The  $\text{Ge}(\text{Gly})_2(\text{H}_2\text{O})_2$  precipitate was obtained by adding a mixture of diethyl ether and ethanol (V: V, 1:1). Finally, the  $\text{Ge}(\text{Gly})_2(\text{H}_2\text{O})_2$  powder was collected by filtration and stored in a vacuum oven.

#### 4.2.1.2. Synthesis of FGS Precursors

The FGS precursor in this work was synthesized via a solution-phase approach which was briefly shown in Figure 4.1. In addition, the effects of solvent, Fe precursor, Ge precursor and reaction time on the product were also studied in the doctoral dissertation.

As shown in Figure 4.1, 0.957g (3.73 mmol)  $\text{Ge}(\text{Gly})_2(\text{H}_2\text{O})_2$  powder was loaded to a 100-mL two-neck round-bottom quartz flask containing a degassed mixture of 10 mL OLA and 5 mL ODE. 2.119 g (6 mmol) Fe (III) 2,4-pentanedionate and 0.384 g (12 mmol) Sulfur powder were separately added to two 25 mL two-neck round bottom glass flask, each of them containing a mixed degassed solution of 10 mL OLA and 5 mL ODE. To remove moisture, all of these three solutions firstly were stirred at 120 °C under vacuum for 30 minutes. Next, argon gas was back-filled to the system that prevents the reactants from oxidization. Then the Fe (III) precursor was

injected into the colorless Ge(IV) solution at 120°C and the mixture turned brownish black within 1 minute. The temperature of the reaction mixture was maintained at 120°C for 10 minutes, followed by heating to 250°C. At the same time, the temperature of the sulfur solution was raised to 150°C and held until the next injection. Once both two solutions reached the target temperatures, the sulfur solution was added dropwise to the Fe–Ge solution. The final solution was held at 250 °C for 15 minutes, after which the reaction was cooled to room temperature by removing the heating source. Afterward, the obtained product was washed with a mixed solution of chloroform and ethanol (V: V, 1:2). The resulting product was dried under vacuum <sup>[69]</sup>.

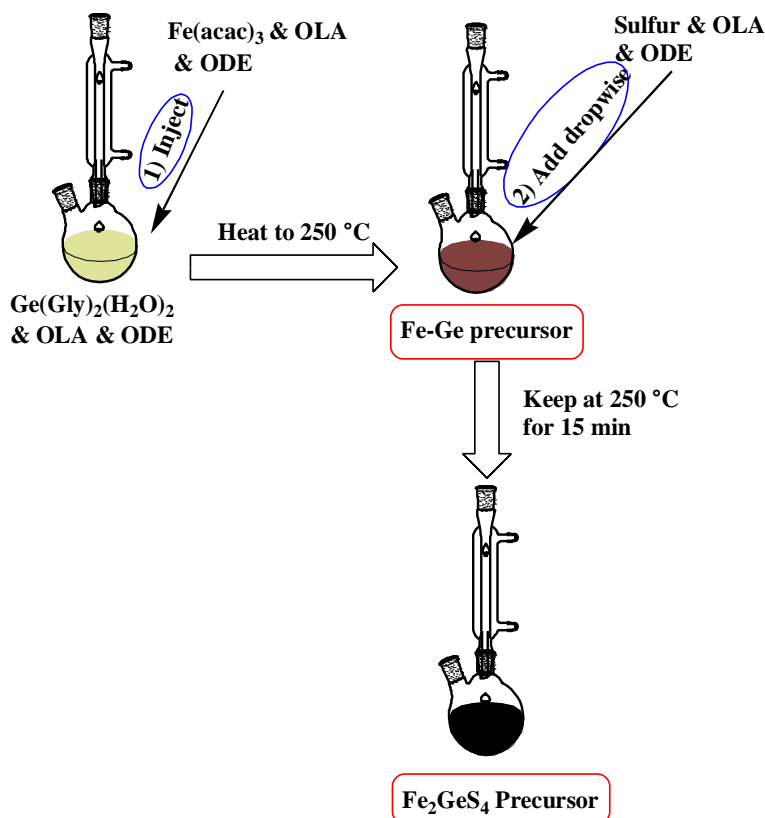


**Figure 4.1.** Illustration of synthesis procedure.

### 4.2.1.3. Selection Experiments of Reaction Parameters for the Synthesis of FGS Precursors

Prior to getting the process of synthesizing the FGS precursor described above, several reaction parameters were studied in this work, such as different solvents, different Fe and Ge precursors, and different reaction times. The details were displayed in Table 4.1.

**Table 4.1.** Selection of reaction parameters

Material	Solvent	Fe precursor	Ge precursor	Reaction time
Fe <sub>2</sub> GeS <sub>4</sub> precursors	Oleylamine (70%)	FeCl <sub>2</sub>	Ge(Gly) <sub>2</sub> (H <sub>2</sub> O) <sub>2</sub>	15 min
		Fe (III) 2,4-pentanedionate	Ge(Gly) <sub>2</sub> (H <sub>2</sub> O) <sub>2</sub>	15 min
		Fe (III) 2,4-pentanedionate	GeI <sub>4</sub>	15 min
		Fe (III) 2,4-pentanedionate	Ge(Gly) <sub>2</sub> (H <sub>2</sub> O) <sub>2</sub>	2 h
	Oleylamine (70%) & 1- Octadecene (90%)	Fe (III) 2,4-pentanedionate	Ge(Gly) <sub>2</sub> (H <sub>2</sub> O) <sub>2</sub>	15 min

#### 4.2.1.3.1. Option of Precursors.

In the selection experiment of Ge precursor, I replaced the Ge(Gly)<sub>2</sub>(H<sub>2</sub>O)<sub>2</sub> with GeI<sub>4</sub> when using oleylamine as the solvent. For the choice of Fe precursor, FeCl<sub>2</sub> was used as the Fe source instead of Fe (III) 2,4-pentanedionate.

#### *4.2.1.3.2. Selection of Reaction Time*

To evaluate the effect of reaction time on the target FGS precursors, the products were collected at different reaction times and then compared the reaction products using 15 minutes and that using 2 hours. The synthetic procedure was the same as above.

#### *4.2.1.3.3 Option of Solvent*

In general, the solvent can serve various functions in solution-processed syntheses, such as surfactants, ligand coordination, reductive agents, and so on. In the literature, the physical and chemical properties of the obtained product may vary depending on the solvent used. To achieve high-quality target FGS precursors, I tried to use oleylamine or a mixture of oleylamine & 1-octadecene (V: V, 1:2) as the solvent. Further, this procedure is the same as the above method of synthesizing the FGS precursor except for the solvent.

### **4.2.2. Preparation of FGS Powders**

In view of the amorphous nature of the as-synthesized FGS precursor, a post thermal treatment on the FGS precursors should be carried out to prepare the FGS crystals. In order to get pure high-crystallinity FGS powders, a study has been conducted on the thermal treatment of the as-synthesized FGS precursor powders. Five FGS precursor samples were respectively annealed at 400°C, 450°C, 500°C, 550°C, and 600°C in a tube furnace for 2 hours under sulfur and argon atmosphere. Figure 4.2 presents the process of the thermal treatment for FGS precursor powders. The sulfur powder (0.5 g) placed before FGS precursor powders served as the source of the

sulfur atmosphere. When the temperature reached 445 °C, the sulfur powder began to evaporate and formed gaseous sulfur slowly. As the argon gas flows, the entire tube was filled with gaseous sulfur to form the argon and sulfur atmosphere.



**Figure 4.2.** Illustration of thermal treatment <sup>[64]</sup>.

### 4.2.3. Fabrication of FGS Thin Films

As shown in Figure 4.3, a typical fabrication of FGS thin films consists of the preparation of FGS precursor inks, a deposition process, and post thermal treatment.

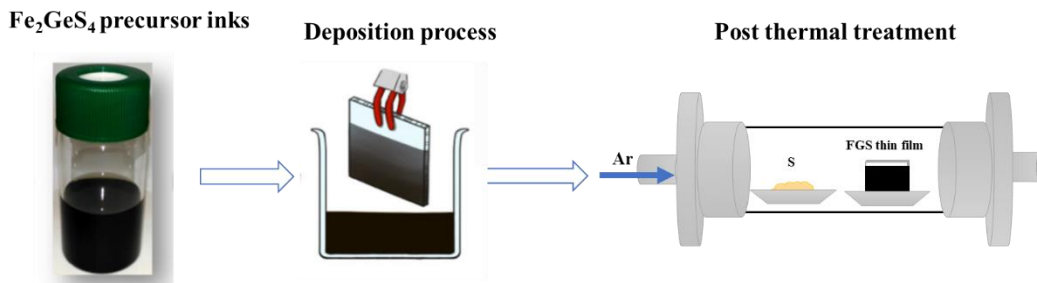


**Figure 4.3.** Fabrication of FGS thin films <sup>[69]</sup>.

#### **4.2.3.1. Preparation of FGS Precursor Inks.**

The FGS precursor inks were prepared by dispersing the as-synthesized FGS precursor powders (300 mg) into a 13.5 mL mixed solution of ethanol and toluene (V: V, 1:8), followed by an ultrasonic treatment using an ultrasonic probe for 6 minutes. The resulting black inks were immediately deposited on substrates without further storage.

#### **4.2.3.2. Deposition Process**

In this work, soda-lime glass, Molybdenum-coated soda lime glass (Mo), Indium doped Tin-oxide glass (ITO), and Fluorine doped Tin-oxide glass (FTO) substrates were used for thin film fabrication. To obtain a clean surface of substrates, the substrates were sequentially rinsed in an ultrasonic bath of methanol, Milli-Q water, and acetone. After drying the substrates, transfer them to a plasma cleaner for further cleaning<sup>[69]</sup>.

The FGS precursor ink was coated on the substrate by dip-coating. The details of the dip-coating process present as follows. First, the substrate was slowly dipped into the fresh FGS precursor inks manually; next, the substrate was held in the inks for around 3 seconds; then, the substrate was slowly taken out; Finally, the as-deposited thin film was air-dried. This dip-coating process was repeated nine times to get the desired thickness.

#### **4.2.3.3. Thermal Treatment**

Once the coating completed, the thin film was placed in a tube furnace under sulfur and argon atmosphere for thermal treatment. As with the thermal treatment of the FGS powders, the

sulfur powder placed before the FGS thin film was the source of the sulfur atmosphere. In order to obtain a high-quality FGS thin film, the optimization of annealing conditions for FGS thin films has been carried out. Five FGS thin films were annealed respectively in the tube furnace at different temperatures ranging from 400°C to 600°C for 2 hours. In addition to the annealing temperature, the effect of annealing time of 1-3 hours on the purity of the FGS thin films has also been investigated.

#### **4.2.4. Solar Cells Fabrication**

In FGS-catalyzed dye-sensitized solar cells, a dye-sensitized TiO<sub>2</sub> thin film worked as the photoelectrode for providing photoelectrons, whereas the FGS thin film acted as a counter electrode which used for charge transport. However, in FGS solution-based solar cell, the FGS is used as a light absorbing layer that provides photoelectrons.

##### **4.2.4.1. Preparation of Photoelectrodes**

As described above, the photoelectrode in the FGS-catalyzed dye-sensitized solar cell was the dye-sensitized TiO<sub>2</sub> thin film. Following the procedure from Grätzel's group<sup>[75]</sup>, the dye-sensitized TiO<sub>2</sub> thin film was prepared by holding the pre-prepared TiO<sub>2</sub> thin film in a dye methanolic solution of ruthenizer 535-bis TBA (0.3 mmol/L) overnight. The TiO<sub>2</sub> thin films were prepared by bar-coating the TiO<sub>2</sub> paste on an Indium-doped tin oxide substrates (ITO) and baking it on a hot plate at 300 °C for 5 min.

#### **4.2.4.2. Preparation of Counter Electrode**

In the FGS-catalyzed dye-sensitized solar cell, the annealed FGS thin film was assembled as the counter electrode to evaluate its potential for photovoltaic application. In a dye-sensitized solar cell (DSSC) without FGS, a clean Molybdenum-coated soda lime glass (Mo) was used as the counter electrode.

#### **4.2.4.3. Fabrication of FGS Based Solar Cells**

##### *4.2.4.3.1. Assembly of Dye-Sensitized Solar Cell (DSSC) without FGS*

Firstly, the dye-sensitized solar cell (DSSC) without FGS was fabricated through assembling a pure Mo substrate face-on to a dye-sensitized TiO<sub>2</sub> thin film like a sandwich-structure, following the procedure reported by Xin et al.<sup>[76]</sup>. To ensure that these two thin films were tightly attached, we held them with a binder clip. Then, two drops of electrolyte consisting of iodide/tri-iodide-iodide were added to the spacer between the two electrodes<sup>[69]</sup>. The architecture of this assembled solar cell, with a structure of ITO/TiO<sub>2</sub>&Dye/Electrolyte /Mo, was shown in Figure 4.4.

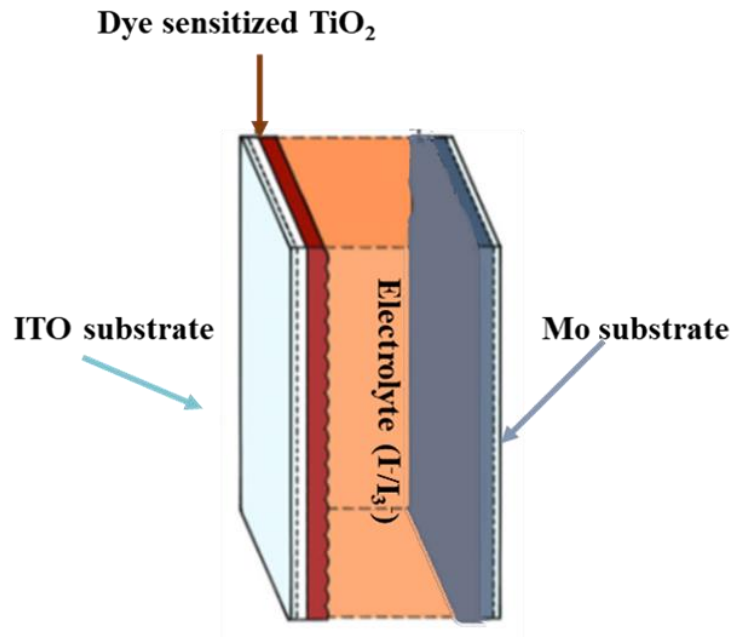


**Figure 4.4.** Dye-sensitized solar cell without FGS (ITO/TiO<sub>2</sub>&Dye/Iodine solution/Mo) <sup>[69]</sup>.

#### 4.2.4.3.2. Assembly of FGS-catalyzed Dye-sensitized Solar Cell

Using the same route to the above assembling, a thin layer of FGS was fabricated into the counter electrode and then assembled with a dye-sensitized TiO<sub>2</sub> thin film to construct the FGS-catalyzed dye-sensitized solar cell with an architecture of ITO/TiO<sub>2</sub>&Dye/Iodine solution/Mo, as shown in Figure 4.5 (a). Base on the FTO was the commonly used substrate for the counter electrode in DSSC <sup>[76,77]</sup>, an FGS-catalyzed DSSC using FGS coated on FTO substrate as the counter electrode was also fabricated following the same approach to the above constructs, which possessing a structure of ITO/TiO<sub>2</sub>&Dye/Electrolyte/FGS/FTO, as shown in Figure 4.5 (b). Their photocurrent voltage (J-V) measurements were performed under the same conditions to the DSSC without FGS.

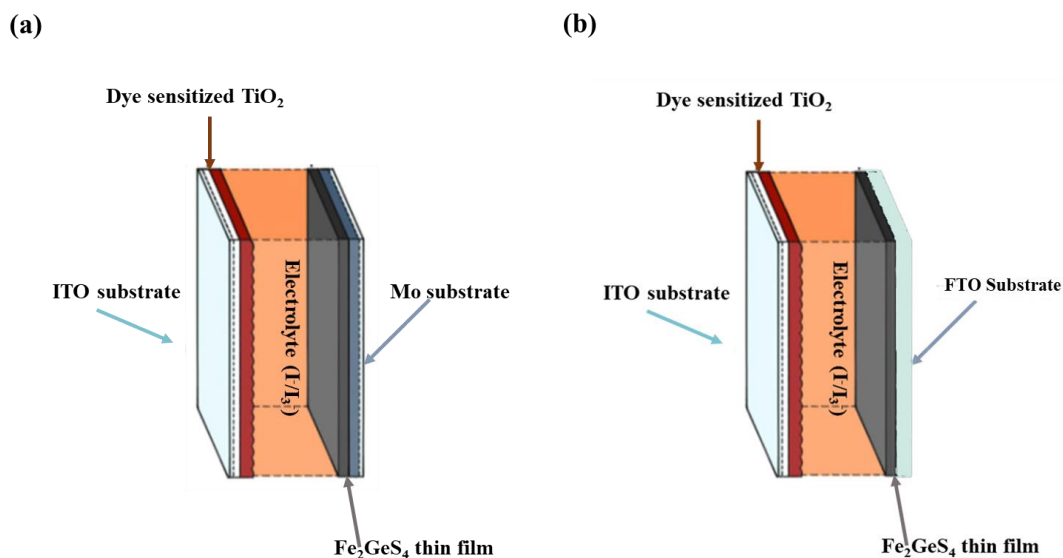


**Figure 4.5.** Structure of FGS-catalyzed DSSC<sup>[69]</sup>. (a) ITO/TiO<sub>2</sub>&Dye/Iodine solution/FGS/ Mo. (b) ITO/TiO<sub>2</sub>&Dye/Iodine solution/FGS/FTO.

#### 4.2.4.3.3. Assembly of FGS Solution-based Solar Cell

As aforementioned, FGS material exhibited great optoelectrical properties which highlighted its potential for photovoltaic application. In order to single out the photoactive effects of the FGS from the photo-activity of the dye, an FGS solution-based solar cell was fabricated.

The FGS-solution-based solar cell was fabricated following the same procedure to the above assembling but without adding the dye to the TiO<sub>2</sub> films. The construction was as shown in Figure 4.6, which possessed a structure of ITO/TiO<sub>2</sub>/iodine solution/FGS/Mo. In such a photovoltaic device, the FGS thin film worked as a light absorbing layer. The photovoltaic performance parameters were measured under the same condition as the photovoltaic devices

described above. The comparison between the FGS solution-based solar cell with the FGS-catalyzed DSSC could be used to evaluate the optoelectrical activity of FGS.

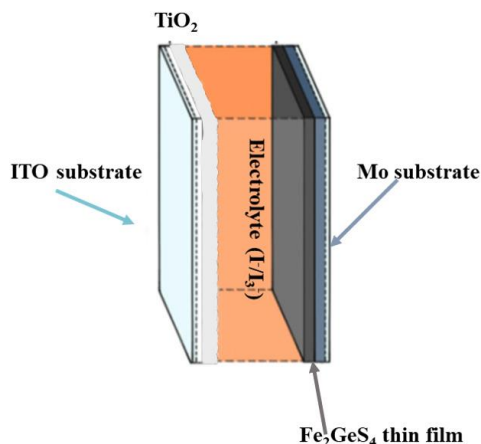


**Figure 4.6.** FGS solution-based solar cell (ITO/TiO<sub>2</sub>/Iodine solution/FGS/Mo) [69].

### 4.3. Result and Discussion

#### 4.3.1. Results of Synthesized FGS Precursors

##### 4.3.1.1. Results of Selection Experiments

###### 4.3.1.1.1. Selection of Fe and Ge Precursors.

In all the selection experiments of Fe and Ge precursors, oleylamine was used as the only solvent. For the selection of Fe precursors, two reagents of Fe(acac)<sub>3</sub> and FeCl<sub>2</sub> were mainly studied when other conditions were held constant. By comparing the XRD patterns of the annealed FGS powder in Figure 4.7, it is clear that the peaks of the annealed FGS using Fe(acac)<sub>3</sub> is more comprehensive and sharper than that of FeCl<sub>2</sub>, indicating the crystallinity of FGS powder prepared using Fe(acac)<sub>3</sub> is higher than that using FeCl<sub>2</sub> under the same conditions

[78]. Therefore,  $\text{Fe}(\text{acac})_3$  is a better Fe source for the FGS preparation. In contrast to  $\text{FeCl}_2$ , the  $\text{Fe}(\text{acac})_3$  is soluble in organic solvent due to its organic ligand of acetylacetonate [79]. In this solution system, the carbonyl groups ( $\text{C}=\text{O}$ ) of acetylacetonate can react with the amine ( $-\text{NH}_2$ ) group of oleylamine to form a new Fe-complex, which leads to easier releasing of Fe ions [80]. Thus, Speculating the reason for the better behavior of  $\text{Fe}(\text{acac})_3$ , we could say that the acetylacetonate ligands of  $\text{Fe}(\text{acac})_3$  enhanced the nucleation rate [81]. Furthermore, oleylamine has a double bond and amine group. Both of these groups ( taking double bond as a ‘group’) may act as reductants which reduce  $\text{Fe}^{3+}$  to  $\text{Fe}^{2+}$  at elevated reaction temperature [82, 83].

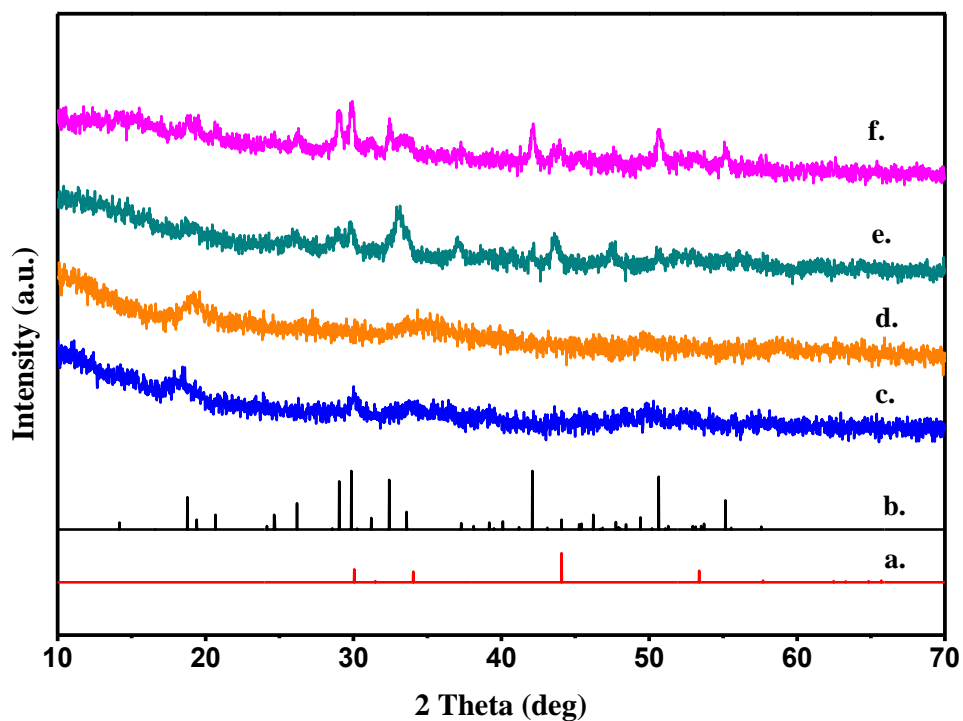


**Figure 4.7.** XRD patterns of FGS powders prepared from different Fe precursors. (a) Standard XRD pattern of  $\text{Fe}_7\text{S}_8$ ; (b) Standard XRD pattern of FGS; (c) XRD patterns of the as-synthesized FGS using  $\text{FeCl}_2$ ; (d) XRD patterns of as-synthesized FGS using  $\text{Fe}(\text{acac})_3$ ; (e) XRD pattern of the annealed FGS synthesized using  $\text{FeCl}_2$ ; (f) XRD pattern of the annealed FGS synthesized using  $\text{Fe}(\text{acac})_3$ .

Under the same conditions, using  $\text{Fe}(\text{acac})_3$  and sulfur powder as Fe and sulfur sources, the Ge source was changed from the pre-prepared  $\text{Ge}(\text{Gly})_2(\text{H}_2\text{O})_2$  to the purchased  $\text{GeI}_4$ , the XRD pattern of the obtained FGS powder upon annealing exhibited a pyrrhotite phase as shown in Figure 4.8. Comparing to  $\text{GeI}_4$ ,  $\text{Ge}(\text{Gly})_2(\text{H}_2\text{O})_2$  precursors are coordination complexes which is easier to dissolve in organic solvent. In this prepared  $\text{Ge}(\text{Gly})_2(\text{H}_2\text{O})_2$ , the glycolate molecule forms a five-membered chelate ring with the Ge cation and it has a higher reactivity than  $\text{GeI}_4$  due to the presence of carbonyl group of glycolate groups<sup>[84]</sup>. Thus, the using of  $\text{Ge}(\text{Gly})_2(\text{H}_2\text{O})_2$  as the Ge source is supposed to be a key factor in this synthesis of FGS precursor. It is worth noting that the prepared  $\text{Ge}(\text{Gly})_2(\text{H}_2\text{O})_2$  powder is unstable and should be stored in a vacuum oven at room temperature.

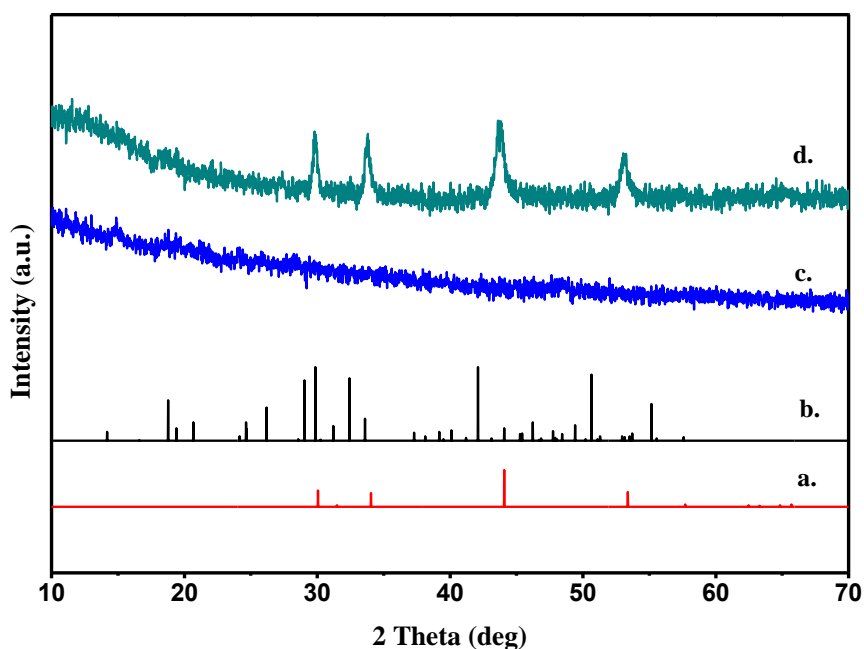


**Figure 4.8.** XRD patterns of FGS powders prepared from  $\text{GeI}_4$ . (a) Standard XRD pattern of  $\text{Fe}_7\text{S}_8$ ; (b) Standard XRD pattern of FGS; (c) XRD patterns of the as-synthesized FGS using  $\text{GeI}_4$ ; (d) XRD patterns of the annealed FGS synthesized using  $\text{GeI}_4$ .

#### 4.3.1.1.2. Option of Reaction Time

Based on the amorphous nature of as-synthesized FGS precursor, the effect of reaction time on the conversion of FGS precursor powder to FGS crystals was investigated, in which the reaction time extended from 15 minutes to 2 hours. As shown in Figure 4.9, XRD patterns of FGS precursors synthesized using different times exhibited that the FGS precursor synthesized over 2 hours was still in an amorphous state, suggesting that increasing the reaction time did not result in the conversion of FGS from amorphous to crystalline.

Therefore, the solution-processed FGS precursor shown herein requires only 15 minutes, which is shorter than any previous report on FGS synthesis.

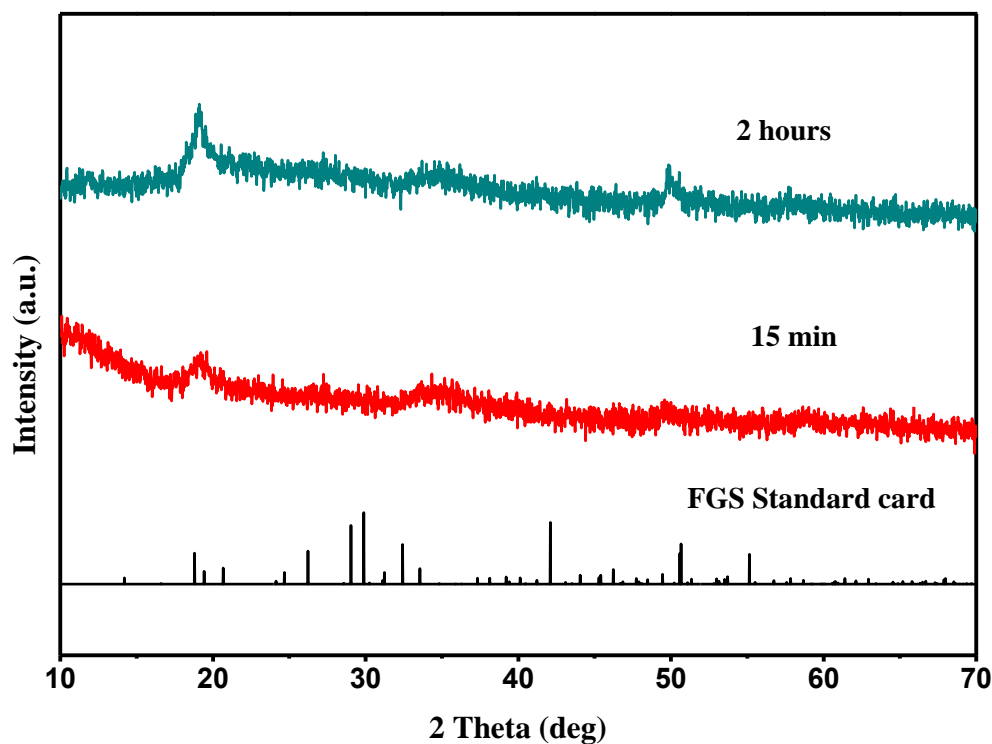


**Figure 4.9.** XRD patterns of FGS precursor powders using different reaction time.

In summary, the FGS precursors could be synthesized by a 15-min reaction of  $\text{Fe}(\text{acac})_3$ ,  $\text{Ge}(\text{Gly})_2(\text{H}_2\text{O})_2$ , and elemental sulfur when using oleylamine as the solvent. However, the FGS precursor powder obtained using oleylamine is easily and quickly degraded. To improve the shelf life of the FGS precursor, we have studied the selection of solvent used.

#### *4.3.1.1.3. Selection of Solvent*

A report by Kauzlarich et al. presents that Ge NPs prepared in alkenes, especially in the ODE, possess a good stability and oxidation resistance<sup>[85]</sup>. This suggests that ODE may have the ability to stabilize Ge-based compounds. Thereby, in this solution-phase approach for preparing FGS precursors, we studied the effect of using the mixture OLA & ODE (V: V, 2:1) in comparison to using only OLA as the solvent.

Figure 4.10 presents the color change of the FGS precursor powder made from OLA (a) and the FGS precursor powder made from a mixture of OLA & ODE (b). It is apparent that the FGS precursors synthesized from only OLA began to change after two days, whereas the FGS precursors prepared using a mixture of OLA and ODE remained visibly intact even after storage for seven days in air. After exposure to air for two days, the FGS precursors prepared in these two routes were respectively annealed in the tube furnace at 550°C for 2 hours. The XRD patterns of these annealed FGS powders in Figure 4.11 indicate that the FGS precursors prepared in OLA-ODE can still produce the FGS phase, while the precursors made only from OLA decompose in two days to form pyrrhotite ( $\text{Fe}_7\text{S}_8$ ) phase<sup>[86]</sup>. Thereby, the introducing of ODE can stabilize the synthesized FGS precursor.

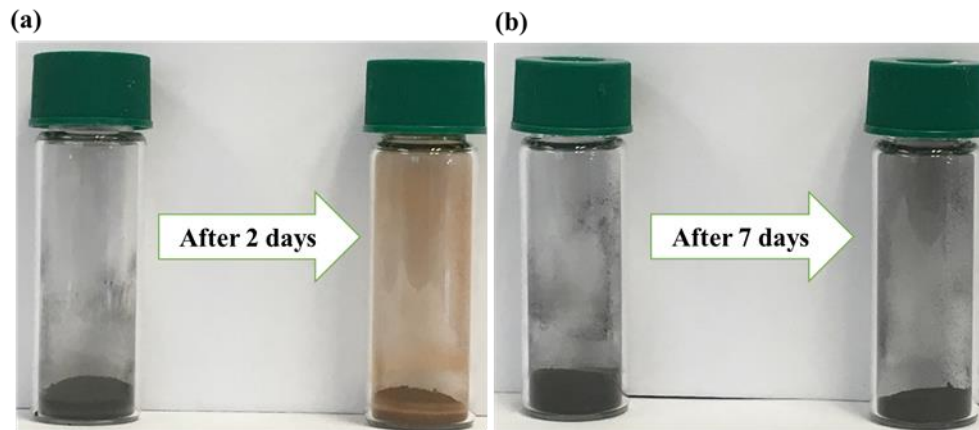


**Figure 4.10.** Color change of FGS precursor made from different solvents. **(a)** FGS precursor prepared using OLA as solvent; **(b)** FGS precursor prepared using a mixture of OLA and ODE [69].

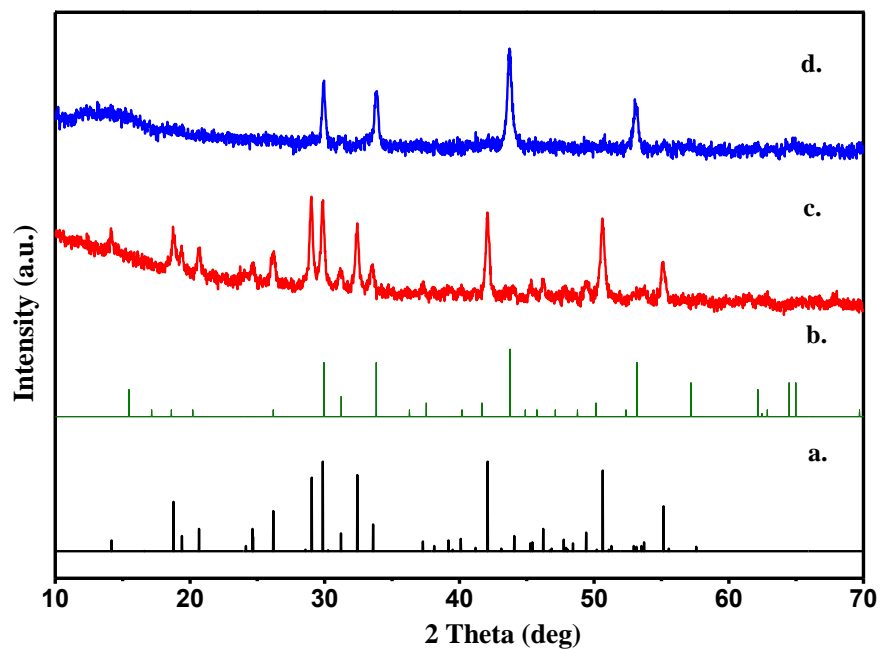


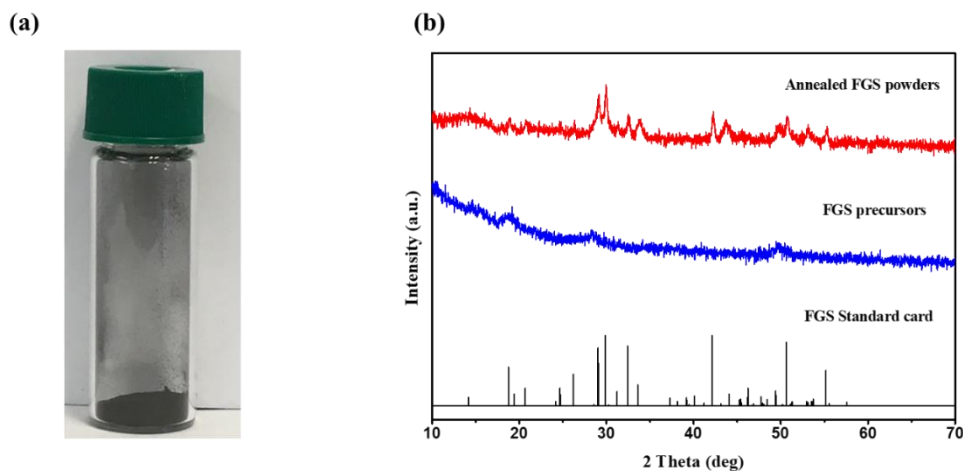
**Figure 4.11.** XRD pattern of the FGS powder that was annealed after two days of exposure. **(a)** Standard XRD pattern of FGS; **(b)** Standard XRD pattern of Fe<sub>7</sub>S<sub>8</sub>; **(c)** XRD patterns of the annealed FGS which synthesized using OLA; **(d)** XRD patterns of the annealed FGS which synthesized using the OLA–ODE mixture [69].

Further, the elemental composition of the as-synthesized FGS powders was analyzed by X-ray fluorescence (XRF), which exhibited a Fe/Ge atomic percent ratio of 2.3 and 2.5 for the FGS precursors made using OLA and that using OLA-ODE, respectively. But the S/(Fe+Ge) ratio is about 1.2 in both these two cases, which is close to the stoichiometry.

In summary, the selected experimental conditions for the synthesis of FGS precursors are as follows: Fe (III) 2,4-pentanedionate is the Fe precursor; Ge(Gly)<sub>2</sub>(H<sub>2</sub>O)<sub>2</sub> is the Ge source; elemental sulfur powder is the sulfur source; the solvent is a mixture of OLA & ODE ( V: V, 1:2); the reaction time is 15 minutes.

#### 4.3.1.2. Results of Synthesized FGS Precursors

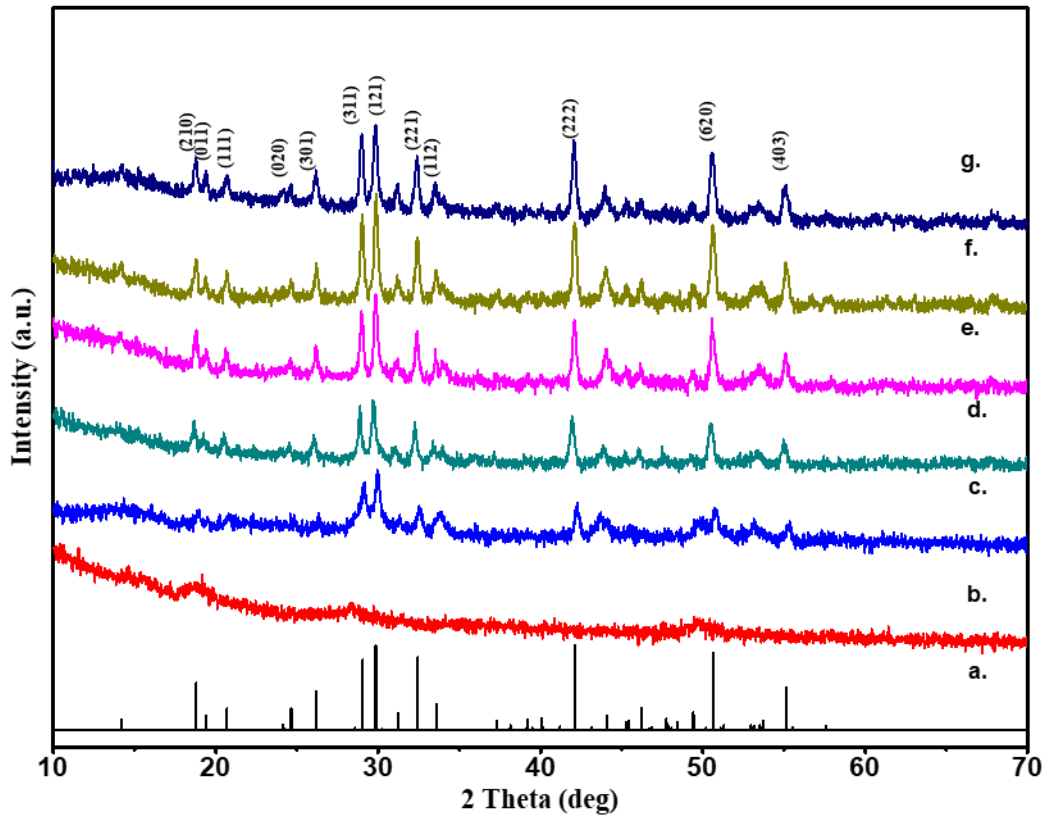
From the photograph and XRD pattern of the FGS precursors in Figure 4.12, it is apparent that the synthesized FGS precursors are amorphous black powders which enable generate to FGS crystals after thermal treatment.



**Figure 4.12.** (a) Photograph of FGS precursors; (b) XRD pattern of As-synthesized FGS precursors and annealed FGS powders <sup>[69]</sup>.

### 4.3.2. Results of Prepared Fe<sub>2</sub>GeS<sub>4</sub> Powders

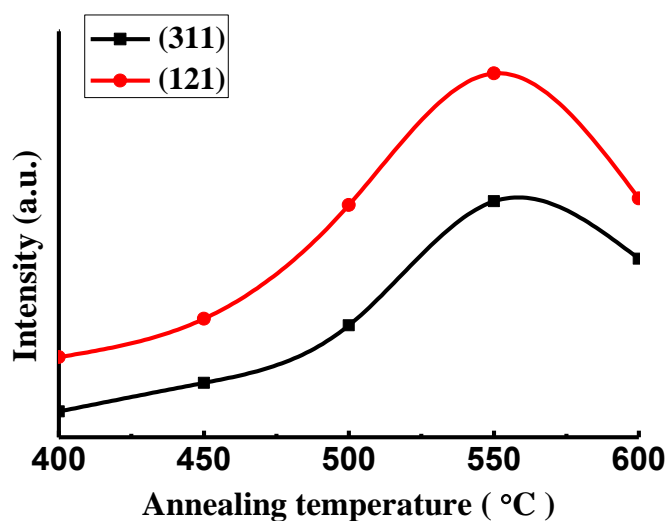
In order to obtain a high crystallinity FGS powder, a study has been conducted on the thermal treatment of the as-synthesized FGS precursor powders. FGS precursors were annealed at different temperatures ranging from 400°C to 600°C. The results of this annealing study were analyzed via XRD. Looking at the XRD pattern in Figure 4.13, we can see that the predominantly formed phase is FGS regardless of the annealing temperature. However, the XRD pattern of FGS annealed at higher temperatures presented all the FGS standard peaks with high intensity, while in the XRD pattern of FGS powder annealed at low temperature (400°C), some small peaks in the FGS standard card did not appear. Therefore, the FGS powder annealed at the higher temperature has higher crystallinity.



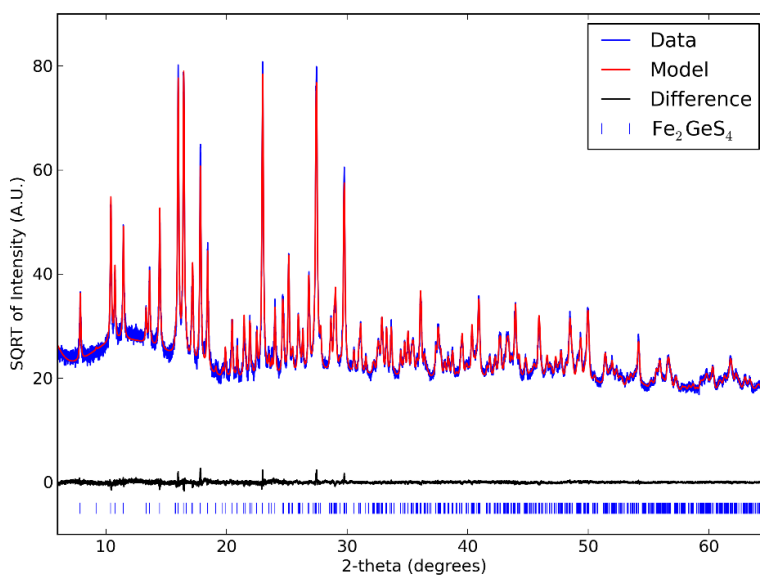
**Figure 4.13.** XRD patterns of FGS powder annealed at different temperature. (a) FGS standard card; (b) FGS precursors; (c) 400°C for 2 hours; (d) 450°C for 2 hours; (e) 500°C for 2 hours; (f) 550°C for 2 hours; (g) 600°C for 2 hours.

To look at the results a little more closely, we amplified the peaks of 28.96° and 29.84°, which are the primary diffraction peaks (311) and (121) of FGS, respectively. The line graph in Figure 4.14 shows the peak intensity of the (311) and (121) peaks as a function of annealing temperature. It is observed that as the annealing temperature increased, the intensity of these two peaks gradually increased except for 600°C, indicating that the overall crystallinity of FGS increased and reached an optimum value at 550°C.

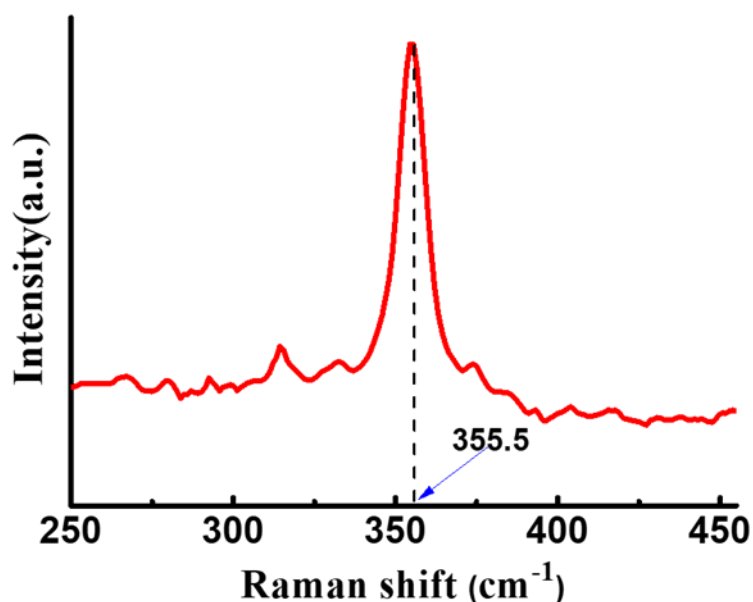
Thus, a pure high-crystallinity FGS powder could be obtained by annealing the FGS precursors in a tube furnace at 550°C under sulfur and argon atmosphere for 2 hours, which was also confirmed by the synchrotron XRD pattern in Figure 4.15.



**Figure 4.14.** Intensity comparison of the most intense XRD peaks from the FGS powders annealed at different temperature.



**Figure 4.15.** Synchrotron X-Ray analysis of annealed FGS powder <sup>[69]</sup>.



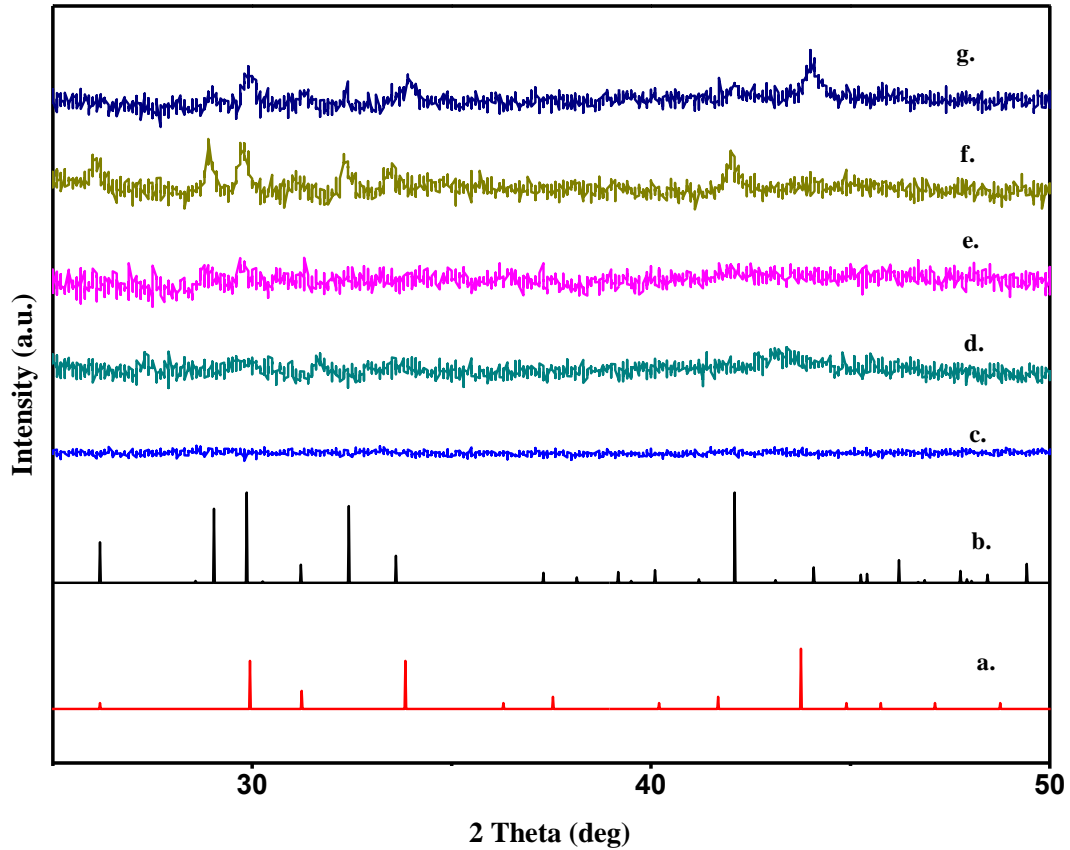
**Figure 4.16.** Raman spectrum of annealed FGS powders.

Figure 4.16 shows the measured Raman spectrum of the annealed FGS powder, which exhibits a significant peak at  $355\text{ cm}^{-1}$ . This special scattering position belongs to the olivine structure of FGS and is consistent with the  $360\text{ cm}^{-1}$  reported by Park et al. [25].

### 4.3.3. Results of FGS Thin Films

To make the thin films suitable for photovoltaic cells, we fabricated the FGS thin films by dip-coating and then annealed these deposited thin films in the sulfur and argon atmosphere at temperatures ranging from  $400\text{-}600^\circ\text{C}$ . Figure 4.17 shows the XRD patterns of these thin films that annealed at different temperatures. Consistent with the results of the annealing study performed on the FGS powders, the FGS thin films also tend to require the optimal annealing temperature of  $550^\circ\text{C}$ . This result indicated by the fact that the XRD pattern of the sample

annealed at 550°C exhibits only the FGS phase and the two major FGS diffraction peaks (311) and (121) of the FGS sample annealing at 550°C have the highest intensity.



**Figure 4.17.** XRD patterns of FGS thin films annealed at different temperature. (a) Pyrrhotite Fe<sub>7</sub>S<sub>8</sub> standard card; (b) FGS standard card; (c) 400°C for 2 hours; (d) 450°C for 2 hours; (e) 500°C for 2 hours; (f) 550°C for 2 hours; (g) 600°C for 2 hours <sup>[69]</sup>.

In order to understand how long it took to form a high-quality FGS thin film, three deposited FGS thin films were annealed at 550 ° C for 1 hour, 2 hours, and 3 hours, respectively. As shown in Figure 4.18, the XRD patterns of these three films show that the primarily formed phase is FGS, regardless of the annealing time. Especially for the thin film annealed for 2 hours,

there were no secondary phases generated. Thus, the optimal annealing condition for the FGS thin film is carried out at 550°C for 2 hours.

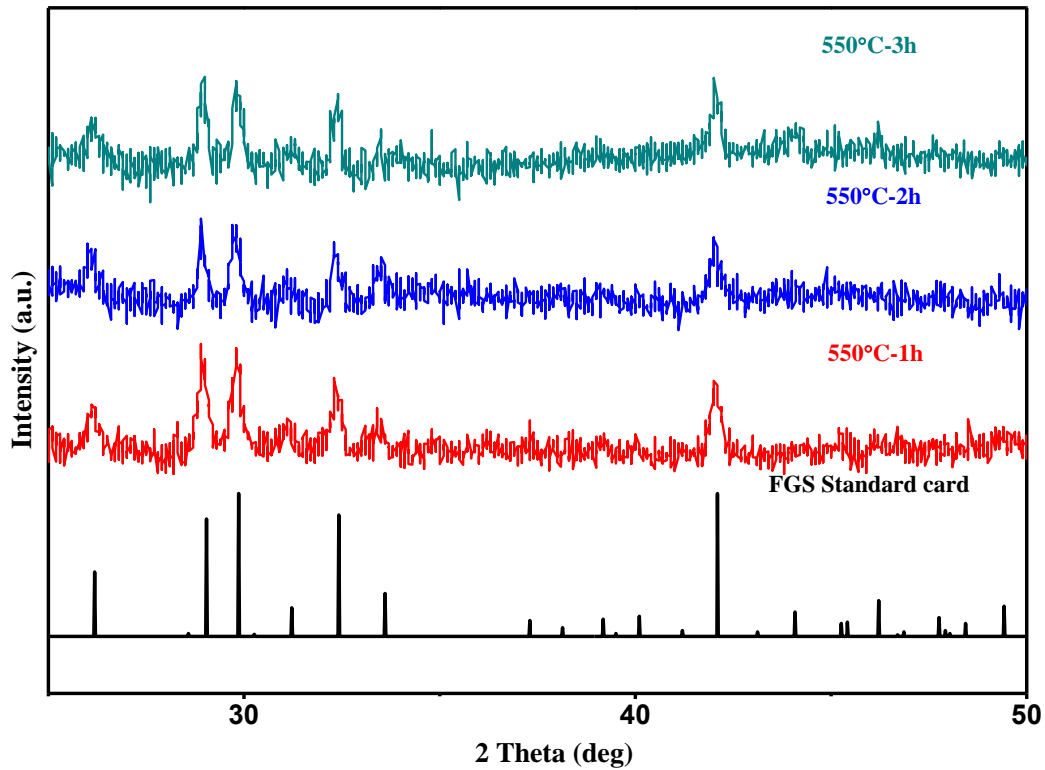


**Figure 4.18.** Comparison of XRD patterns of FGS thin film annealed at 550 °C for different times <sup>[69]</sup>.

Figure 4.19 depicts the Raman spectrum of the FGS thin film obtained under the optimized annealing condition. Once more a Raman peak at around  $355.5\text{ cm}^{-1}$  was observed which belongs to the olivine structure of  $\text{Fe}_2\text{GeS}_4$  phase. This result is in good agreement with the Raman scattering literature of FGS measured by Park et al. <sup>[25]</sup>.

Furthermore, the band gap of the FGS thin film prepared under the optimum conditions was analyzed using the photoluminescence (PL) spectroscopy, which exhibited a value of around

1.4 eV, as shown in Figure 4.20. This result is consistent with the band gap of 1.40 eV calculated by Yu et al. [24] and the previously reported value of 1.43 or 1.38 eV by Park's group [25].

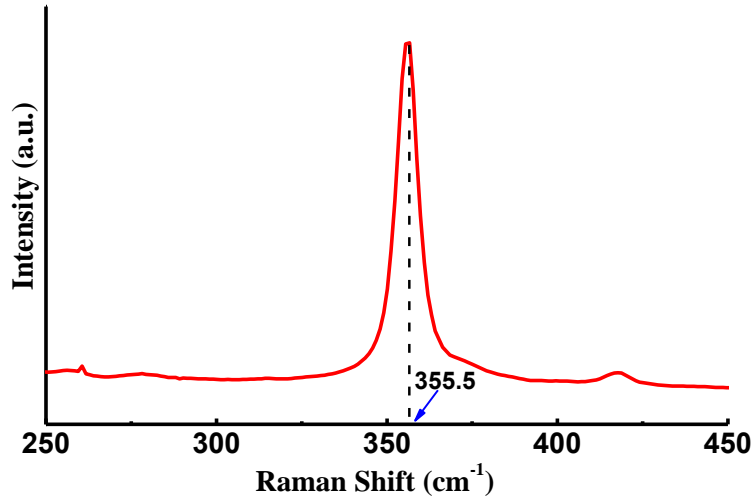


**Figure 4.19.** Raman spectrum of FGS thin film annealed at 550°C for 2 hours [69].

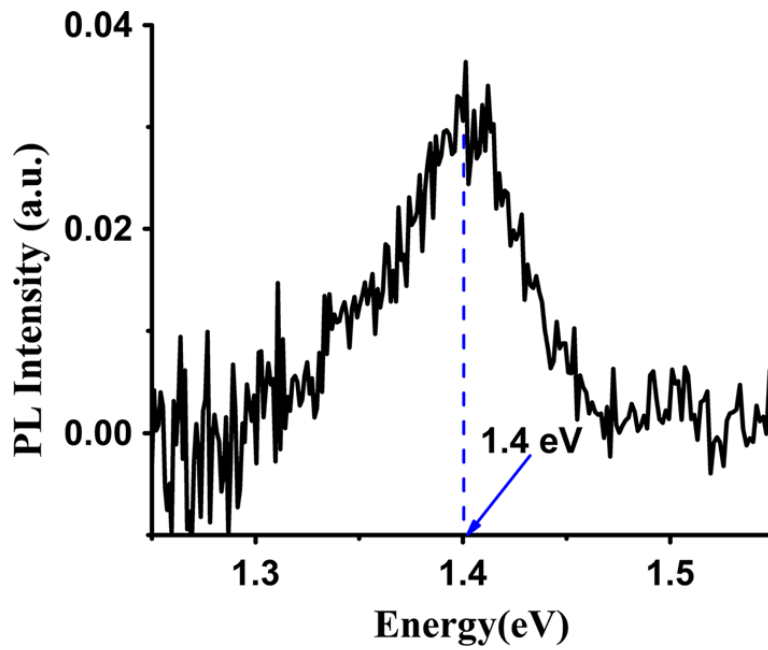


**Figure 4.20.** FGS thin-film band gap evaluation [69].

Moreover, it is well known that the morphology and thickness of the films have a significant impact on their application in photovoltaic cells. For example, the grain boundaries of the thin film can influence the recombination in the thin film. In this doctoral dissertation, the cross-section of the FGS thin film annealed under the optimal conditions was characterized by Scanning Electron Microscopy (SEM). The SEM image in Figure 4.21 presents that the annealed FGS thin film has a limited grain-growth and a thickness of about 1 $\mu$ m, making it suitable for the photovoltaic applications <sup>[69]</sup>.

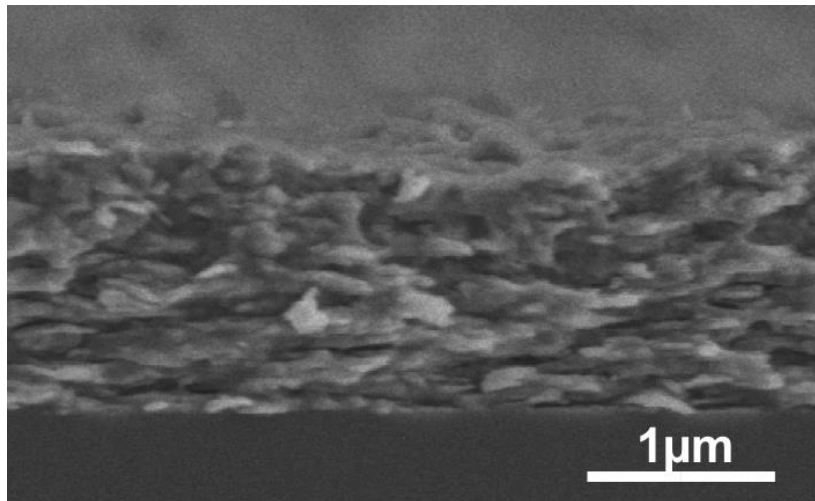


**Figure 4.21.** SEM Cross section of annealed FGS thin film <sup>[69]</sup>.

In summary, the FGS thin films which annealed at 550°C for 2 hours have high purity, suitable thickness, and good optical and electrical properties for solar cells.

#### 4.3.4. Performance of FGS Thin Films in Photovoltaic Devices

So far, although Prieto and Fredrick have reported a measured photocurrent of FGS thin film, there is still no FGS-based solar cell produced. In this research, I fabricated FGS-catalyzed dye-sensitized solar cells (DSSC) successfully to test the potential application of the obtained FGS thin films as the counter electrodes in FGS-catalyzed DSSC. This design of FGS-catalyzed DSSC comes from both the report by Xin et al. (2011) and that by Tong et al. (2014), which pronounced that the chalcogenide semiconductors could be performed as the counter electrodes in dye-sensitized solar cells <sup>[76,77]</sup>.

First, a typical dye-sensitized solar cell (DSSC) has the structure of ITO/TiO<sub>2</sub>&Dye/Electrolyte/Mo, as shown in Figure 4.4. The photocurrent density-voltage (J-V) curve of this DSSC, as shown in Figure 4.22, was recorded by Keithley 2400 source meter under simulated AM 1.5 G illumination, which exhibited a photovoltaic behavior with an open-circuit voltage ( $V_{OC}$ ) of 467 mV and a short-circuit current density ( $J_{SC}$ ) of 0.68 mA·cm<sup>-2</sup>. Fitting of this curve to the functions of fill factor (FF) (equation 1.3) and conversion efficiency ( $\eta$ ) (equation 1.4) showed that the fill factor and conversion efficiency ( $\eta$ ) of this DSSC was 43.0% and 0.14%, respectively <sup>[69]</sup>.

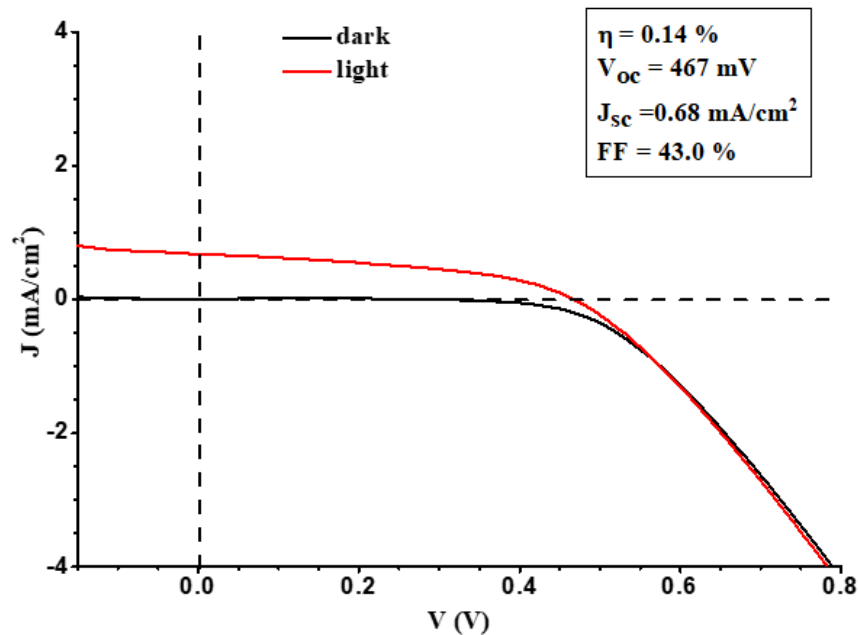


**Figure 4.22.** Device characteristics for DSSC (ITO/TiO<sub>2</sub>&Dye/Iodine solution/Mo) <sup>[69]</sup>.

To clarify the contribution of FGS thin film to the dye-sensitized solar cell (DSSC), we incorporated the FGS into the above DSSC to form FGS-catalyzed DSSC with a structure of ITO/TiO<sub>2</sub>&Dye/Electrolyte/FGS /Mo, as shown in Figure 4.5 (a). In this typical FGS-catalyzed DSSC, the thin film of FGS deposited on Mo substrate was incorporated as a counter electrode while the thin film of dye-sensitized TiO<sub>2</sub> deposited on ITO substrate performed as the photoelectrode. As shown in Figure 4.23, the J-V characteristics of the FGS-catalyzed DSSC exhibit a higher open-circuit voltage ( $V_{OC}$ ) of 544 mV and a short-circuit current density ( $J_{SC}$ ) of 4.15 mA·cm<sup>-2</sup>, resulting in the increased conversion efficiency ( $\eta$ ) of 0.71%. This increase in short-circuit current density ( $J_{SC}$ ) can be attributed to the addition of the light absorption of FGS when introducing it into the DSSC. For the decrease in fill factor, we can speculate that it is due to the increase in series resistance. Series resistance in a DSSC caused by several parts, such as

the transparent conductive oxide, the electrolyte layer and the counter electrode. Comparing FGS-catalyzed DSSC and DSSC without FGS, the only change is the addition of FGS layer. So, we can only speculate now that there probably is high density of trap states in FGS thin film which increased the series resistance of the FGS-catalyzed DSSC [87].

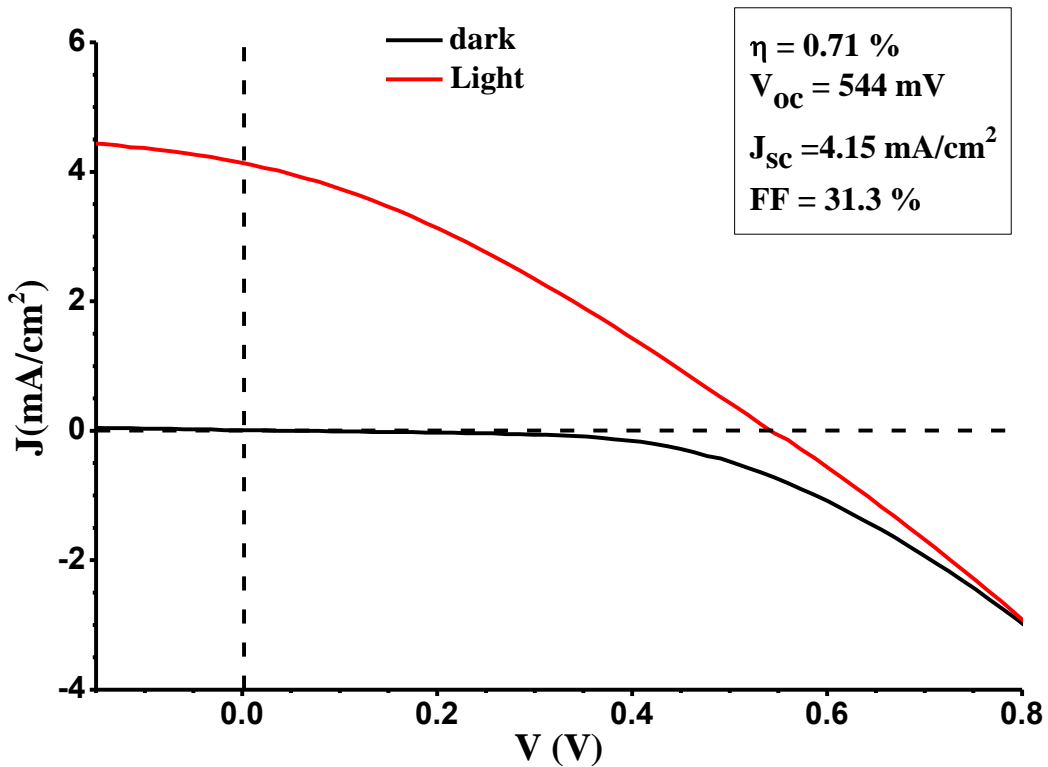


**Figure 4.23.** Device characteristics for FGS-catalyzed DSSC (ITO/TiO<sub>2</sub>&Dye/Iodine solution /FGS/Mo) [69].

Furthermore, an FGS-catalyzed DSSC using FGS coated on FTO substrate as the counter electrode was also fabricated following the same approach to the above constructs, which possessing a structure of ITO/TiO<sub>2</sub>&Dye/Electrolyte/FGS/FTO, as shown in Figure 4.5 (b). Compared to the FGS-catalyzed DSSC using Mo, the J-V curve of this photovoltaic device

showed a lower short-circuit current density ( $J_{sc}$ ) of  $2.93 \text{ mA}\cdot\text{cm}^{-2}$  with a lower open-circuit voltage ( $V_{oc}$ ) of  $537 \text{ mV}$ , but a higher fill factor of  $33.17$ , resulting in a conversion efficiency ( $\eta$ ) of  $0.52\%$ , as shown in Figure 4.24.

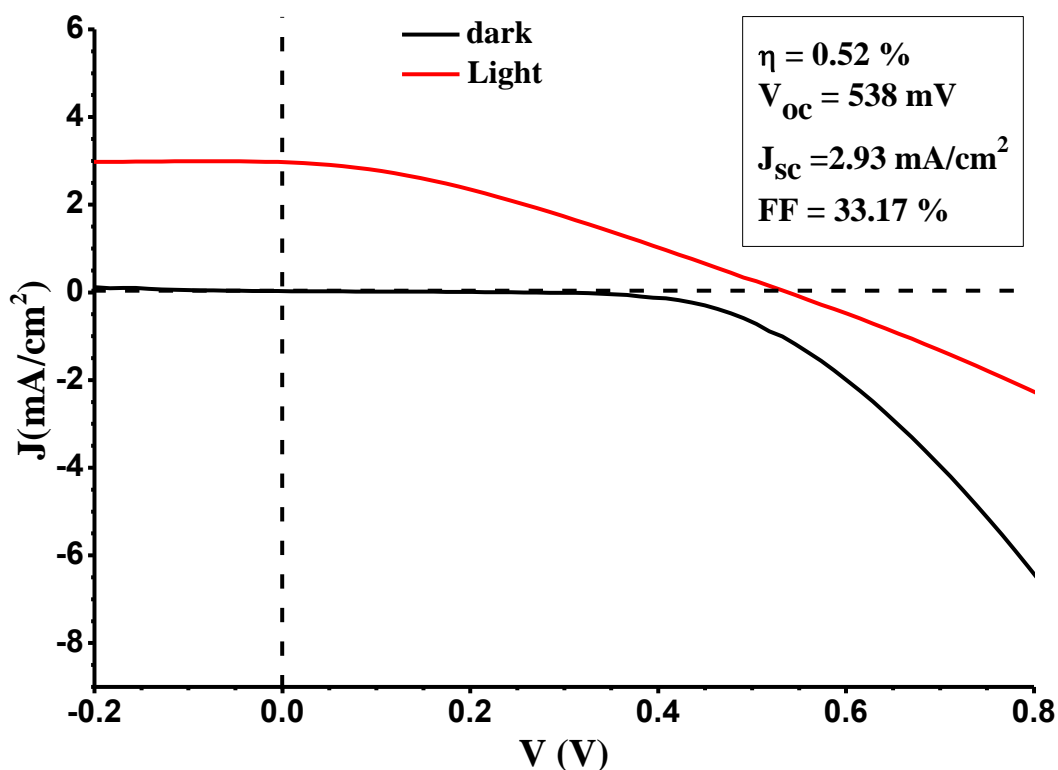


**Figure 4.24.** Device characteristics for FGS-catalyzed DSSC (ITO/TiO<sub>2</sub>&Dye/Iodine solution/FGS/FTO).

The relevant photovoltaic performance parameters for these three photovoltaic devices are summarized in Table 4.2. As can be seen from Table 4.2, both the FGS-catalyzed DSSC using Mo and the FGS-catalyzed DSSC using FTO have higher conversion efficiency ( $\eta$ ), short-circuit current density ( $J_{sc}$ ), and open-circuit voltage ( $V_{oc}$ ) than DSSC without FGS. However, the increase in these parameters of the FGS-catalyzed DSSC using Mo is different from the FGS-

catalyzed DSSC using FTO. Therefore, the contribution of FGS on counter electrode ascribed to the added light absorption of FGS thin film rather than an improved band alignment [69].

**Table 4.2.** Photovoltaic performance of DSSCs with different counter electrode.

Photovoltaic device	J <sub>sc</sub> (mA·cm <sup>-2</sup> )	V <sub>oc</sub> (mV)	FF (%)	H (%)
DSSC without FGS	0.68	467	43.0	0.14
FGS-catalyzed DSSC using Mo	4.15	544	31.3	0.71
FGS-catalyzed DSSC using FTO	2.93	537	33.17	0.52

As described above, in the FGS-catalyzed dye-sensitized solar cell, the FGS thin film contributes a certain amount to the light absorption. And it is well known that the dye-sensitized TiO<sub>2</sub> thin film is used as a photoelectrode which absorbs light in a DSSC. Therefore, in my doctoral work, I have fabricated an FGS solution-based solar cell to dissociate the light absorption of FGS from the light absorption of the dye.

As shown in Figure 4.6, the FGS solution-based solar cell was assembled in the same constructs as the FGS-catalyzed DSSC, but the original TiO<sub>2</sub> thin film was used instead of the dye-sensitized TiO<sub>2</sub> thin film. The resulting structure was ITO/TiO<sub>2</sub>/Electrolyte/FGS /Mo. In such a photovoltaic device, the TiO<sub>2</sub> thin film worked as n-type while the FGS thin film performed as p-type that absorbs light. The measured J-V curve of this FGS solution-based solar cell, as displayed in Figure 4.25, exhibits a low conversion efficiency ( $\eta$ ) of 0.03%, which is primarily ascribed to the extremely low short-circuit current density (J<sub>sc</sub>) of 0.19 mA·cm<sup>-2</sup>.

However, this FGS solution-based photovoltaic device exhibits a relatively high open-circuit voltage ( $V_{OC}$ ) of 361 mV. It is worth noting that whether a material is a promising light absorbing material is related to its ability to achieve high  $V_{OC}$ . Therefore, it is safe for us to conclude that our fabricated FGS thin film is a promising candidate for photoactivity in photovoltaic applications.

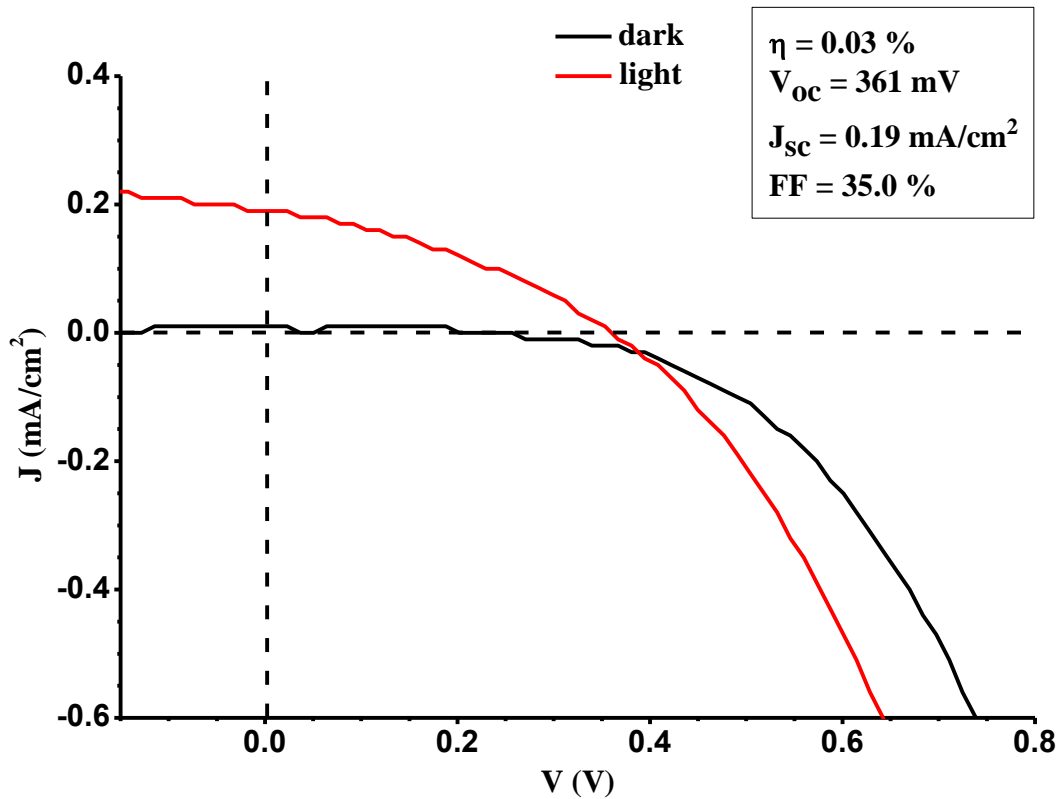


**Figure 4.25.** Device characteristics for FGS solution-based solar cell (ITO/TiO<sub>2</sub>/Iodine solution/FGS/Mo) <sup>[69]</sup>.

As mentioned in Chapter 1, the short-circuit current density ( $J_{SC}$ ) is related to light intensity, the spectrum of incident light, optical properties, and collection probability. Excluding the effects of external conditions, the collection probability is a major factor for the low short-

circuit current density ( $J_{SC}$ ) of such FGS solution-based photovoltaic device. In general, photovoltaic devices convert solar energy into electrical energy by two main processes: 1) absorbing incident light and generating electron-hole pairs; 2) Collecting carriers by the p-n junction to prevent the recombination of the electron-hole pairs. In the second process, the ‘collection probability’ is the key factor, which explains the probability that a carrier produced by light absorption in a specific area of the cell will be collected by a p-n junction and thus contribute to the light-generated current <sup>[88]</sup>. Scientific research has shown that the ‘collection probability’ is related to the distance that a carrier generated by light absorption needs to move and the surface characteristics of the photovoltaic device. Therefore, we can conclude that this FGS solution-based photovoltaic device has poor ability to collect the light-generated carriers and drive them to the current, resulting in its low short-circuit current density ( $J_{SC}$ ). For the low current extraction of this device, we can only speculate that it may be caused by the high density of defect states <sup>[69]</sup>.

#### **4.4. Conclusion**

In this work, we presented a two-step approach for the preparation of  $Fe_2GeS_4$  crystals, including a solution-processed synthesis of FGS precursor and a thermal treatment. The optimization of the synthetic procedure suggests that the FGS precursor could be synthesized by a solution-phase reaction of Fe (III) 2,4-pentanedionate,  $Ge(Gly)_2(H_2O)_2$ , and sulfur powder in OLA-ODE, using only 15 minutes. Optimization of the thermal treatment for both the FGS powders and the FGS thin films suggests that annealing at 550 °C for 2 hours under argon and sulfur atmosphere is the optimum condition. The room-temperature photoluminescence

measurement on FGS thin films showed a band gap of about 1.40 eV. When the FGS thin film acted as the counter electrode in a dye-sensitized solar cell, an enhanced open-circuit voltage and power conversion efficiency were achieved, compared to a DSSC without FGS. Moreover, the FGS solution-based solar cell in which FGS thin film worked as a light absorbing layer displayed a significantly high open-circuit voltage ( $V_{OC}$ ) of 361 mV. Thus,  $Fe_2GeS_4$  holds the potential to absorb photons and convert light into electricity, indicating it is a promising candidate for photoactivity in photovoltaic applications.

## CHAPTER 5. ONE-POT SYNTHESIS OF $\text{Fe}_2\text{GeS}_4$ NANOCRYSTALS AND SOLAR CELLS

### 5.1. Introduction

As mentioned previously, the  $\text{Fe}_2\text{GeS}_4$  material is considered to be a promising semiconductor, not only because it has a high absorption coefficient of  $10^5 \text{ cm}^{-1}$ , a suitable band gap of 1.4 eV, but also better sustainability, as well as the toxicity of its constituent is relatively low [24]. In the development of  $\text{Fe}_2\text{GeS}_4$ , various methods have been applied to the preparation of  $\text{Fe}_2\text{GeS}_4$  materials, however, a time-saving synthesis of  $\text{Fe}_2\text{GeS}_4$  nanosheets was reported by Lim et al. in 2016. In this report, single-crystalline  $\text{Fe}_2\text{GeS}_4$  nanosheets were prepared in oleylamine using the one-pot method, and the obtained  $\text{Fe}_2\text{GeS}_4$  nanosheets possessed a large size of about 800 nm and a thickness of 64 nm [66]. It is well known that the size and shape of a semiconductor can extensively affect its physical and chemical properties, even affecting its photovoltaic applications [89,90]. Small nanocrystals with narrow size distributions contribute to their photovoltaic performance due to size quantization effect [91-93]. In addition, as we know, the crystal size can be tuned by adjusting several reaction parameters such as the reactants, the reaction time, reaction temperature, and so on. Further, one-pot synthesis is an approach in which the reactants undergo a continuous reaction in only one reactor, which makes the process easier to handle.

Taking into account the advantages of one-pot synthesis and the size requirement of the resulting FGS nanomaterials, we attempted to improve the Lim's route for synthesizing  $\text{Fe}_2\text{GeS}_4$  (FGS) nanosheets though adjusting several reaction parameters. The obtained FGS nanosheets

were deposited on a substrate and then annealed at 400 °C under argon and sulfur atmosphere to fabricate a high-quality FGS thin film. The resulting FGS thin film was subjected to a photovoltaic device to investigate its photovoltaic performance.

## 5.2. Experimental Section

As shown in Figure 5.1, the fabrication of FGS NPs based solar cell involves three processes: 1) synthesis of FGS nanoparticles; 2) fabrication of FGS thin films; 3) assembly of the FGS NPs based solar cells and measuring the photocurrent density-voltage (J-V) of the fabricated photovoltaic devices.

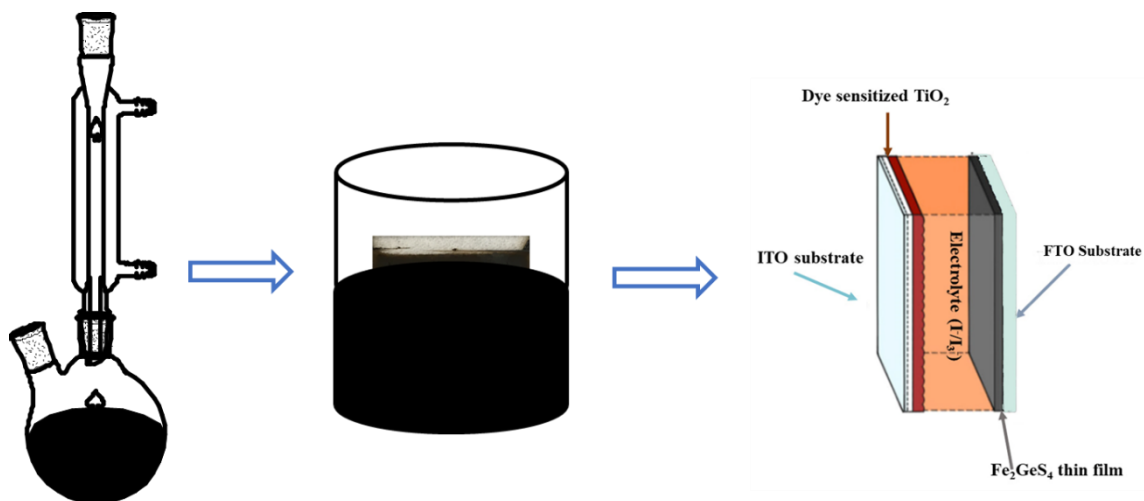


**Figure 5.1.** Fabrication of FGS NPs-catalyzed dye-sensitized solar cells.

### 5.2.1. Synthesis of FGS Nanocrystals

The FGS nanosheets herein were synthesized via a method that was modified from the procedure of Lim et al. <sup>[67]</sup>. The  $\text{Ge}(\text{Gly})_2(\text{H}_2\text{O})_2$  powders prepared as described in chapter 4 was still used as the Ge source in this chapter.

In a typical synthesis of  $\text{Fe}_2\text{GeS}_4$  nanoparticles,  $\text{FeCl}_2$  (3 mmol, 0.380 g),  $\text{Ge}(\text{Gly})_2(\text{H}_2\text{O})_2$  (3 mmol, 0.769g), Trioctylphosphine oxide (TOPO, 4 mmol, 1.546 g), 2mL of 1-dodecanethiol(1-DDT), and 20 mL of oleylamine (OLA) were added to a 100 mL 2-neck round bottom quartz flask. Next, the flask was connected to the Schlenk line technique and heated to 140 °C. Under magnetic stirring, the reaction system was held at 140 °C for 1 hour under vacuum to remove the moisture. Then the reaction system was filled with argon and heat to 260 °C, followed by stirring at 260 °C for 1.5 hours. Afterward, the reaction was heated to 320 °C and held for 2 hours. After cooling to room temperature, the resulting FGS precipitates were washed three times with an equal volume of chloroform and ethanol <sup>[66]</sup>. Finally, the as-synthesized FGS nanoparticles suspended in 12 mL of chloroform for further use.

In order to study the role of TOPO, a set of synthesis without using TOPO was designed to prepare FGS nanoparticles. The procedure used was the same as above, but no TOPO was added. Following this synthesized procedure, we collected the FGS NPs which reacted at 320 °C for different times, such as 2 hours, 2.5 hours and 3 hours. The resulting products were washed by the same route as the above procedure.

### **5.2.2. Fabrication of FGS Thin Films**

In a typical experiment, 12 mL of the above FGS-Chloroform solution was placed in an ultrasonic bath for 5 minutes to prepare a uniformly dispersed FGS ink. The resulting solution was coated on the clean substrates by dip-coating.

The cleaning process for substrates is the same as described in the previous chapter. The substrates were washed in an ultrasonic bath containing methanol, Milli-Q water, and acetone in sequence for 3 minutes, and then subjected them to a plasma cleaner to remove additional organic compounds on their surface [69].

For the dip-coating process, the general operation is the same as we described in chapter 4. First, a clean substrate was manually immersed in the FGS-Chloroform solution; next, the substrate was kept in the solution for 5 seconds; then, the deposited substrate was slowly taken out; the deposited thin film was dried in air for 3 minutes; afterwards, repeated the above steps for 11 times to get desired FGS thin film.

According to the reports by both Prieto and Park, FGS nanoparticles are oxidized under hours of air exposure [24,25]. To prevent oxidation of the prepared FGS thin film, we subjected it in a tube furnace and annealed it at 400°C for 2 h under the argon and sulfur atmosphere.

### **5.2.3. Solar Cells Fabrication**

The procedure for manufacturing FGS NPs based solar cells in this chapter is the same as that described in Chapter 4. Firstly, a dye-sensitized TiO<sub>2</sub> thin film was prepared according to the method proposed by Grätzel's group [75], in which the TiO<sub>2</sub> thin film was soaked in a dye

methanolic solution of ruthenizer 535-bis TBA (0.3 mmol/L) overnight; Secondly, the annealed FGS thin film was assembled face-on to the dye-sensitized TiO<sub>2</sub> thin film and clamped with two binder clips; Thirdly, 100 μL of iodide/triiodide-iodide solution that acted as an electrolyte was dropped into the gap between the two films; Finally, the assembled photovoltaic device was placed vertically such that the electrolyte could fill the entire gap between FGS thin film and the dye-sensitized TiO<sub>2</sub> thin film. The resulting structure of the FGS NPs-catalyzed dye-sensitized solar cell was ITO/TiO<sub>2</sub>&Dye/Electrolyte/ FGS/FTO, as shown in Figure 5.2.

To investigate the contribution of the FGS thin film to this FGS NPs -catalyzed DSSC, we fabricated two other photovoltaic devices. One is a DSSC without FGS, which has a structure of ITO/TiO<sub>2</sub>&Dye/Electrolyte/FTO, as shown in Figure 5.3 (a). Another one is assembled without adding a dye to form an FGS NPs solution-based solar cell with a structure of ITO/TiO<sub>2</sub>/Electrolyte/ FGS/FTO, as shown in Figure 5.3 (b). In such an FGS solution-based solar cell, the FGS thin film was performed as a light absorbing layer which absorbs light and converts it into electricity.

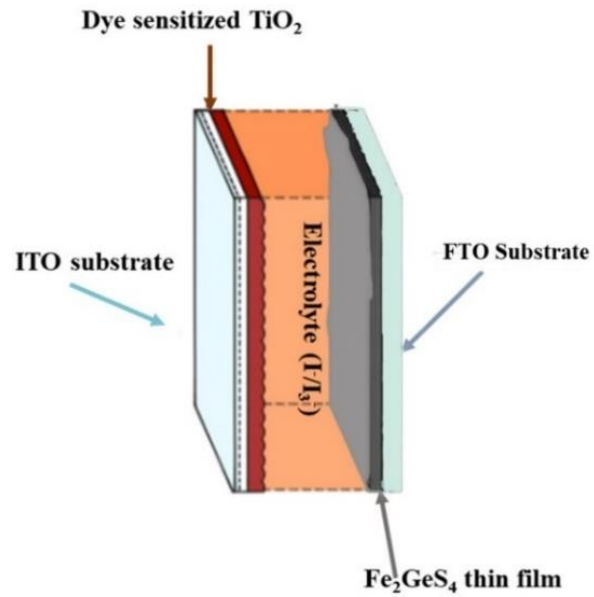


**Figure 5.2.** Structure of FGS NPs-catalyzed dye-sensitized solar cells. (ITO/TiO<sub>2</sub>&Dye/ Electrolyte/FGS/FTO).

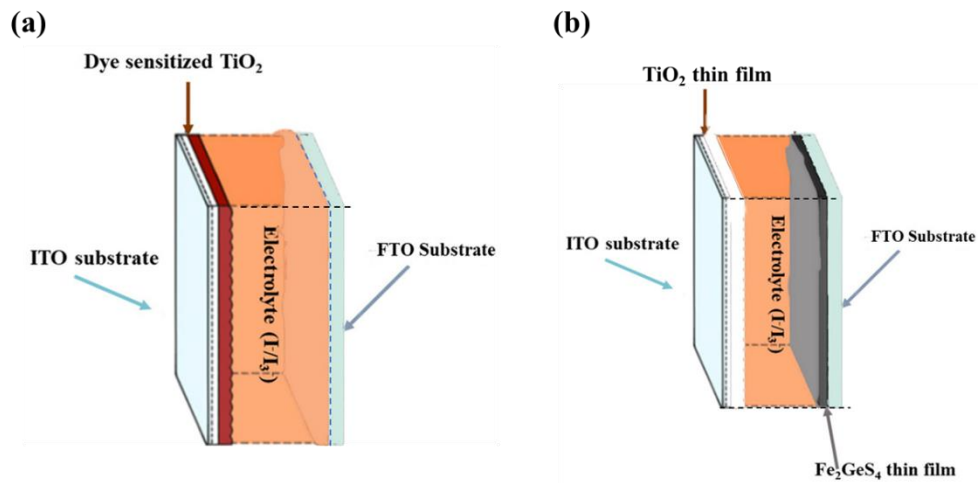


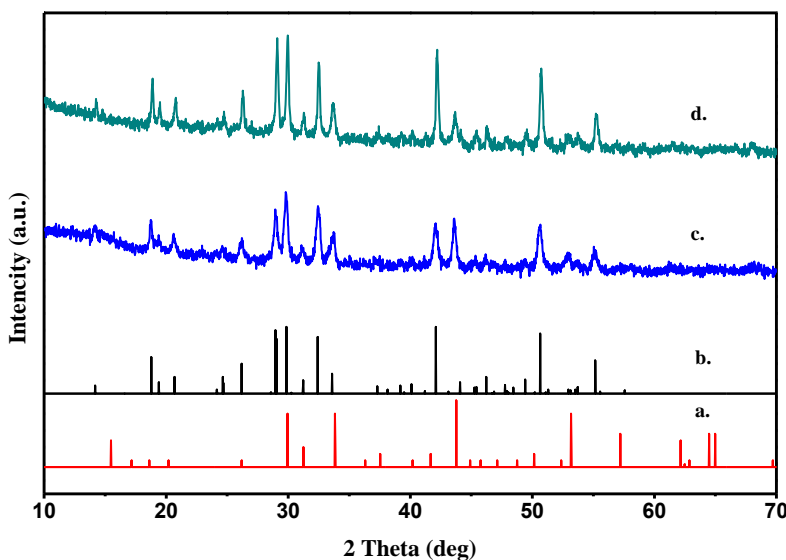
**Figure 5.3.** (a) Structure of DSSC without FGS (ITO/TiO<sub>2</sub>&Dye/ Electrolyte/FTO); (b) Structure of FGS solution-based solar cell (ITO/TiO<sub>2</sub>/Electrolyte/ FGS/FTO).

## 5.3. Results and Discussion

### 5.3.1. Results of Synthesis of FGS Nanocrystals

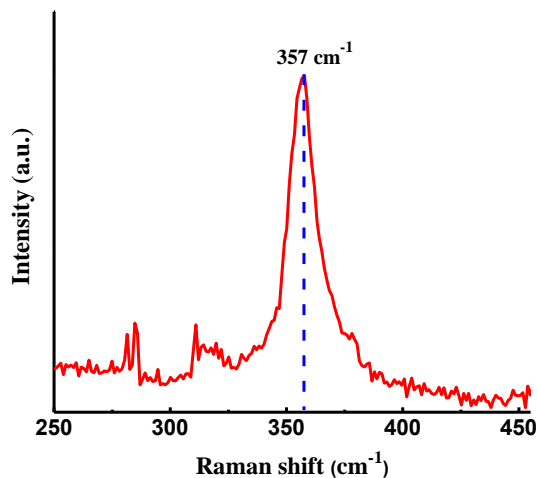
In the literature, TOPO strongly affects the growth kinetics of nanomaterials, enable to reduce the reaction time and even to control the size of the obtained nanomaterials <sup>[94-98]</sup>. In this work, to improve the properties of the obtained FGS nanoparticles, we added TOPO to the reaction starting materials.

Figure 5.4 presents the XRD pattern of FGS NPs prepared at 320 °C for different times. When the reaction mixture reacted at 320°C for 1 hour, the obtained product was a mixture of orthorhombic FGS and hexagonal Fe<sub>0.481</sub>S. However, when the reaction time extended to 2 hours, the Fe<sub>0.481</sub>S phase disappeared, and the XRD pattern of the product exhibited only the FGS phase.



**Figure 5.4.** XRD Patterns of FGS NPs prepared with TOPO. (a) Pyrrhotite standard card; (b) FGS Standard card; (c) FGS -TOPO-1h; (d) FGS-TOPO-2h.

Figure 5.5 shows the Raman spectrum of the obtained FGS nanoparticles, exhibiting only one peak at  $356\text{ cm}^{-1}$ . This result fits well with the  $361\text{ cm}^{-1}$  which reported by Park et al. [25]. TEM images in Figure 5.6 show that the as-synthesized FGS nanoparticles possess a plate-like shape and a varying size ranging from 400-800 nm. Although the resulting product didn't present a small uniform size as we expected, the reaction time had been reduced from 3.5 hours to 2 hours.



**Figure 5.5.** Raman spectrum of as-synthesized FGS NPs.

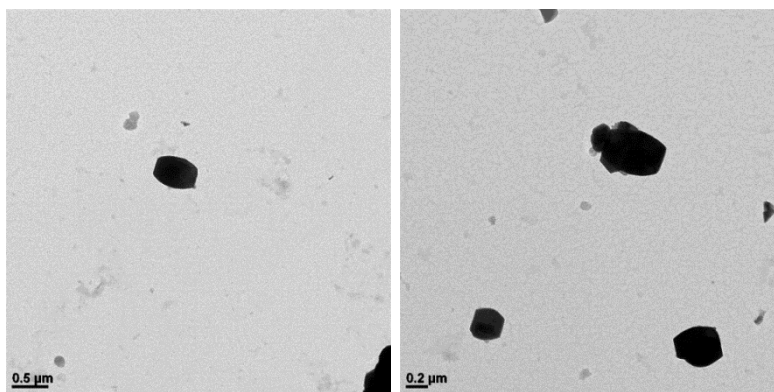


**Figure 5.6.** TEM images of as-synthesized FGS NPs.

Figure 5.7 shows the thermogravimetric analysis (TGA) of the as-synthesized FGS nanoparticles. Since that the capping reagent OLA has a high boiling point of 364 °C and the boiling point of TOPO is also high (201-202 °C), we speculate that the OLA and TOPO could also be further analyzed when performing thermogravimetric analysis on as-synthesized FGS NPs. With this in mind, in the thermogravimetric analysis of FGS NPs, the mass loss occurred at 380-450°C due to the evaporation of solvents residues such as OLA, TOPO. The rapid mass loss took place at the temperature ranging from 607-750 °C was speculated to be caused by the volatilization of GeS<sub>2</sub> which easily formed during the decomposition of FGS. In fact, we do not seek to identify the species formed during the thermogravimetric analysis, but rather to determine the temperature at which FGS begins to decompose.

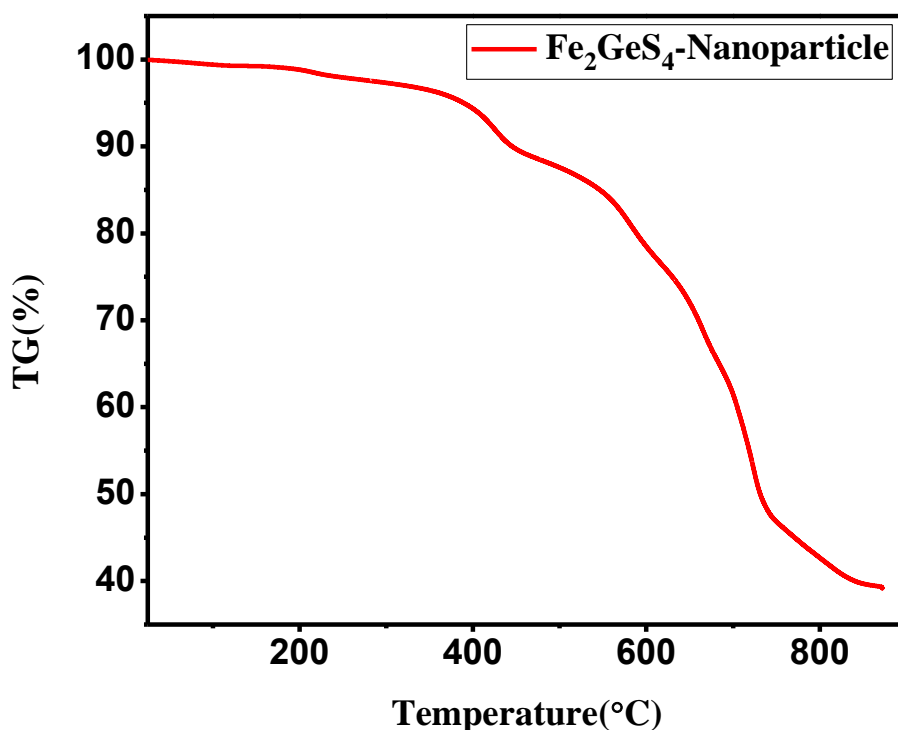


**Figure 5.7.** Thermogravimetric analysis (TGA) of as-synthesized FGS NPs.

### 5.3.2. Effects of Trioctylphosphine Oxide (TOPO)

A report by Peng et al. demonstrated that TOPO has a significant influence on the growth kinetics of CdSe, so as far to affect the shape of synthesized CdSe nanocrystals<sup>[98]</sup>. In order to determine the role of TOPO in the FGS synthesis, we carried out a series of experiments without adding TOPO and collecting the products at different times. The reaction time at 320°C was controlled at 2, 2.5, and 3 hours, respectively.

Figure 5.8 presents the XRD pattern of the as-synthesized FGS NPs prepared without TOPO and using different reaction times. When the same reaction time (2 hours) as the FGS synthesis with TOPO was used, the reaction without TOPO produced only the pyrrhotite phase. In the reaction which no TOPO reagent added, when the reaction time at 320 ° C was increased to 2.5 hours, the formation of FGS began. However, if TOPO was added to the reaction, FGS was formed as long as reacting at 320°C for 1 hour, as shown in Figure 5.4. Further, when the reaction time was extended to 3 hours, FGS could be finally obtained through the process without TOPO. Therefore, compared to the reaction with TOPO, it is apparent that the reaction without TOPO takes a longer time to form FGS nanoparticles. This result is also supported by the XRF results shown in Table 5.1. Thus, we can speculate the TOPO does affect the reaction rate.

**Table 5.1.** XRF results of as-synthesized FGS NPs using different time.

Sample	Fe (at. %)	Ge (at. %)	S (at. %)	Fe/Ge	S/(Fe+Ge)
FGS-2 hours	40.04	29.27	30.69	1.37	0.44
FGS-2.5 hours	22.73	41.81	35.46	0.54	0.55
FGS-3 hours	33.26	16.61	50.13	2.00	1.01

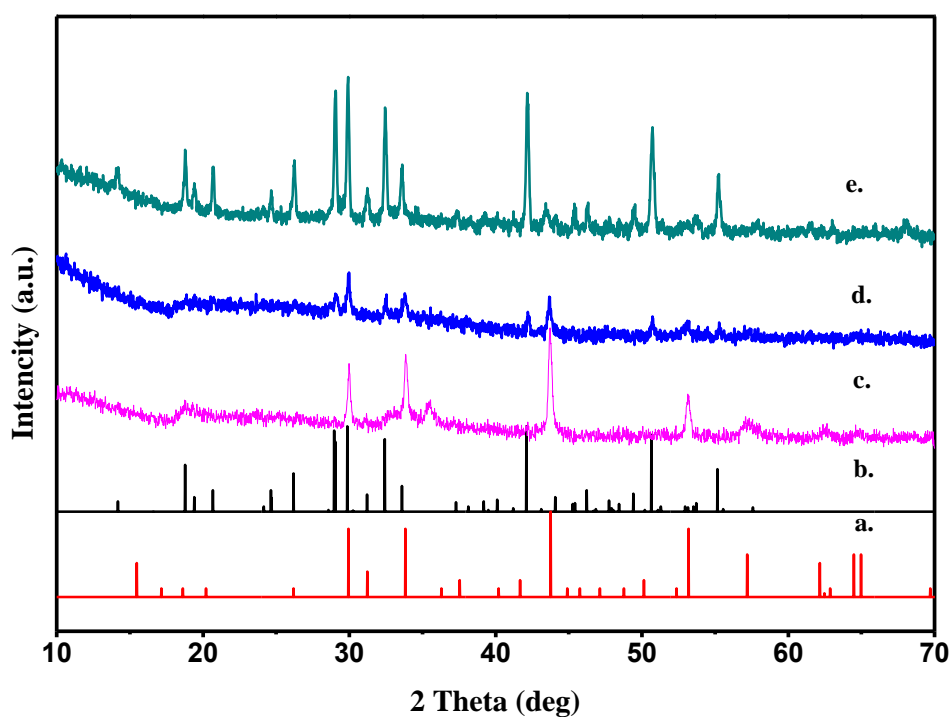


**Figure 5.8.** XRD Patterns of FGS NPs prepared without TOPO. (a) Pyrrhotite standard card; (b) FGS Standard card; (c) FGS-without TOPO-2h; (d) FGS-Without TOPO-2.5h; (e) FGS-Without TOPO-3h.

### 5.3.3. Results of FGS Thin Films

According to the thermogravimetric analysis (TGA) of the as-synthesized FGS nanoparticles, FGS starts to decompose after 607 °C. So, we annealed the deposited FGS thin films at lower temperature 400 °C for 2 hours in a tube furnace under argon and sulfur atmospheres. Figure 5.9 shows the XRD pattern and Raman spectrum of the fabricated FGS thin film. The primary FGS peaks are present in the XRD pattern of the fabricated FGS thin film, although the intensity of the peak is a bit weak. The Raman spectrum exhibits a peak at 358 cm<sup>-1</sup>, belonging to the particular scattering position of the FGS olivine structure. These results fit well with the previous reports.

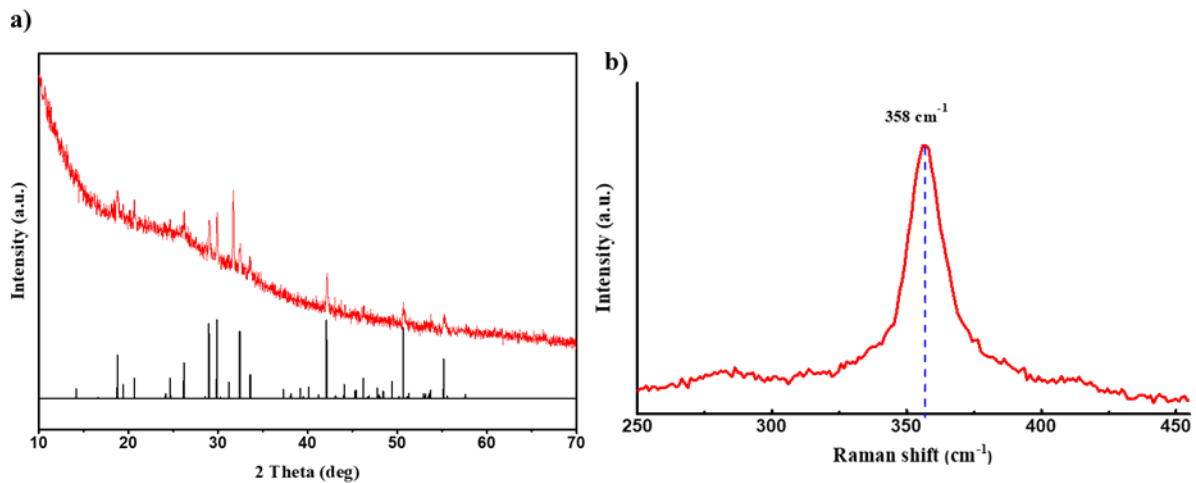


**Figure 5.9.** (a) XRD pattern of FGS thin film; (b) Raman spectrum of FGS thin film.

### 5.3.4. Results of FGS NP-Based Solar Cells

Experiments to fabricate FGS NPs based photovoltaic devices are similar to those described in the previous chapter. The photocurrent-density voltage (J-V) characteristics of the

fabricated photovoltaic devices were determined at room temperature by the combined system shown in Figure 3.4. The photovoltaic performance of the photovoltaic devices is characterized by open-circuit voltage ( $V_{OC}$ ), short-circuit current density ( $J_{SC}$ ), fill factor (FF), and conversion efficiency ( $\eta$ ).

As shown in Figure 5.10, the obtained J-V curve exhibits a poor diode behavior, the short-circuit current density ( $J_{SC}$ ) is as low as  $0.014 \text{ mA}\cdot\text{cm}^{-2}$ , and the conversion efficiency ( $\eta$ ) is only 0.002%, although the open-circuit voltage ( $V_{OC}$ ) possess a relatively high value of 416 mV.

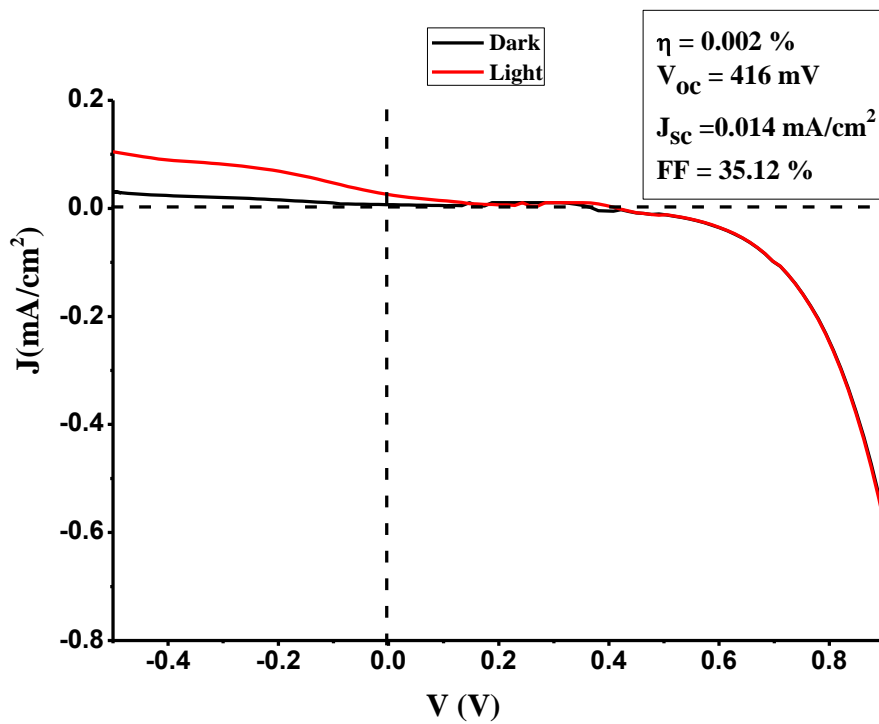


**Figure 5.10.** Device characteristics of DSSC without FGS. (ITO /TiO<sub>2</sub>&Dye/Electrolyte/ FTO).

However, when the FGS layer was incorporated into the above dye-sensitized solar cell to form an FGS-catalyzed DSSC, the photovoltaic performance was greatly improved. The

resulting device, with a structure of ITO/TiO<sub>2</sub>&Dye/ Electrolyte/FGS /FTO as shown in Figure 5.2, presents higher short-circuit current density ( $J_{SC}$ ) of 2.09 mA·cm<sup>-2</sup> and better conversion efficiency ( $\eta$ ) of 0.35%, as shown in Figure 5.11. Thus, short-circuit current density ( $J_{SC}$ ) and conversion efficiency ( $\eta$ ) increases with the incorporation of the FGS layer. This result is in line with our expectations, as we speculated in the previous chapter, FGS contributed a portion of the light absorption.

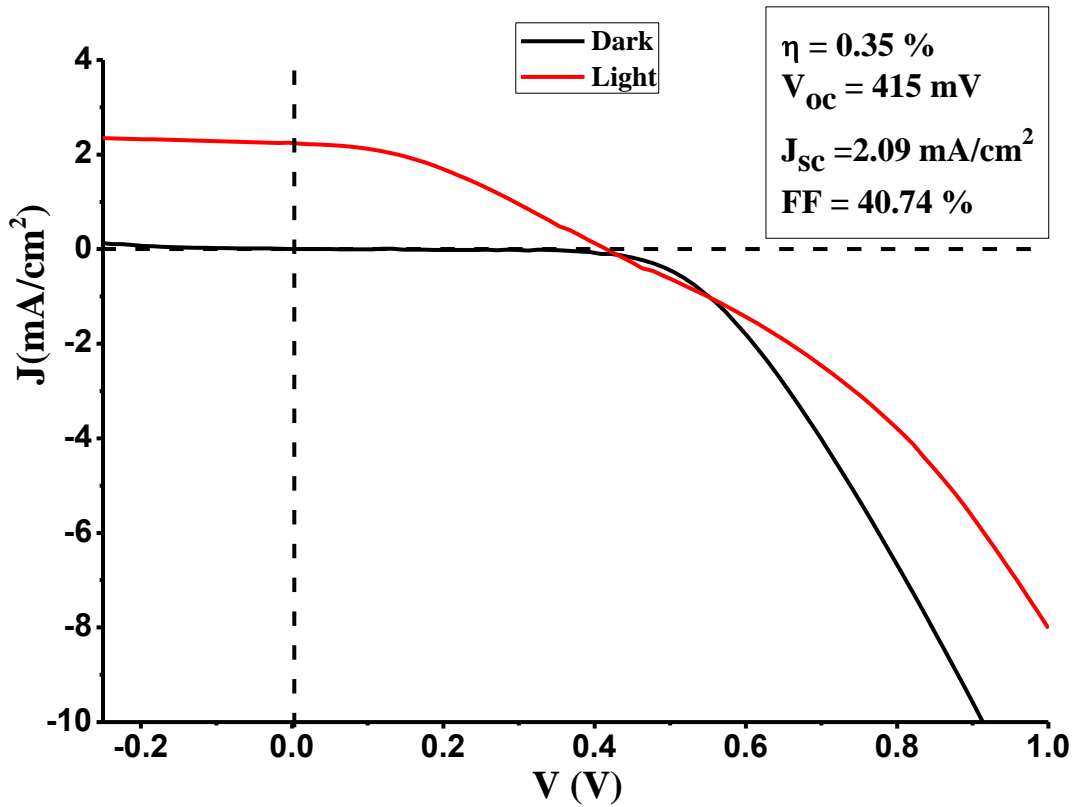


**Figure 5.11.** Device characteristics of FGS-catalyzed DSSC. (ITO/TiO<sub>2</sub>&Dye/Electrolyte /FGS/FTO).

Further, we assembled an FGS solution-based solar cell to investigate the dedication of the FGS layer to light absorption. As shown in Figure 5.3 (b), FGS NPs solution-based solar cell, with a structure of ITO/TiO<sub>2</sub>/Electrolyte/FGS /FTO, was fabricated via the same route to the FGS-catalyzed DSSC but using only TiO<sub>2</sub> thin film as the counter electrode. As shown in Figure 5.12, the measured photocurrent-voltage curve of this FGS solution-based solar cell presents a lower open-circuit voltage (V<sub>OC</sub>) of 267 mV, a low short-circuit current density (J<sub>SC</sub>) of 0.174 mA·cm<sup>-2</sup>, resulting in poor conversion efficiency (η) of 0.023%. The relatively low conversion efficiency of this photovoltaic device could be attributed to the low current extraction and high shunt conductance which probably caused by the presence of shorts or leaks in this device.

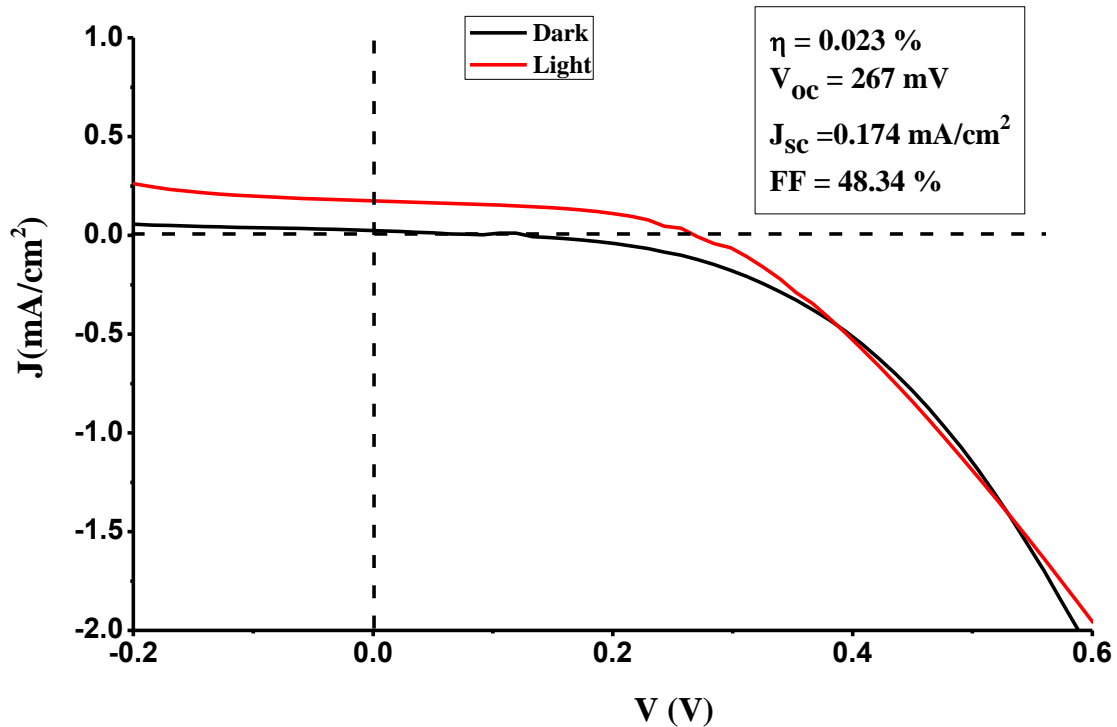


**Figure 5.12.** Device characteristics of FGS-Solution-based solar cell. (ITO/TiO<sub>2</sub>/Electrolyte /FGS/FTO).

Comparing to the FGS based photovoltaic devices made from FGS precursors in the previous chapter, the solar cells made with FGS nanoparticles possess lower conversion efficiency( $\eta$ ). We can only speculate that thin films made with very large-sized FGS nanoparticles are not uniform, which can lead to high shunt conductance in the established FGS based photovoltaic device. Despite the low conversion efficiency of fabricated photovoltaic devices, their significant open circuit voltage ( $V_{OC}$ ) still indicates that FGS is a promising candidate for photovoltaic applications.

#### **5.4. Conclusion**

An improved synthetic approach has been developed to produce FGS NPs within 5 hours. The obtained FGS NPs and thin films have been characterized by XRD, Raman spectra, and XRF. When the fabricated FGS thin film was incorporated in the counter electrode of the dye-sensitized solar cell, enhanced open-circuit voltage and power conversion efficiency were achieved, compared to a cell without FGS layer. Moreover, the FGS solution-based solar cell in which the FGS thin film worked as the light absorbing layer displayed a significant open-circuit voltage ( $V_{OC}$ ) of 267 mV. In summary, all these investigations indicate that  $Fe_2GeS_4$  is a promising candidate for light absorbing material for photovoltaic devices.

## CHAPTER 6. CONCLUSION AND PATH FORWARD

In recent decades, with the continuous depletion of non-renewable energy and the resulting environmental issues, the development and utilization of renewable energy have increasingly attracted the attention of countries all over the world. Among all kinds of renewable energy sources, solar energy is one of the most popular energy sources due to its minimal effects on the environment and its use of unlimited sunlight. Although solar energy, especially solar cells, is developing rapidly, several problems of solar cells remain unsolved challenges, such as the high cost of current solar cells, the use of earth rare elements, and the risk of using toxic elements. Nowadays, more and more research is focusing on developing a new type of earth-abundant, non-toxic and low-cost semiconductor.  $\text{Fe}_2\text{GeS}_4$  is one such material with a high absorption coefficient of  $10^5 \text{ cm}^{-1}$  and a band gap of 1.4 eV, which is suitable for photovoltaic applications. This dissertation aimed to develop a solution-phase method for FGS materials and then to fabricate high-quality thin films which used to investigate the photovoltaic performance of FGS material.

In this dissertation, two different approaches have been developed to prepare FGS materials, including solution-processed synthesis of FGS precursors and one-pot synthesis of plate-like FGS nanocrystals. Thus, two methods of preparing FGS-based solar cells have been derived.

The first method, described in chapter 4, was based on the solution-processed synthesis of FGS precursors. In the solution-processed synthesis of FGS precursor, the reactants, solvents, and the reaction time were carefully selected to account for the physical and chemical properties of the obtained products. The results present that high-stability FGS precursors were typically

prepared in OLA-ODE, using Fe(III) 2,4-pentanedionate,  $\text{Ge}(\text{Gly})_2(\text{H}_2\text{O})_2$ , elemental sulfur as Fe, Ge and S source respectively, while the reaction time is 15 minutes. The as-synthesized FGS precursors underwent a thermal treatment in argon and sulfur atmosphere to form FGS crystals. In the optimization of the annealing conditions, various annealing temperatures have been tried to prepare the FGS crystals, however, high-crystallinity and pure FGS powders were produced only at 550 °C for 2 hours. XRD patterns and Raman spectra confirmed that the final FGS powder annealed under optimized conditions was a pure FGS phase, which belongs to the olivine structure.

A high-quality FGS thin film based on the as-synthesized FGS precursors was prepared via a two-step method, including a dip-coating process and thermal treatment in a tube furnace under argon and sulfur atmosphere. Through the same optimization of the annealing conditions for the FGS powders, the XRD pattern of annealed FGS thin films exhibited that a high-quality FGS thin film can be obtained by annealing at 550 °C for 2 hours. XRD pattern and Raman spectra exhibited that the thin film annealed under the optimized conditions has proven to be a pure FGS phase without secondary phase. In addition, the room-temperature photoluminescence measurements on FGS thin films showed a band gap of around 1.40 eV, which is in good agreement with the calculated value of 1.40 eV by Yu et al. [24].

When an optimized FGS thin film was incorporated in a well-established dye-sensitized solar cell to form the FGS-catalyzed dye-sensitized solar cell with a structure of  $\text{ITO}/\text{TiO}_2\&\text{Dye}/\text{electrolyte}/\text{FGS}/\text{Mo}$ , the photocurrent-voltage (J-V) characteristics indicate that the introducing of FGS layer can enhance the open-circuit voltage ( $V_{\text{OC}}$ ) and short-circuit current density ( $J_{\text{SC}}$ ), resulting in a rise in conversion efficiency ( $\eta$ ). On the other hand, when a  $\text{TiO}_2$  thin

film was used instead of the dye-sensitized TiO<sub>2</sub>, the fabricated photovoltaic device became an FGS solution-based solar cell using an FGS thin film as the light absorbing layer. The J-V characteristics of this fabricated FGS-solution based solar cell showed a significant open-circuit voltage (V<sub>oc</sub>) of 361 mV, though it had a relatively low conversion efficiency ( $\eta$ ) of 0.14%.

The second method, described in chapter 5, was based on the one-pot synthesis of plate-like FGS nanocrystals. In this study, the influence of TOPO on the morphology and reaction time was investigated. The results show that TOPO does help to reduce the reaction time. Finally, the plate-like FGS crystals can be prepared in 5 hours, using FeCl<sub>2</sub>, Ge(Gly)<sub>2</sub>(H<sub>2</sub>O)<sub>2</sub>, trioctylphosphine oxide (TOPO), and 1-dodecanethiol(1-DDT) as reactants, while the OLA suffers as the solvent. The obtained powder was confirmed to be the FGS phase by Raman spectra and XRD pattern. TEM images showed that the as-synthesized FGS were plate-like nanocrystals with sizes ranging from 400 to 800 nm.

A stable FGS thin film was fabricated by a two-step process including dip-coating the FGS NCs on a clean substrate and a subsequent thermal treatment in a tube furnace at 400 °C for 2 hours under the argon and sulfur atmosphere. The resulting thin films were characterized by Raman spectroscopy and XRD, confirming that there were no secondary phases presented in the annealing thin film, but only the pure FGS phase.

Similar to the fabrication of solution-processed FGS based solar cells, the FGS thin film prepared using FGS NCs was introduced into the dye-sensitized solar cell to form an FGS NPs catalyzed dye-sensitized solar cell with a structure of ITO/TiO<sub>2</sub>&Dye/electrolyte/FGS/FTO. The J-V measurements show that an enhanced open-circuit voltage and power conversion efficiency were achieved when incorporating the fabricated FGS thin film to the counter electrode of the

dye-sensitized solar cell. Furthermore, the FGS NPs-solution-based solar cell in which FGS thin film worked as a light absorbing layer displayed a significant open-circuit voltage ( $V_{OC}$ ) of 267 mV.

In summary, all these investigations indicate that  $Fe_2GeS_4$  holds the potential to absorb photons and convert light into electricity, suggesting that it is a promising candidate for photoactive in photovoltaic applications. However, all of these fabricated photovoltaic devices suffered from low short-circuit current density ( $J_{SC}$ ) and low power conversion efficiency, which probably caused by the low current extraction and high shunt conductance.

According to the investigations, some suggested future work are as follows:

1. Control the size and morphology of the FGS nanoparticles to improve their optical and electrical properties, even the photovoltaic performance.
2. Optimizing the process of making the thin films is also recommended to minimize the adverse influences on the performance of the solar cell.
3. Other suitable constructs of the solar cell are required to develop.
4. The main challenge for commercialization is scaling up lab-scale techniques to industrial production while maintaining high efficiency. For the commercialization of FGS based solar cells, there are several approaches are proposed. 1) using conductive substrates with large areas ( $120\text{ cm}^2$ ) instead of the lab-used  $0.5\text{ cm}^2$  to scale-up<sup>[98]</sup>; 2) using roll-to-roll electrodeposition-based process or in-line deposition process instead of dip-coating to improve the manufacturing<sup>[98,99]</sup>; 3) using stacking cells structure instead of dye-sensitized solar cells to improve the power conversion efficiency.

## REFERENCES

- [1] CHARRIAU, P. (2017). Global Energy Trends. 2017. Retrieved June 06, 2017, from <https://www.enerdata.net/publications/reports-presentations/global-energy-trends-2017.html>.
- [2] OECD/IEA. (2015). CO<sub>2</sub> Emissions From Fuel Combustion. Retrieved from [https://www.iea.org/publications/freepublications/publication/CO<sub>2</sub>EmissionsFromFuelCombustionHighlights2015.pdf](https://www.iea.org/publications/freepublications/publication/CO2EmissionsFromFuelCombustionHighlights2015.pdf).
- [3] Becquerel, M. E. (1839). Mémoire sur les effets électriques produits sous l'influence des rayons solaires. *Comptes rendus hebdomadaires des séances de l'Académie des sciences*, 9, 561-567.
- [4] Williams, R. (1960). Becquerel photovoltaic effect in binary compounds. *The journal of Chemical physics*, 32(5), 1505-1514.
- [5] Riordan, M., & Hoddeson, L. (1997). The origins of the pn junction. *IEEE spectrum*, 34(6), 46-51.
- [6] Cyferz. (2012). Silicon Solar cell structure and mechanism. Retrieved september 23, 2016, from [https://commons.wikimedia.org/wiki/File:Silicon\\_Solar\\_cell\\_structure\\_and\\_mechanism.svg](https://commons.wikimedia.org/wiki/File:Silicon_Solar_cell_structure_and_mechanism.svg).
- [7] Russell S. Ohl. Red Bank. N.J., Light-Sensitive Electric Device Including Silicon. US 2402662, June 15, 1948.
- [8] Green, M. A. (2017). Corrigendum to 'Solar cell efficiency tables (version 49)' [Prog. Photovolt: Res. Appl. 2017; 25: 3–13]. *Progress in Photovoltaics: Research and Applications*, 4(25), 333-334.
- [9] Ahmadi, T. S., Wang, Z. L., Green, T. C., Henglein, A., & El-Sayed, M. A. (1996). Shape-controlled synthesis of colloidal platinum nanoparticles. *Science*, 272(5270), 1924-1925.
- [10] Collins, R. W., Ferlauto, A. S., Ferreira, G. M., Chen, C., Koh, J., Koval, R. J., ... & Wronski, C. R. (2003). Evolution of microstructure and phase in amorphous, protocrystalline, and microcrystalline silicon studied by real time spectroscopic ellipsometry. *Solar energy materials and solar cells*, 78(1-4), 143-180.
- [11] Smith, Z. E., & Wagner, S. (1987). Band tails, entropy, and equilibrium defects in hydrogenated amorphous silicon. *Physical review letters*, 59(6), 688.
- [12] Meier, J., Flückiger, R., Keppner, H., & Shah, A. (1994). Complete microcrystalline p-i-n solar cell—Crystalline or amorphous cell behavior?. *Applied Physics Letters*, 65(7), 860-862.

- [13] Sai, H., Matsui, T., Koida, T., Matsubara, K., Kondo, M., Sugiyama, S., ... & Yoshida, I. (2015). Triple-junction thin-film silicon solar cell fabricated on periodically textured substrate with a stabilized efficiency of 13.6%. *Applied Physics Letters*, 106(21), 213902.
- [14] Nguyen, K. C., Willmore, W. G., & Tayabali, A. F. (2013). Cadmium telluride quantum dots cause oxidative stress leading to extrinsic and intrinsic apoptosis in hepatocellular carcinoma HepG2 cells. *Toxicology*, 306, 114-123.
- [15] Fthenakis, V. M. (2004). Life cycle impact analysis of cadmium in CdTe PV production. *Renewable and Sustainable Energy Reviews*, 8(4), 303-334.
- [16] Shockley, W., & Queisser, H. J. (1961). Detailed balance limit of efficiency of p-n junction solar cells. *Journal of applied physics*, 32(3), 510-519.
- [17] Rühle, S. (2016). Tabulated values of the Shockley–Queisser limit for single junction solar cells. *Solar Energy*, 130, 139-147.
- [18] Kibria, M. T., Ahammed, A., Sony, S. M., Hossain, F., & Islam, S. U. (2014, September). A Review: Comparative studies on different generation solar cells technology. In *Proc. of 5th International Conference on Environmental Aspects of Bangladesh*.
- [19] Goetzberger, A., Knobloch, J., & Voss, B. (1998). Crystalline silicon solar cells. *editorial John Wiley & Sons Ltd, 1*.
- [20] Jordan Hanania, K. S., Jason Donev. (2015). Energy Education - Band gap. Retrieved September 10, 2016, from [https://energyeducation.ca/encyclopedia/Band\\_gap](https://energyeducation.ca/encyclopedia/Band_gap).
- [21] Nanoscale Material Design. (2013). Nrel.gov. Retrieved August 14, 2018, from [https://en.wikipedia.org/wiki/Band\\_gap](https://en.wikipedia.org/wiki/Band_gap).
- [22] Direct and Indirect Band Gap Semiconductors. (2004). Retrieved August 16, 2018, from <https://www.doitpoms.ac.uk/tlplib/semiconductors/direct.php>.
- [23] Möller, H. J. (1993). *Semiconductors for solar cells*. Artech House Publishers.
- [24] Yu, L., Lany, S., Kykyneshi, R., Jieratum, V., Ravichandran, R., Pelatt, B., ... & Zunger, A. (2011). Iron chalcogenide photovoltaic absorbers. *Advanced Energy Materials*, 1(5), 748-753.
- [25] Park, B. I., Yu, S., Hwang, Y., Cho, S. H., Lee, J. S., Park, C., ... & Lee, S. Y. (2015). Highly crystalline Fe<sub>2</sub>GeS<sub>4</sub> nanocrystals: green synthesis and their structural and optical characterization. *Journal of Materials Chemistry A*, 3(5), 2265-2270.
- [26] Tsubomura, H., Matsumura, M., Nomura, Y., & Amamiya, T. (1976). Dye sensitised zinc oxide: aqueous electrolyte: platinum photocell. *Nature*, 261(5559), 402.

- [27] Desilvestro, J., Graetzel, M., Kavan, L., Moser, J., & Augustynski, J. (1985). Highly efficient sensitization of titanium dioxide. *Journal of the American Chemical Society*, *107*(10), 2988-2990.
- [28] O'Regan, B., & Grätzel, M. (1991). A low cost and high-efficiency solar cell based on dye-sensitization of colloidal titanium dioxide films. *Nature*, *356*(6346), 737-740.
- [29] Nakade, S., Kanzaki, T., Kubo, W., Kitamura, T., Wada, Y., & Yanagida, S. (2005). Role of electrolytes on charge recombination in dye-sensitized TiO<sub>2</sub> solar cell (1): the case of solar cells using the I-/I<sub>3</sub>-redox couple. *The Journal of Physical Chemistry B*, *109*(8), 3480-3487.
- [30] Wu, J., Lan, Z., Lin, J., Huang, M., Huang, Y., Fan, L., & Luo, G. (2015). Electrolytes in dye-sensitized solar cells. *Chemical reviews*, *115*(5), 2136-2173.
- [31] Hassan, F. E. H., & Akbarzadeh, H. (2006). Ground state properties and structural phase transition of beryllium chalcogenides. *Computational materials science*, *35*(4), 423-431.
- [32] Emsley, J. (2011). *Nature's building blocks: an AZ guide to the elements*. Oxford University Press.
- [33] Han, C. (2015). Synthesis of nanostructured metal chalcogenides used for energy conversion and storage.
- [34] Yang, Y., Liu, J., Liu, F., Wang, Z., & Miao, S. (2018). Molecular-level insights into mercury removal mechanism by pyrite. *Journal of hazardous materials*, *344*, 104-112.
- [35] Zhang, M. Y., Cui, Z. H., & Jiang, H. (2018). Relative stability of FeS<sub>2</sub> polymorphs with the random phase approximation approach. *Journal of Materials Chemistry A*, *6*(15), 6606-6616.
- [36] Li, Y., Chen, J., Chen, Y., Zhao, C., Lee, M. H., & Lin, T. H. (2018). DFT+ U study on the electronic structures and optical properties of pyrite and marcasite. *Computational Materials Science*, *150*, 346-352.
- [37] Schlegel, A., & Wachter, P. (1976). Optical properties, phonons and electronic structure of iron pyrite (FeS<sub>2</sub>). *Journal of Physics C: Solid State Physics*, *9*(17), 3363.
- [38] Jagadeesh, M. S., & Seehra, M. S. (1980). Electrical resistivity and band gap of marcasite (FeS<sub>2</sub>). *Physics Letters A*, *80*(1), 59-61.
- [39] Bullett, D. W. (1982). Electronic structure of 3d pyrite-and marcasite-type sulphides. *Journal of Physics C: solid state physics*, *15*(30), 6163.
- [40] Eyert, V., Höck, K. H., Fiechter, S., & Tributsch, H. (1998). Electronic structure of FeS<sub>2</sub>: The crucial role of electron-lattice interaction. *Physical Review B*, *57*(11), 6350.

- [41] Sun, R., Chan, M. K. Y., & Ceder, G. (2011). First-principles electronic structure and relative stability of pyrite and marcasite: Implications for photovoltaic performance. *Physical Review B*, 83(23), 235311.
- [42] Ennaoui, A., Fiechter, S., Pettenkofer, C., Alonso-Vante, N., Bükler, K., Bronold, M., & Tributsch, H. (1993). Iron disulfide for solar energy conversion. *Solar Energy Materials and Solar Cells*, 29(4), 289-370.
- [43] Ennaoui, A., Fiechter, S., Jaegermann, W., & Tributsch, H. (1986). Photoelectrochemistry of highly quantum efficient single-crystalline n-FeS<sub>2</sub> (Pyrite). *Journal of the Electrochemical Society*, 133(1), 97-106.
- [44] Prabukanthan, P., Thamaraiselvi, S., & Harichandran, G. (2018). Structural, morphological, electrocatalytic activity and photocurrent properties of electrochemically deposited FeS<sub>2</sub> thin films. *Journal of Materials Science: Materials in Electronics*, 1-13.
- [45] Zhang, X., Li, M., Walter, J., O'Brien, L., Manno, M. A., Voigt, B., ... & Leighton, C. (2017). Potential resolution to the doping puzzle in iron pyrite: Carrier type determination by Hall effect and thermopower. *Physical Review Materials*, 1(1), 015402.
- [46] Gronvold, F., & Westrum Jr, E. F. (1976). Heat capacities of iron disulfides Thermodynamics of marcasite from 5 to 700 K, pyrite from 300 to 780 K, and the transformation of marcasite to pyrite.
- [47] Bükler, K., Alonso-Vante, N., & Tributsch, H. (1992). Photovoltaic output limitation of n-FeS<sub>2</sub> (pyrite) Schottky barriers: A temperature-dependent characterization. *Journal of applied physics*, 72(12), 5721-5728.
- [48] Rui, X., Tan, H., & Yan, Q. (2014). Nanostructured metal sulfides for energy storage. *Nanoscale*, 6(17), 9889-9924.
- [49] Mills, B. (2007). Ball-and-stick model of the unit cell of iron(II) sulfide, FeS. Retrieved June 26, 2018, from [https://commons.wikimedia.org/wiki/File:Iron\(II\)-sulfide-unit-cell-3D-balls.png](https://commons.wikimedia.org/wiki/File:Iron(II)-sulfide-unit-cell-3D-balls.png).
- [50] Devey, A. J., Grau-Crespo, R., & de Leeuw, N. H. (2009). Electronic and magnetic structure of Fe<sub>3</sub>S<sub>4</sub>: GGA+ U investigation. *Physical Review B*, 79(19), 195126.
- [51] Nesbitt, H. W., Schaufuss, A. G., Bancroft, G. M., & Szargan, R. (2002). Crystal orbital contributions to the pyrrhotite valence band with XPS evidence for weak Fe-Fe  $\pi$  bond formation. *Physics and chemistry of minerals*, 29(1), 72-77.
- [52] Wang, H., & Salveson, I. (2005). A review on the mineral chemistry of the non-stoichiometric iron sulphide, Fe<sub>1-x</sub>S (0 ≤ x ≤ 0.125): polymorphs, phase relations and transitions, electronic and magnetic structures. *Phase Transitions*, 78(7-8), 547-567.

- [53] Vincent, H., Bertaut, E. F., Baur, W. H., & Shannon, R. D. (1976). Polyhedral deformations in olivine-type compounds and the crystal structure of  $\text{Fe}_2\text{SiS}_4$  and  $\text{Fe}_2\text{GeS}_4$ . *Acta Crystallographica Section B*, 32(6), 1749-1755.
- [54] Kristin Persson. *Materials Data on  $\text{Fe}_2\text{GeS}_4$  (SG:62) by Materials Project*. United States. doi:10.17188/1196363.
- [55] Fredrick, S. J., & Prieto, A. L. (2013). Solution synthesis and reactivity of colloidal  $\text{Fe}_2\text{GeS}_4$ : a potential candidate for Earth abundant, nanostructured photovoltaics. *Journal of the American Chemical Society*, 135(49), 18256-18259.
- [56] Vincent, H., & Bertaut, E. F. (1973). Etude Cristallographique et Magnetique de  $\text{Fe}_2\text{GeS}_4$  Structures Magnetiques a 85 et 4, 2 K. *Journal of Physics and Chemistry of Solids*, 34(2), 151-158.
- [57] Junod, A., Wang, K. Q., Triscone, G., & Lamarche, G. (1995). Specific heat, magnetic properties and critical behaviour of  $\text{Mn}_2\text{SiS}_4$  and  $\text{Fe}_2\text{GeS}_4$ . *Journal of magnetism and magnetic materials*, 146(1-2), 21-29.
- [58] Ohgushi, K., & Ueda, Y. (2006, September). Anomalous magnetic properties of  $\text{Fe}_2\text{GeS}_4$  and  $\text{Mn}_2\text{SiS}_4$ . In *AIP Conference Proceedings* (Vol. 850, No. 1, pp. 1277-1278). AIP.
- [59] Rowe, D. M. (2005). *Thermoelectrics handbook: macro to nano*. CRC press.
- [60] Aoard, G., Wu, M., & Chen, Y. (2010). Report to the Grant AOARD-08-4049 Development of High ZT Thermoelectric Materials with Nanostructure for Energy Applications.
- [61] Platt, H. A. (2010). Copper and iron chalcogenides for efficient solar absorption.
- [62] Gudelli, V. K., Kanchana, V., & Vaitheeswaran, G. (2015). Predicted thermoelectric properties of olivine-type  $\text{Fe}_2\text{GeCh}_4$  (Ch= S, Se and Te). *Journal of Physics: Condensed Matter*, 28(2), 025502.
- [63] Richard, A. P. (2011). Single crystal growth, powder synthesis and characterization of layered chalcogenide semiconductors.
- [64] Hwang, P. Y., Berg, D. M., Liu, M., Lai, C. Y., & Radu, D. R. (2018). A rapid molecular precursor solid-state route to crystalline  $\text{Fe}_2\text{GeS}_4$  nanoparticles. *Materials Letters*, 223, 128-132.
- [65] Wang, W., Jiang, J., Ding, T., Wang, C., Zuo, J., & Yang, Q. (2015). Alternative synthesis of  $\text{CuFeSe}_2$  nanocrystals with magnetic and photoelectric properties. *ACS applied materials & interfaces*, 7(4), 2235-2241.
- [66] Lim, D. H., Ramasamy, P., & Lee, J. S. (2016). Solution synthesis of single-crystalline  $\text{Fe}_2\text{GeS}_4$  nanosheets. *Materials Letters*, 183, 65-68.

- [67] Guruleninn. (2011, 25 November 2016). Process flow diagram of PVD. Retrieved June 23, 2018, from [https://commons.wikimedia.org/wiki/File:PVD\\_process.svg](https://commons.wikimedia.org/wiki/File:PVD_process.svg).
- [68] Davis, C. M., & Curran, K. A. (2007). Manipulation of a Schlenk line: preparation of tetrahydrofuran complexes of transition-metal chlorides. *Journal of chemical education*, 84(11), 1822.
- [69] Liu, M., Berg, D. M., Hwang, P. Y., Lai, C. Y., Stone, K. H., Babbe, F., ... & Radu, D. R. (2018). The promise of solution-processed Fe<sub>2</sub>GeS<sub>4</sub> thin films in iron chalcogenide photovoltaics. *Journal of Materials Science*, 53(10), 7725-7734.
- [70] Chan, D. S., & Phang, J. C. (1987). Analytical methods for the extraction of solar-cell single-and double-diode model parameters from IV characteristics. *IEEE Transactions on Electron devices*, 34(2), 286-293.
- [71] Ferber, J., & Luther, J. (2001). Modeling of photovoltage and photocurrent in dye-sensitized titanium dioxide solar cells. *The Journal of Physical Chemistry B*, 105(21), 4895-4903.
- [72] Ito, S., Murakami, T. N., Comte, P., Liska, P., Grätzel, C., Nazeeruddin, M. K., & Grätzel, M. (2008). Fabrication of thin film dye sensitized solar cells with solar to electric power conversion efficiency over 10%. *Thin solid films*, 516(14), 4613-4619.
- [73] Parisi, A., Pernice, R., Andò, A., Adamo, G., Cino, A. C., & Busacca, A. C. (2016, October). Experimental characterization of Ruthenium-based Dye Sensitized Solar Cells and study of light-soaking effect impact on performance. In *AEIT International Annual Conference (AEIT), 2016* (pp. 1-5). IEEE.
- [74] Chiang, H. C., Wang, M. H., & Ueng, C. H. (1993). Synthesis and structure of diaquabis (glycolato-O, O") germanium (IV). *Acta Crystallographica Section C*, 49(2), 244-246.
- [75] Kalyanasundaram, K., & Grätzel, M. (2009). Efficient dye-sensitized solar cells for direct conversion of sunlight to electricity. *Material Matters*, 4(4), 88-90.
- [76] Xin, X., He, M., Han, W., Jung, J., & Lin, Z. (2011). Low-cost copper zinc tin sulfide counter electrodes for high-efficiency dye-sensitized solar cells. *Angewandte Chemie International Edition*, 50(49), 11739-11742.
- [77] Tong, Z., Su, Z., Liu, F., Jiang, L., Lai, Y., Li, J., & Liu, Y. (2014). In situ prepared Cu<sub>2</sub>ZnSnS<sub>4</sub> ultrathin film counter electrode in dye-sensitized solar cells. *Materials Letters*, 121, 241-243.
- [78] Suryawanshi, M. P., Ghorpade, U. V., Shin, S. W., Pawar, S. A., Kim, I. Y., Hong, C. W., ... & Kim, J. H. (2016). A simple aqueous precursor solution processing of earth-abundant Cu<sub>2</sub>SnS<sub>3</sub> absorbers for thin-film solar cells. *ACS applied materials & interfaces*, 8(18), 11603-11614.

- [79] Benny, P. D., Ganguly, T., Raiford, L., Fugate, G. A., & Twamley, B. (2011). Synthesis and reactivity of acetylacetonate with amine ligands in fac-Re(OH<sub>2</sub>)<sub>3</sub>(CO)<sub>3</sub><sup>+</sup> complexes. *Inorganic Chemistry Communications*, 14(2), 392-395.
- [80] Pereira, C., Patrício, S., Silva, A. R., Magalhães, A. L., Carvalho, A. P., Pires, J., & Freire, C. (2007). Copper acetylacetonate anchored onto amine-functionalised clays. *Journal of colloid and interface science*, 316(2), 570-579.
- [81] Mourdikoudis, S., & Liz-Marzán, L. M. (2013). Oleylamine in nanoparticle synthesis. *Chemistry of Materials*, 25(9), 1465-1476.
- [82] Xu, Z., Shen, C., Hou, Y., Gao, H., & Sun, S. (2009). Oleylamine as both reducing agent and stabilizer in a facile synthesis of magnetite nanoparticles. *Chemistry of Materials*, 21(9), 1778-1780.
- [83] Carencu, S., Labouille, S., Bouchonnet, S., Boissière, C., Le Goff, X. F., Sanchez, C., & Mezaillies, N. (2012). Revisiting the molecular roots of a ubiquitously successful synthesis: Nickel (0) nanoparticles by reduction of [Ni (acetylacetonate)<sub>2</sub>]. *Chemistry—A European Journal*, 18(44), 14165-14173.
- [84] Irkhina, A., Levchenko, S., Hinrichs, V., Plate, P., & Unold, T. (2017). Metal acetate-based synthesis of small-sized Cu<sub>2</sub>ZnSnS<sub>4</sub> nanocrystals: effect of injection temperature and synthesis time. *RSC Advances*, 7(19), 11752-11760.
- [85] Nolan, B. M., Chan, E. K., Zhang, X., Muthuswamy, E., Van Benthem, K., & Kauzlarich, S. M. (2016). Sacrificial silver nanoparticles: reducing GeI<sub>2</sub> to form hollow germanium nanoparticles by electroless deposition. *ACS nano*, 10(5), 5391-5397.
- [86] Zhang, X., Scott, T., Socha, T., Nielsen, D., Manno, M., Johnson, M., ... & Leighton, C. (2015). Phase stability and stoichiometry in thin film iron pyrite: impact on electronic transport properties. *ACS applied materials & interfaces*, 7(25), 14130-14139.
- [87] Liu, W., Hu, L., Dai, S., Guo, L., Jiang, N., & Kou, D. (2010). The effect of the series resistance in dye-sensitized solar cells explored by electron transport and back reaction using electrical and optical modulation techniques. *Electrochimica acta*, 55(7), 2338-2343.
- [88] Collection Probability. (2018). Retrieved July 23, 2018, from <https://www.pveducation.org/pvcdrom/solar-cell-operation/collection-probability>.
- [89] Wang, W., Jiang, J., Ding, T., Wang, C., Zuo, J., & Yang, Q. (2015). Alternative synthesis of CuFeSe<sub>2</sub> nanocrystals with magnetic and photoelectric properties. *ACS applied materials & interfaces*, 7(4), 2235-2241.
- [90] Zhang, L., Li, Z. J., Lin, Q. P., Qin, Y. Y., Zhang, J., Yin, P. X., ... & Yao, Y. G. (2009). Synthesis, structure, and luminescent properties of hybrid inorganic–organic framework

materials formed by lead aromatic carboxylates: inorganic connectivity variation from 0D to 3D. *Inorganic chemistry*, 48(14), 6517-6525.

[91] Efros, A. L., & Efros, A. L. (1982). Interband absorption of light in a semiconductor sphere. *Soviet Physics Semiconductors-Ussr*, 16(7), 772-775.

[92] Rossetti, R., Nakahara, S., & Brus, L. E. (1983). Quantum size effects in the redox potentials, resonance Raman spectra, and electronic spectra of CdS crystallites in aqueous solution. *The Journal of Chemical Physics*, 79(2), 1086-1088.

[93] Takagahara, T., & Takeda, K. (1992). Theory of the quantum confinement effect on excitons in quantum dots of indirect-gap materials. *Physical Review B*, 46(23), 15578.

[94] Talapin, D. V., Rogach, A. L., Kornowski, A., Haase, M., & Weller, H. (2001). Highly luminescent monodisperse CdSe and CdSe/ZnS nanocrystals synthesized in a hexadecylamine– trioctylphosphine oxide– trioctylphosphine mixture. *Nano letters*, 1(4), 207-211.

[95] Peng, X., Manna, L., Yang, W., Wickham, J., Scher, E., Kadavanich, A., & Alivisatos, A. P. (2000). Shape control of CdSe nanocrystals. *Nature*, 404(6773), 59.

[96] Li, W., Lee, S. S., Wu, J., Hinton, C. H., & Fortner, J. D. (2016). Shape and size-controlled synthesis of uniform iron oxide nanocrystals through new non-hydrolytic routes. *Nanotechnology*, 27(32), 324002.

[97] Hong, Y. K., Cho, G., Park, Y., Oh, S. J., & Ha, D. H. (2018). Trioctylphosphine-assisted morphology control of ZnO nanoparticles. *Nanotechnology*, 29(22), 225602.

[98] Parisi, A., Pernice, R., Andò, A., Adamo, G., Cino, A. C., & Busacca, A. C. (2016, October). Experimental characterization of Ruthenium-based Dye Sensitized Solar Cells and study of light-soaking effect impact on performance. In *AEIT International Annual Conference (AEIT), 2016* (pp. 1-5). IEEE.

[99] Basol, B. (2010). *Commercialization of High Efficiency Low Cost CIGS Technology Based on Electroplating: Final Technical Progress Report, 28 September 2007-30 June 2009*(No. NREL/SR-520-48590). National Renewable Energy Lab.(NREL), Golden, CO (United States).

[100] Ramanujam, J., & Singh, U. P. (2017). Copper indium gallium selenide based solar cells—a review. *Energy & Environmental Science*, 10(6), 1306-1319.